

United Arab Emirates University

Scholarworks@UAEU

Dissertations

Electronic Theses and Dissertations

4-2021

THERMAL EVALUATION OF ADVANCED LEADING EDGE FOR ROTATING GAS TURBINE BLADE: NUMERICAL AND EXPERIMENTAL INVESTIGATIONS

Amin Safi

Follow this and additional works at: https://scholarworks.uaeu.ac.ae/all_dissertations



Part of the [Mechanical Engineering Commons](#)

United Arab Emirates University

College of Engineering

THERMAL EVALUATION OF ADVANCED LEADING EDGE FOR
ROTATING GAS TURBINE BLADE: NUMERICAL AND
EXPERIMENTAL INVESTIGATIONS

Amin Safi

This dissertation is submitted in partial fulfillment of the requirements for the degree
of Doctor of Philosophy

Under the Supervision of Dr. Emad Elnajjar

April 2021

Declaration of Original Work

I, Amin Safi, the undersigned, a graduate student at the United Arab Emirates University (UAEU), and the author of this dissertation entitled “*Thermal Evaluation of Advanced Leading Edge for Rotating Gas Turbine Blade: Numerical and Experimental Investigations*” hereby, solemnly declare that this dissertation is my own original research work that has been done and prepared by me under the supervision of Dr. Emad Elnajjar, in the College of Engineering at UAEU. This work has not previously formed the basis for the award of any academic degree, diploma or a similar title at this or any other university. Any materials borrowed from other sources (whether published or unpublished) and relied upon or included in my dissertation have been properly cited and acknowledged in accordance with appropriate academic conventions. I further declare that there is no potential conflict of interest with respect to the research, data collection, authorship, presentation, and publication of this dissertation.

Student's Signature:  _____

Date: April 20, 2021

Copyright © 2021 Amin Safi
All Rights Reserved

Advisory Committee

1) Advisor: Emad Elnajjar

Title: Associate Professor

Department of Mechanical Engineering

College of Engineering, UAEU

2) Co-Advisor (External Member): Mohammad O. Hamdan

Title: Professor

Department of Mechanical Engineering

College of Engineering

American University of Sharjah, UAE

3) Member: Salah Al Omari

Title: Professor

Department of Mechanical Engineering

College of Engineering, UAEU

4) Member: Bobby Mathew

Title: Associate Professor

Department of Mechanical Engineering

College of Engineering, UAEU

Approval of the Doctorate Dissertation

This Doctorate Dissertation is approved by the following Examining Committee Members:

Advisor (Committee Chair): Dr. Emad Elnajjar

Title: Associate Professor

Department of Mechanical Engineering

College of Engineering

Signature

Date April 18, 2021

1) Member: Mahmoud Elgendi

Title: Associate Professor

Department of Mechanical Engineering

College of Engineering

Signature

Date April 19, 2021

2) Member: Qasem Al Mdallal

Title: Professor

Department of Mathematical Science

College of Science

Signature

Date April 18, 2021

3) Member (External Examiner): Farzad Mashayek

Title: Professor

Department of Mechanical and Industrial Engineering

Institution: University of Illinois at Chicago (UIC)

Signature

Date April 18, 2021

This Doctorate Dissertation is accepted by:

Dean of the College of Engineering: Professor James F. Klausner

Signature James F. Klausner Date 16/5/2021

Dean of the College of Graduate Studies: Professor Ali Al-Marzouqi

Signature Ali Hassan Date 16/5/2021

Copy ____ of ____

Abstract

Gas turbine engines play a vital role in our life. Our power demand is significantly and continuously growing. One approach to improve thermal efficiency in gas turbine engines requires a higher turbine inlet gas temperature. Advanced gas turbine engines operate at high temperatures, around 2000 K. Since operating at high temperatures may compromise the blade structure integrity, different cooling systems are used in a turbine blades. One of the most efficient cooling techniques is impingement cooling, mostly used in the leading edge. The leading edge experiences the highest temperature in the blade exposed to the hottest gas.

Researchers studied different factors over the years to identify and optimize jet impingement on the leading edge of the blade. Nevertheless, publications on jets impingement under rotation are limited in the public literature. Hence, the objective of this study is to evaluate blade cooling via jet impingement on a rotating semi-circular internal channel. The study is initially carried out numerically and experimentally for validation purpose. After validation, a parametric numerical model is developed to understand the effect of internal jets impingement on a rotating leading edge. By comparing the experimental results and the numerical results, all features of the temperature distribution over the target surface are precisely captured. A good agreement between the numerical analysis and the experimental measurements has been established.

The parametric numerical model is used to test higher jet Reynolds numbers, varying between 7,500 to 30,000, and a higher rotating speed, ranging from 0 to 750 rpm. The results show that jets impingement with high Reynolds numbers is an efficient method of cooling a rotating leading edge. The jets impingement cooling

performance is strongly influenced by the individual jet location, the crossflow from other jets, and the blade rotation speed. The effect of rotation is diminished at high jet Reynolds numbers. The cooling performance improves as jet Reynolds number increases and as rotating speed decreases.

Keywords: Gas turbine engine, SST $k-\omega$ model, thermal efficiency, turbine inlet temperature, impingement cooling, turbine blade cooling, rotating leading-edge, crossflow, thermochromic liquid crystal.

Title and Abstract (in Arabic)

التقييم الحراري للحافة المتقدمة لزعفة التربيننة الغازية أثناء الدوران - دراسات عملية ورقمية

الملخص

تلعب المحركات التوربينية الغازية دورًا حيويًا في حياتنا. ويتزايد الطلب على الطاقة لدينا بشكل كبير ومستمر، مما أدى إلى تحسين الكفاءة الحرارية لمحركات التوربينات الغازية. ولتحسين الكفاءة الحرارية في محركات التوربينات الغازية يتطلب ذلك إرتفاع في درجات حرارة الغازات الداخلة للتوربينات. وبما أن العامل الأساسي في تحديد درجات حراره الغازات الداخلة للتوربينات هو القيود الموجوده على المواد المصنوع منها ريش التوربينات الغازية؛ لذلك يتم إستخدام طرق تبريد حراريه مبتكره لحماية شفرة التوربين من إرتفاع درجة حرارة الغاز الداخل لها .

تعمل المحركات التوربينية الغازية المتقدمة في درجات حرارة عالية، حوالي (2000 كلفن)، ونظرًا لأن التشغيل في درجات حرارة عالية قد يضر بسلامة بنية الشفرة، يتم إستخدام أنظمة تبريد مختلفة في شفرات التوربينات لتقليل درجة حرارة الشفرة وإطالة عمرها. ومن أكثر تقنيات التبريد فاعلية وقوة هو التبريد بالإصطدام، والذي يستخدم في الغالب في الحافة الأمامية للجنيحات الدوارة. تتعرض الحافة الأمامية للشفرة لأعلى درجة حرارة نظرًا لأنها معرضه لأشد الغازات الساخنة القادمة من غرفة الإحتراق. وتعتبر الحافة الأمامية للشفرة الدوارة مناسبة تمامًا للتبريد بالإصطدام بسبب المنطقة المحلية السميكة نسبيًا للشفرة .

درس الباحثون عوامل مختلفة على مر السنين لتحديد وتحسين إصطدام النفاثات بالحافة الأمامية للشفرة. ومع ذلك، فإن الأبحاث عن طريقة التبريد بواسطة إصطدام النفاثات تحت التناوب محدودة. ومن ثم، فإن الهدف من هذه الدراسة هو تقييم تبريد الشفرة عبر إصطدام النفاثات على قناة داخلية نصف دائرية دوارة. تمت هذه الدراسة على عدة مراحل، في البداية أجريت هذه الدراسة تجريبيًا وعدديًا لغرض التحقق من صحة النتائج. بعد ذلك تم تطوير نموذج عددي لفهم تأثير سلسلة من العوامل المؤثره على إصطدام النفاثات الداخلية لتبريد الحافة الأمامية الدوارة مع نطاق أعلى من أرقام رينولدز وأرقام الدوران. ثم تم إجراء دراسات التحقق التجريبية والرقمية لتبريد القناة الداخلية وذلك عن طريق إستخدام سبع نفاثات تصطدم داخل قناة داخلية نصف دائرية دوارة .

أُجريت الدراسات التجريبية لرينولدز عدد 7500 وخمس سرعات دوارة تتراوح من 0 إلى 200 دورة في الدقيقة. تم إجراء التحاليل العددية باستخدام نموذج (SST $k-\omega$) المضطرب مع تجزئة دقيقة للمجسم المدروس تم تحليله بشكل دقيق. ومن خلال مقارنة النتائج التجريبية والنتائج العددية، تم التقاط جميع ميزات توزيع درجة الحرارة على السطح المستهدف بدقة. و نتيجة لهذه المقارنات وُجد تقارب جيد بالنتائج .

أُستخدم النموذج العددي النهائي لإختبار أرقام رينولدز والتي تتراوح بين 7500 إلى 30000، وسرعة دوران أعلى تتراوح من 0 إلى 750 دورة في الدقيقة. أظهرت النتائج أن إصطدام النفاثات عند أرقام رينولدز العالية هي طريقة فعالة لتبريد الحواف الأمامية الدوارة. ويتأثر أداء تبريد إصطدام النفاثات بشدة بموقع النفاثة الفردية ، والتدفق المتقاطع من النفاثات الأخرى، وسرعة دوران الشفرة. ويلاحظ أن تأثير الدوران يتضائل عند أرقام رينولدز العالية. ويتحسن أداء التبريد مع زيادة رقم رينولدز وتناقص سرعة الدوران .

مفاهيم البحث الرئيسية: محرك التوربينات الغازية، نقل الحرارة، الكفاءة الحرارية، درجة حرارة مدخل التوربينات، تبريد الاصطدام، تبريد شفرة التوربينات.

Acknowledgments

I would like to express my deepest gratitude to my advisor Dr. Emad Elnajjar who expertly guided me during my PhD study. My sincere appreciation goes to Prof. Mohammad Hamdan for his continuous support during the course of my PhD. Especial thanks to my advisory committee members Prof. Salah Al Omari and Dr. Bobby Mathew. Your golden comments and solutions during my PhD kept me in the right track. This work would not have been possible without your support.

I would like to acknowledge, with gratitude, the support and love from my family: my parents, Afsaneh and Darioush, and my brother Sina.

Special thanks to my wife Maryam for her persistent support, understanding and encouraging during my PhD.

Also, I would like to extend my sincere thanks and appreciation to one of the greatest people, Mr. Ahmed Ghazi for his advice and support in my personal life.

Finally, I would like to thank my examination committee members for their valuable feedback, the UAEU graduate office, the mechanical engineering department's engineers and workshop.

Dedication

To my beloved wife and my parents

Table of Contents

Title	i
Declaration of Original Work	ii
Copyright	iii
Advisory Committee	iv
Approval of the Doctorate Dissertation	v
Abstract	vii
Title and Abstract (in Arabic)	ix
Acknowledgments.....	xi
Dedication	xii
Table of Contents	xiii
List of Tables.....	xvi
List of Figures	xvii
List of Abbreviations.....	xxi
Chapter 1: Introduction	1
1.1 Background	1
1.2 Problem Statement	4
1.3 Hypothesis and Novelty Statement	4
1.4 Thesis Objectives	6
1.5 Thesis Organization.....	6
Chapter 2: Background Information and Literature Review.....	8
2.1 Background of Gas Turbine Cooling Technology	8
2.2 Internal Cooling Technique.....	8
2.2.1 Pin Fin Cooling	9
2.2.2 Rib Turbulators in a Cooling Channel	9
2.2.3 Jet Impingement Cooling	10
2.3 External Cooling Technique Using Film Cooling.....	10
2.4 Jet Impingement Technique	12
2.5 Literature Review	14
2.5.1 Jet Impingement Cooling – Numerical Studies.....	14
2.5.2 Jet Impingement Cooling-Experimental Studies.....	22
Chapter 3: Numerical Formulation	30
3.1 Governing Equations	31
3.1.1 Continuity Equation	31
3.1.2 Momentum Equation (Navier-Stokes Equations)	31
3.1.3 Energy Equation.....	32

3.2 Turbulence Modeling	32
3.2.1 Turbulence Modeling Introduction	32
3.2.2 SST k - ω Model.....	33
3.3 Description of Physical Model.....	36
3.3.1 Assumptions	38
3.4 Meshing	41
3.4.1 Mesh Description	41
3.4.2 Wall Treatment Method	41
3.4.3 Grid Independent Study	43
3.5 CFD Solution.....	44
3.5.1 Discretization Scheme.....	44
3.5.2 Boundary Conditions	44
3.5.3 Solver Setting	47
3.5.4 Measure of Convergence.....	47
Chapter 4: Experimental Setup and Details	49
4.1 Overview of Experimental Setup	49
4.2 Test Facility.....	49
4.2.1 Test Rig Description.....	50
4.2.2 Compressed Air Supply	55
4.2.3 Hot Gas Simulation	58
4.2.4 Temperature Measurements	60
4.2.5 Camera and Lighting Setup.....	62
4.3 Test Section	63
4.4 Experimental Procedure	65
4.5 Validation Test Cases	66
Chapter 5: Results and Discussion.....	67
5.1 Validation	67
5.1.1 Temperature Contours Evaluation	68
5.1.2 Impingement Flow Behavior.....	76
5.2 Numerical Results for the Modified Test Section.....	86
5.2.1 Streamlines of Cross-Sectional Area for Each Jet	86
5.2.2 Center Plane Streamlines	95
5.2.3 Nusselt Number Contour.....	102
5.2.4 Nusselt Number Distribution on Facing Each Jet	110
5.2.5 Static Pressure Distribution Facing Each Jet.....	117
5.2.6 Static Pressure Variation on the Center Line	125
5.2.7 Nusselt Number Distribution on the Line	127
5.2.8 Averaged Local Nusselt Number Facing Each Jet.....	129
5.2.9 Mass Fraction for Each Individual Jet.....	131
5.2.10 Pressure Coefficient for Each Individual Jet.....	133
5.2.11 Correlation.....	135
Chapter 6 Conclusion and future work	137

6.1 Conclusions	137
6.2 Future work	139
References	140
List of Publications	145

List of Tables

Table 1: Dimensions and geometric model details	39
Table 2: Average Nusselt number for each case	43
Table 3: Properties of cooling air	45
Table 4: Domain and boundary conditions of the modeled leading edge	46
Table 5: Conversions residuals	48
Table 6: Setup components	54
Table 7: Case validation study	66

List of Figures

Figure 1: Gas turbine engine working principle	1
Figure 2: The ideal Brayton cycle for gas turbine engines	2
Figure 3: Power improvement by increasing turbine inlet temperature.....	3
Figure 4: Increasing turbine inlet temperature over the years.....	3
Figure 5: Various cooling techniques used in advanced turbine blade	8
Figure 6: Heat transfer distribution around the turbine blade	9
Figure 7: Film cooling in gas turbine blade	11
Figure 8: Impingement cooling.....	12
Figure 9: Typical jet impingement structure before and after impingement	13
Figure 10: Semicircular leading edge with rectangular supplied channel, (a) rectangular inlet supplied channel, (b) adopter connected to rectangular supplied channel used in the experiment for a CFD validation	38
Figure 11: Geometry and dimensions of the leading edge.....	40
Figure 12: Model with tetrahedrons mesh with 8 million elements.....	41
Figure 13: Boundary layer mesh on the target surface	43
Figure 14: Grid independent study for $Re_j = 5,000$ and $Re_j = 30,000$	44
Figure 15: Model description	46
Figure 16: Monitoring average Nusselt number on the target surface.....	48
Figure 17: Experimental setup overview	52
Figure 18: Actual experimental setup	53
Figure 19: Three supplied-air configurations.....	56
Figure 20: Cooling air outlet temperature for three different cases	57
Figure 21: Temperature distribution along the actual turbine rotor blade	59
Figure 22: Flexible heater arrangement	60
Figure 23: Liquid Crystal Calibration Hue vs. Temperature	61
Figure 24: Connecting thermocouples to datalogger through a slip ring.....	62
Figure 25: Target surface configuration with camera position	63
Figure 26: Experimental test section.....	64
Figure 27: Target surface temperature counters at 0 rpm is displayed using (a) CFD temperature contours, (b) experiment TLC image and (c) TLC calibrated contours	70
Figure 28: Target surface temperature counters at 50 rpm is displayed using (a) CFD temperature contours, (b) experiment TLC image and (c) TLC calibrated contours	71
Figure 29: Target surface temperature counters at 100 rpm is displayed using (a) CFD temperature contours, (b) experiment TLC image and (c) TLC calibrated contours	71

Figure 30: Target surface temperature counters at 150 rpm is displayed using (a) CFD temperature contours, (b) experiment TLC image and (c) TLC calibrated contours	72
Figure 31: Target surface temperature counters at 200 rpm is displayed using (a) CFD temperature contours, (b) experiment TLC image and (c) TLC calibrated contours	72
Figure 32: Centerline temperature distribution at 0 rpm.....	73
Figure 33: Centerline temperature distribution at 50 rpm.....	75
Figure 34: Centerline temperature distribution at 100 rpm.....	75
Figure 35: Centerline temperature distribution at 150 rpm.....	75
Figure 36: Centerline temperature distribution at 200 rpm.....	75
Figure 37: The mass flow rate fraction percentage for all jets.....	77
Figure 38: Center plane streamlines at $Re_j = 7,500$ at different rotational speed, (a) stationary, (b) 50 rpm, (c) 100 rpm, (d) 150 rpm, (e) 200 rpm	79
Figure 39: Streamlines of the jet cross sectional area, Row(a) Stationary, Row(b) 50 rpm, Row(c) 100 rpm, Row(d) 150 and Row(e) 200 rpm.....	81
Figure 40: Vector and streamlines for jet number 1 and 4 at 0 rpm	82
Figure 41: Vectors and streamlines for jet number 1 and 4 at the center plane at 0 rpm (stationary condition).....	83
Figure 42: Vector and streamlines for jet number 1 and 4 at 200 rpm	84
Figure 43: Vectors and streamlines for jet number 1 and 4 at the center plane at 200 rpm	85
Figure 44: Modification of the inlet for the supply channel	86
Figure 45: Streamlines on vertical cross section for jet number 1, 3, 5 and 7 for $Re_j = 7,500$ at different rpm.....	89
Figure 46: Streamlines on vertical cross section for jet number 1, 3, 5 and 7 for $Re_j = 10,000$ at different rpm.....	90
Figure 47: Streamlines on vertical cross section for jet number 1, 3, 5 and 7 for $Re_j = 15,000$ at different rpm.....	91
Figure 48: Streamlines on vertical cross section for jet number 1, 3, 5 and 7 for $Re_j = 20,000$ at different rpm.....	92
Figure 49: Streamlines on vertical cross section for jet number 1, 3, 5 and 7 for $Re_j = 25,000$ at different rpm	93
Figure 50: Streamlines on vertical cross section for jet number 1, 3, 5 and 7 for $Re_j = 30,000$ at different rpm	94
Figure 51: Streamlines on center plane for $Re_j = 7,500$ with different rpm, (a) stationary, (b) 250 rpm, (c) 500 rpm, (d) 750 rpm.....	96
Figure 52: Streamlines on center plane for $Re_j = 10,000$ with different rpm, (a) stationary, (b) 250 rpm, (c) 500 rpm, (d) 750 rpm.....	97
Figure 53: Streamlines on center plane for $Re_j = 15,000$ with different rpm, (a) stationary, (b) 250 rpm, (c) 500 rpm, (d) 750 rpm.....	98

Figure 54: Streamlines on center plane for $Re_j = 20,000$ with different rpm, (a) stationary, (b) 250 rpm, (c) 500 rpm, (d) 750 rpm.....	99
Figure 55: Streamlines on center plane for $Re_j = 25,000$ with different rpm, (a) stationary, (b) 250 rpm, (c) 500 rpm, (d) 750 rpm.....	100
Figure 56: Streamlines on center plane for $Re_j = 30,000$ with different rpm, (a) stationary, (b) 250 rpm, (c) 500 rpm, (d) 750 rpm.....	101
Figure 57: Nusselt number contours on the curved surface for Re_j of 7,500 with different rotation, (a) stationary, (b) 250 rpm, (c) 500 rpm and (d) 750 rpm	104
Figure 58: Nusselt number contours on the curved surface for Re_j of 10,000 with different rotation, (a) stationary, (b) 250 rpm, (c) 500 rpm and (d) 750 rpm	105
Figure 59: Nusselt number contours on the curved surface for Re_j of 15,000 with different rotation, (a) stationary, (b) 250 rpm, (c) 500 rpm and (d) 750 rpm	106
Figure 60: Nusselt number contours on the curved surface for Re_j of 20,000 with different rotation, (a) stationary, (b) 250 rpm, (c) 500 rpm and (d) 750 rpm	107
Figure 61: Nusselt number contours on the curved surface for Re_j of 25,000 with different rotation, (a) stationary, (b) 250 rpm, (c) 500 rpm and (d) 750 rpm	108
Figure 62: Nusselt number contours on the curved surface for Re_j of 30,000 with different rotation, (a) stationary, (b) 250 rpm, (c) 500 rpm and (d) 750 rpm	109
Figure 63: Local Nusselt number on the curved line facing each jet for $Re_j = 7,500$, (a) stationary, (b) 250 rpm, (c) 500 rpm, (d) 750 rpm	111
Figure 64: Local Nusselt number on the curved line facing each jet for $Re_j = 10,000$, (a) stationary, (b) 250 rpm, (c) 500 rpm, (d) 750 rpm	112
Figure 65: Local Nusselt number on the curved line facing each jet for $Re_j = 15,000$, (a) stationary, (b) 250 rpm, (c) 500 rpm, (d) 750 rpm	113
Figure 66: Local Nusselt number on the curved line facing each jet for $Re_j = 20,000$, (a) stationary, (b) 250 rpm, (c) 500 rpm, (d) 750 rpm	114
Figure 67: Local Nusselt number on the curved line facing each jet for $Re_j = 25,000$, (a) stationary, (b) 250 rpm, (c) 500 rpm, (d) 750 rpm	115
Figure 68: Local Nusselt number on the curved line facing each jet for $Re_j = 30,000$, (a) stationary, (b) 250 rpm, (c) 500 rpm, (d) 750 rpm	116

Figure 69: Local static pressure at the curved line facing each jet for jet Reynolds of 7,500, (a) stationary, (b) 250 rpm, (c) 500 rpm, (d) 750 rpm	119
Figure 70: Local static pressure at the curved line facing each jet for jet Reynolds of 10,000, (a) stationary, (b) 250 rpm, (c) 500 rpm, (d) 750 rpm	120
Figure 71: Local static pressure at the curved line facing each jet for jet Reynolds of 15,000, (a) stationary, (b) 250 rpm, (c) 500 rpm, (d) 750 rpm	121
Figure 72: Local static pressure at the curved line facing each jet for jet Reynolds of 20,000, (a) stationary, (b) 250 rpm, (c) 500 rpm, (d) 750 rpm	122
Figure 73: Local static pressure at the curved line facing each jet for jet Reynolds of 25,000, (a) stationary, (b) 250 rpm, (c) 500 rpm, (d) 750 rpm	123
Figure 74: Local static pressure at the curved line facing each jet for jet Reynolds of 30,000, (a) stationary, (b) 250 rpm, (c) 500 rpm, (d) 750 rpm	124
Figure 75: Local static pressure on line A-A (center line) for jet Reynolds number of (a) 7,500, (b) 10,000, (c) 15,000, (d) 20,000, (e) 25,000 and (f) 30,000	126
Figure 76: Nusselt number on line A-A (center line) for jet Reynolds number of (a) 7,500, (b) 10,000, (c) 15,000, (d) 20,000, (e) 25,000 and (f) 30,000	128
Figure 77: Average Nusselt number on the curved line facing each jet for jet Reynolds number of (a) 7,500, (b) 10,000, (c) 15,000, (d) 20,000, (e) 25,000 and (f) 30,000	130
Figure 78: Average mass fraction passing each jet for different jet Reynolds numbers of (a) 7,500, (b) 10,000, (c) 15,000, (d) 20,000, (e) 25,000 and (f) 30,000	132
Figure 79: Pressure coefficient facing each jet for different jet Reynolds numbers of (a) 7,500, (b) 10,000, (c) 15,000, (d) 20,000, (e) 25,000 and (f) 30,000	134
Figure 80: Correlation fit with computation results	136

List of Abbreviations

2D	Two dimension
3D	Three dimension
A	Cross-sectional area, (m^2)
ACF	Anti cross flow
CFD	Computational fluid dynamics
Cp	Pressure coefficient
D	Diameter, (m)
DSC	Double swirl chamber
j	Jet
LE	Leading-edge
n	Number of jets
Nu	Nusselt number
P	Pressure, (Pa)
Pr	Prandtl number
q	Heat, (J)
R	Rotating arm radius, (m)
Re	Reynold number
Roj	Jet rotation number, $Roj = (\Omega \cdot d_j / v_j)$
rpm	Rotation per minute
RSM	Response surface methodology
SST	Shear stress transport
t	Jet thickness, (m)
T	Temperature, (K)
TIT	Turbine inlet temperature, (K)

TLC	Thermochromic liquid crystal
v	Velocity, (m/s)
W	Work, (J)
w	Supplied channel width, (m)

Symbols:

η	Thermal performance
ω	Specific dissipation rate, $(1/s)$
μ	Dynamic viscosity, $(Pa.s)$
ε	Turbulence dissipation rate, (m^2/s^3)
ρ	Density, (kg/m^3)
Ω	Angular velocity, (m/s)
s	Jet to jet distance, (m)
l/d_j	Jet to target distance

Subscripts:

<i>avg</i>	Average
<i>c</i>	Curved Target
<i>ch</i>	Channel
<i>H</i>	Hydraulic
<i>in</i>	Inlet
<i>j</i>	Jet
<i>LE</i>	Leading-edge
<i>n</i>	Number of jets
<i>out</i>	Outlet

Chapter 1: Introduction

1.1 Background

Gas turbine engines and their cooling system are described in this chapter. Gas turbine engines are widely used for aircraft propulsion, land-based power generation, marine vessels, military tanks, and helicopter power. The working principle of a gas turbine engine is shown in Figure 1. Fresh air enters the compressor as the air pressure and the temperature increase in each compressor stage. Then compressed air enters the combustion chamber and mixes with the fuel. The fuel is combusted in the presence of compressed air, producing high thermal energy and raises the gas temperature to around 2000 K in advanced gas turbine engines. The hot gas leaves the combustion chamber at a high temperature and moves toward the turbine. The turbine blades convert the enthalpy of the gas to work in gas turbine engines. This work generates power to propel vehicles, like marine vessels, military tanks, and helicopters. Moreover, the gas's high enthalpy is converted into kinetic energy in gas turbine engines used for aircraft propulsion. The gas turbine engines follow an ideal Brayton cycle shown in Figure 2.

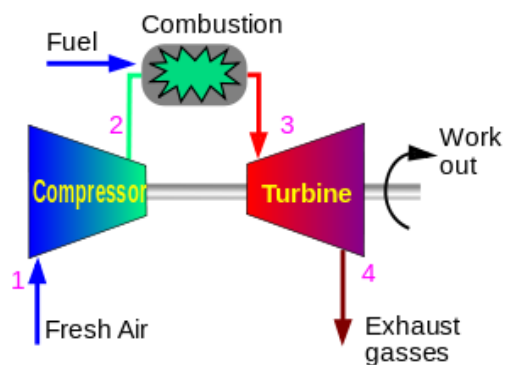


Figure 1: Gas turbine engine working principle [1]

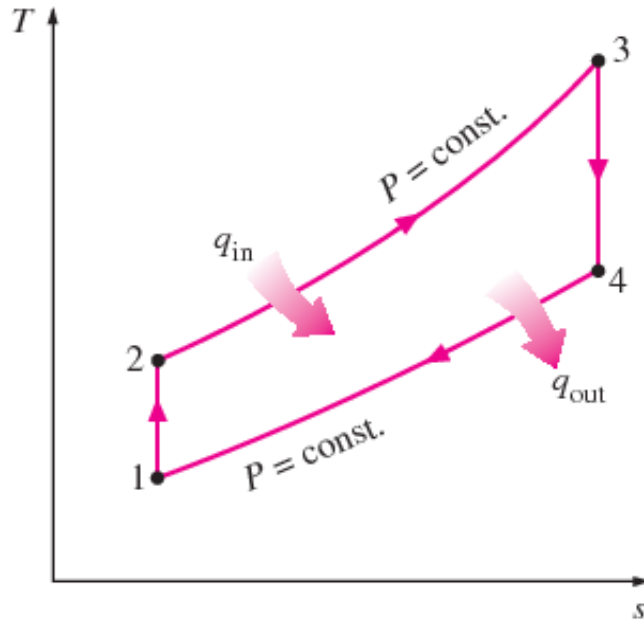


Figure 2: The ideal Brayton cycle for gas turbine engines [1]

The Brayton cycle's thermal efficiency primarily depends on the turbine inlet temperature (TIT), T_3 indicates in Figure 2. The efficiency is calculated based on the following formula [2]:

$$\eta_{th,Brayton} = \frac{w_{net}}{q_{in}} = 1 - \frac{q_{out}}{q_{in}} = 1 - \frac{(T_4 - T_1)}{(T_3 - T_2)} \quad (1)$$

As shown in Equation (1), increasing the turbine inlet temperature (T_3) increases the engine's thermal efficiency and power output. Figure 3 presents how turbine inlet temperature strongly affects power output. In modern gas turbine engines, the turbine inlet temperature is relatively high (around 2000 K), allowing high thermal efficiencies. Due to turbine material integrity limitations, designers have implemented a sophisticated cooling technique in turbine blades to protect the turbine integrity, prolonging its life. Therefore, cooling from the high-pressure compressor stage bleeds some compressed air. While the bled air decreases compressor efficiency, it

accommodates a high turbine inlet temperature, improving the gas turbine's efficiency. Therefore, adopting an efficient cooling technique can minimize gas turbine fuel consumption. Figure 4 displays the trends of using various cooling techniques in turbine blades since 1950. It illustrates improved cooling techniques can enhance the turbine inlet temperatures (TIT), improving the gas turbine engines' thermal efficiency.

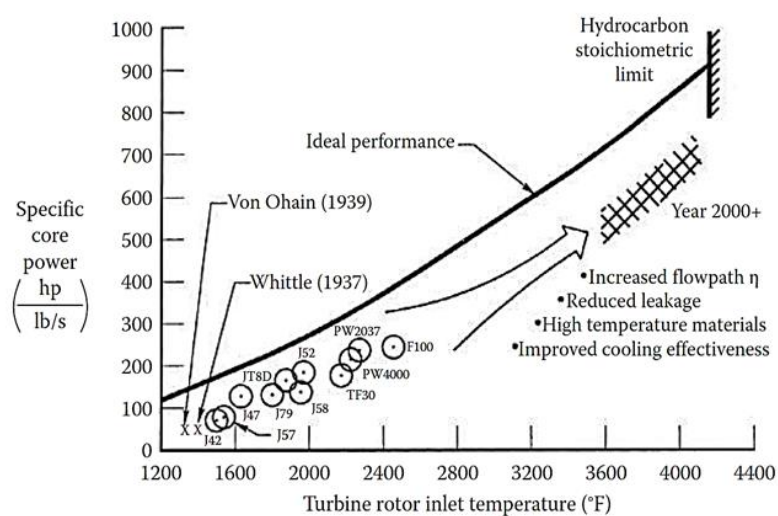


Figure 3: Power improvement by increasing turbine inlet temperature [3]

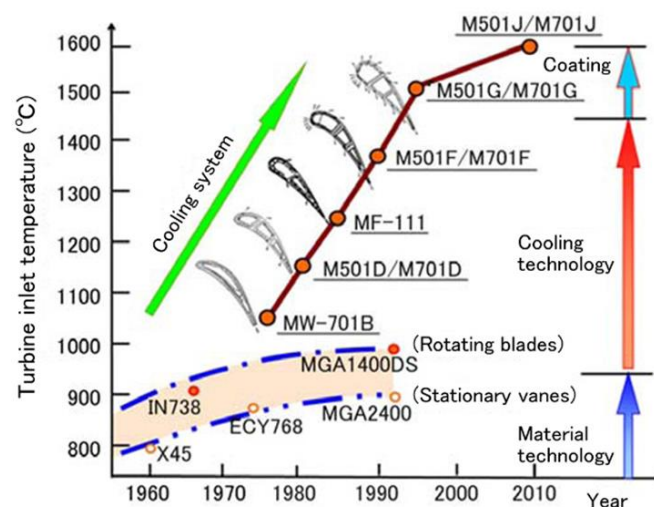


Figure 4: Increasing turbine inlet temperature over the years [1]

1.2 Problem Statement

The primary focus of this thesis is to study how blade rotation affects cooling capabilities. If rotation negatively influences cooling, one needs to consider using more cooling air than the stationary condition or possibly redesigning the cooling system orientation to account for blade rotation. This study will quantitatively answer how blade rotation impacts the blade jet impingement cooling performance. Therefore, to answer this question, numerical and experimental investigations are performed for different turbulent Reynolds numbers at different rotating conditions. For the numerical analysis, a turbulent SST $k-\omega$ model is employed. Furthermore, to trust and validate the numerical results, two temperature methods are used: thermochromic liquid crystal and thermocouples. The validation is achieved by comparing the experimental measurements to the CFD results of a similar geometrical case. The thermocouples and the liquid crystal measurements are focused on the centerline of the leading edge. Following the successful validation, the primary leading edge's design's vulnerability is observed; however, for the parametric numerical studies, the leading edge is redesigned before progressing with the research.

1.3 Hypothesis and Novelty Statement

Jet impingement exemplifies an efficient cooling technique for a gas turbine blade. The rotation number, Reynolds number, crossflow, jet configuration, and jet interaction were the main factors impacting the gas turbine blade's impingement cooling performance. This work aims to experimentally and numerically explore the leading-edge's cooling performance and to examine the effect of different parameters on jets impingement cooling, primarily the Reynolds number and the rotation number.

The present work contributes to the knowledge base, namely through the following points:

- 1) A 3D (three dimensional) numerical simulation using SST $k-\omega$ turbulence model was implemented to capture jet complex flow behavior, which was challenging to attain experimentally. The numerical simulation shed more light on the jet interactions with the curved surface and other jets, and how it plays a significant role in the cooling performance.
- 2) A novel correlation is establish in this study that relates jet Nusselt number to jet Reynolds number and jet rotation number. This correlation is of great importance for gas turbine designers who needs to account for the thermal management of jet impingement under rotation.
- 3) The present work shows the feasibility of SST $k-\omega$ turbulence model to analyze jet flow under rotation. Hence, the study open the door for CFD engineer to use such model for jet impingement under rotation condition. Based on current literature, this study is the first study that proves the ability of SST $k-\omega$ model to model jet impingement under rotation condition.
- 4) A unique test facility have been built in this study. Based on current literature, this unique setup is one of three setups in the world that can analyze rotating jet impingement. The UAE University test setup is a unique one since it combines two measuring thermal tools, namely the thermocouple measurements and the liquid crystal technique.

- 5) The hypothesis was tested numerically and validated experimentally to determine the effect of critical factors such as rotation and Reynolds number.

1.4 Thesis Objectives

This thesis principally aims to study the cooling performance of a gas turbine blade leading edge using jet impingements under various Reynolds numbers and rotating velocities. This study is carried out numerically and validated experimentally. The numerical simulation uses ANSYS FLUENT 15.0, a commercial computational fluid dynamics (CFD) tool. The SST $k-\omega$ turbulence model was adopted to simulate a 3D model of seven jets impinging on a semi-circular channel. An experimental setup, designed and built at United Arab Emirates University, was used for validation. The experimental setup consists of a semi-circular channel that was internally cooled with seven impingement jets which were subjected to a controlled flow and rotating configuration. A parametric 3D numerical simulation, covering a wide range of Reynold numbers and rotation numbers, had been used to examine the flow structure and thermal behaviour of impingement cooling.

1.5 Thesis Organization

This thesis presents a comprehensive experimental and numerical study of impingement cooling on a rotating leading-edge applied on the curved surface. The thesis starts with Chapter 1, introducing the problem statement, the novelty statement and the main objectives.

Chapter 2 presents the prevailing empirical literature findings and describes the experimental and numerical background of gas turbine blade cooling theory, focusing on jet impingement cooling.

Chapter 3 introduces the methodology followed in the numerical simulation, including the geometry, generation of mesh, the adopted turbulence model, and assigning the boundary conditions. Additionally, two Reynolds numbers are studied for the mesh independent analysis. Based on the literature review, *SST $k-\omega$* turbulence model is employed for CFD analysis which presents the most effective and accurate turbulence model for impingement flow.

Chapter 4 discusses and illustrates the experimental equipment, working conditions, setup instrumentation, testing procedure, tested cases, experimental limitations.

Chapter 5 includes the results of the numerical investigation, clearly demonstrating the contour plots of Nusselt number, local Nusselt number distribution, local pressure distribution, local and overall flow behavior, jet mass fraction, pressure coefficient, and normalized Nusselt number at both stationary and rotating conditions for six Reynolds numbers. Also, the correlation CFD results using the least-squares method is exhibited. The correlation indicates how the overall Nusselt number changes with the jet Reynolds number at various rotating conditions.

Finally, Chapter 6 concludes with the key findings and proposes future work.

Chapter 2: Background Information and Literature Review

2.1 Background Information of Cooling Technology of Gas Turbine Engines

Modern gas turbine engines work at high temperatures (~ 2000 K) to improve thermal efficiency and power output. Given that operating temperature is much higher than the blade material melting point, therefore it needs cooling. In gas turbine engines, various cooling techniques are used for cooling the blades to maintain their integrity. Blade cooling methods comprise internal and external as discussed in the following sections [4].

2.2 Internal Cooling Technique

Forcing cooling air extracted from the compressor stages into the serpentine channels are used for cooling the turbine blades. Various approaches (jet impingement cooling, tip cap cooling, pin fins, and rib turbulators, etc.) can enhance this cooling technique, as shown in Figure 5.

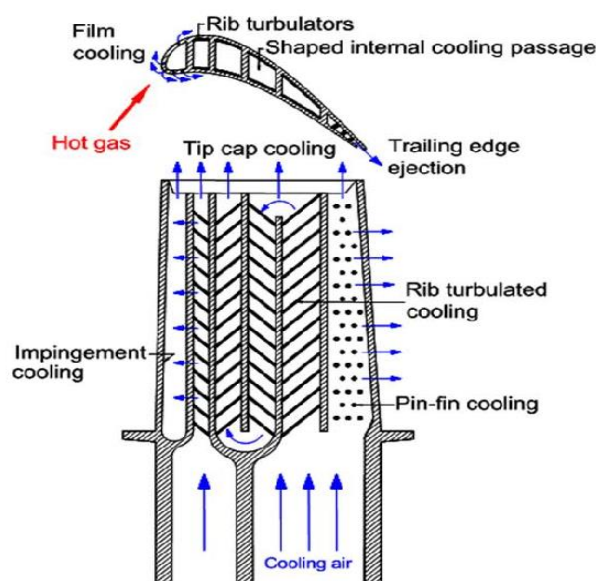


Figure 5: Various cooling techniques used in advanced turbine blade [5]

2.2.1 Pin Fin Cooling

Figure 6 displays the highest heat transfer rate on the leading and the trailing edge. In most advanced cooling turbine blades, implementing a serpentine cooling channel into the blades is not suitable due to its thin cross-section. Therefore, at the trailing edge, a pin fin cooling technique properly cools, as shown in Figure 5. Pins increase surface area and enhance the flow mixing at the trailing edge, consequently, leads to increase the heat transfer rate. Pin fin cooling depends on several factors, such as pin fin shape, configuration, and pin arrangements, and number of pins.

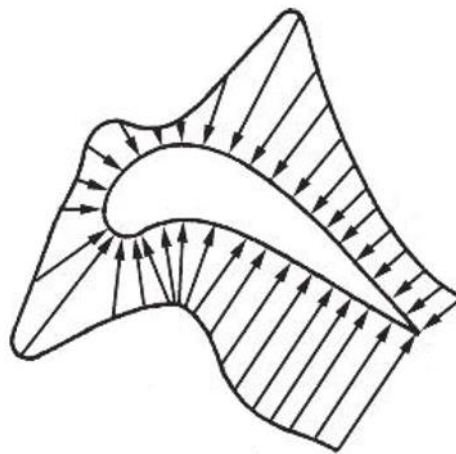


Figure 6: Heat transfer distribution around the turbine blade [6]

2.2.2 Rib Turbulators in a Cooling Channel

As shown in Figure 5, advanced gas turbine blades contain a serpentine channel for cooling where the air passes through it to remove the heat from the surface. Similar to the pin fin cooling technique, rib turbulators enhance the heat transfer in the cooling channel, increasing the contact surface with the cooling air and heat transfer coefficient. Some essential factors, like rib configurations and the flow Reynolds

number, need to be considered in this cooling process. Due to the centrifugal and the Coriolis force, rotation significantly impacts the flow inside the channel; therefore, the flow field inside the stationary cooling channels differs from the rotating conditions required to evaluate the rotational effect on rib turbulator technique [4].

2.2.3 Jet Impingement Cooling

The most critical region of turbine blades is the leading edge, where the highest thermal load exists. Therefore, choosing a proper cooling method for this region is very important. Due to the size limitation of the leading edge, implementing a serpentine channel is not possible; therefore, designers are employed other techniques that can be used for this position. Jet impingement cooling is the most powerful cooling method within all cooling techniques in gas turbine blades. This method also can be used in the mid-chord of the blade. Many research groups have investigated jet impingement cooling technique and tried different approaches to improve its cooling performance. Recently, researchers and engineers started to look at the effect of jet location and the blade rotational speed. The method will be explained in detail in the jet impingement technique section of this chapter.

2.3 External Cooling Technique Using Film Cooling

Film cooling is an external technique achieved by employing small holes on the blade surface, creating a thin layer of relatively cool air on the surface that absorbs external heat and shields the blade from external hot gases. The cool air is taken from the compressor and pumped through the cooling channels inside the blade, eventually leaving the blade through small and discrete holes manufactured on the surface. The air will be mixed with the hot gas and passes through the turbine section. Figure 7

shows that cooling air leaves the blade from the leading edge and the trailing edge through small film holes. The red track clearly shows a serpentine channel. As shown in the same figure, high-pressure cooling air is used for the leading edge and the middle of the turbine blade, while low pressure is used for the trailing edge. Due to the turbine blades' working principle, the gas pressure is lower than the leading edge due to the gas expansion at the trailing edge.

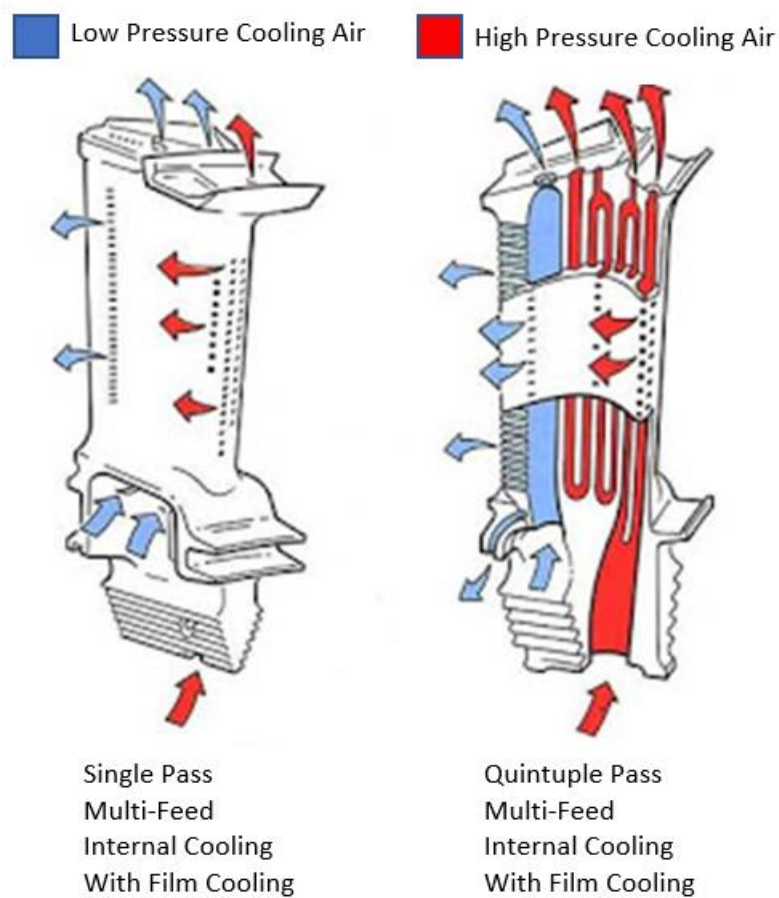
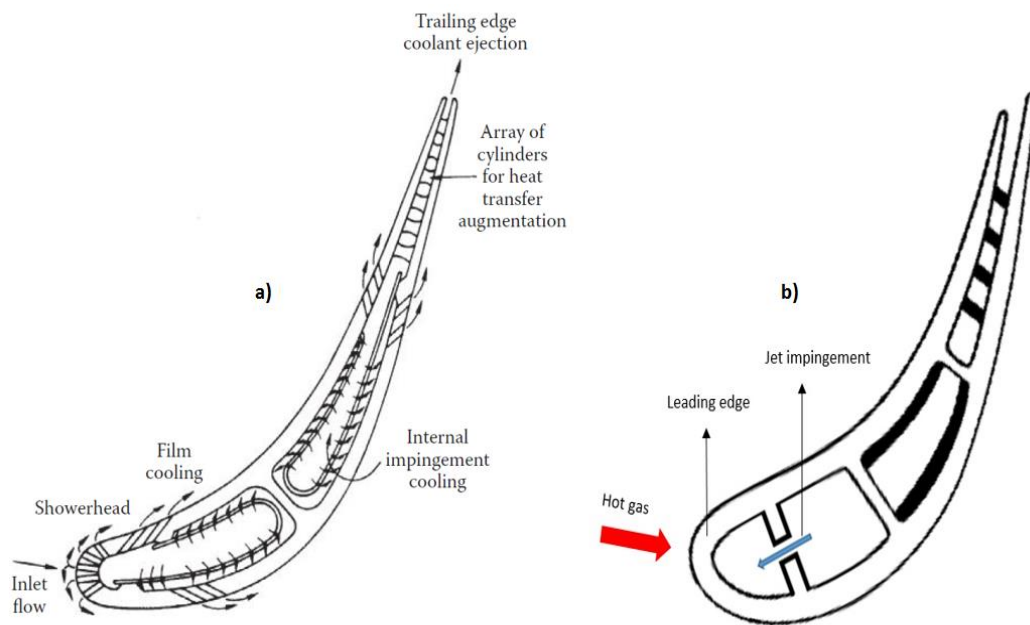


Figure 7: Film cooling in gas turbine blade [7]

2.4 Jet Impingement Technique

Jet impingement cooling method effectively cools, by impinging cooled air on the curved surface. However, due to the rotating turbine blade and fabrication complexity's structural limitation, this technique is only implemented on the rotating blades' leading edge [4]. On the other hand, stationary vanes can use the same technique around the mid-chord since they have a thicker cross-section compared to the rotating blades. Figure 8 shows the impingement method used in the rotating and stationary turbine blades.



a) mid-chord of turbine inlet vane b) the leading edge of a rotating blade.

Figure 8: Impingement cooling [8]

Creating a very thin boundary layer and the turbulent flow at the stagnation area using jet impingement causes extremely high heat removal at the region. Cooling air leaves the jet hole with a high velocity and impinges on the target surface. Figure 9 details jet impingement.

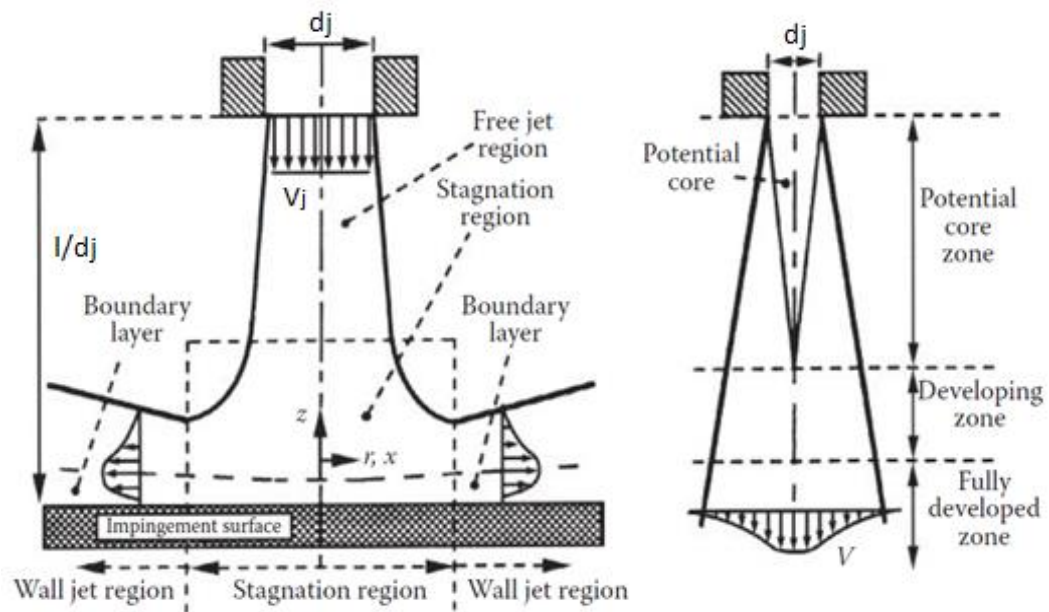


Figure 9: Typical jet impingement structure before and after impingement [9]

As shown in Figure 9, jet impingement on the target surface creates a stagnation region. Essential differences exist in the flow characteristics before and after striking the target surface. In gas turbine's internal cooling application, the jet flow impinges on the target surface, expelling a relatively cool turbulent airstream. Typically, constrained jets (where the jet is confined within a cavity) and submerged jets (where the injected fluid is the same as the fluid throughout the cooling channels) are similarly cool. Conventionally, the impinging jet structure consists of three parts. Potential core region, where the viscous forces do not affect the velocity profile. Shear layer region, where the viscous forces impact the shear layer as the jet discharges, causing the jet to expand and develop. Wall jet region, where the jet flow impinges on the target surface, the wall jet forms and develops along the wall.

Many scholars have discussed the jet behavior considering various parameters, including:

- Jet to target distance, l/d_j .
- Jet diameter, d_j .
- Jet to jet distance, s/d_j .
- Optimum number of jet holes, n .
- Jet configuration; (inline, staggered, double, circle, etc).
- Target surface roughness.
- Blade rotation.

2.5 Literature Review

2.5.1 Jet Impingement Cooling – Numerical Studies

Several investigators conducted a numerical studies on jet impingement cooling, concluded that the heat transfer performance is enhanced in the turbine blade's leading edge. Many quantitative investigators have explored jet impingement cooling for stationary and rotating blades. In 2010, Liu et al. [10] performed a three dimensional numerical investigation of flow and heat transfer performance concerning jet impingement cooling. Three turbulent models are used in their numerical study. They employed the standard $k-\omega$ turbulence model, RNG $k-\varepsilon$ model, and the combination of both turbulent models known as $k-\omega$ Shear Stress Transport (SST). Liu et al. validated their results with the experimental study performed by Bunker et al. [11] and reported the SST $k-\omega$ turbulent model as the most accurate and suitable turbulent model for jet impingement yielding a relative error of 13.58% compared to the experimental data reported in reference [11]. For grid-independent analysis, four numerical mesh elements from 1.3 million to 4.3 million are employed. Using the

Richardson extrapolation, they concluded 4.3 million nodes have a relative error of 0.74%. The study showed that by increasing jet diameter (d_j), the Nusselt number at the leading edge increase. Liu et al. [12] numerically studied jet location impact on leading edge cooling efficiency. Five jet locations are considered in the study with a single row of 14 round circular jets. They revealed the average Nusselt number at the leading edge increased as the jet Reynolds number increased. Also, they demonstrated that by reducing jet to target distance (l/d_j), the local Nusselt number increased.

Lin et al. [13] introduced a new cooling chamber design for the leading edge: double swirl chamber (DSC), reducing the crossflow (the accumulated spent air each jet creates inside the chamber toward the outlet), and increasing the jet effect on the leading edge. After testing turbulent models, like SST $k-\omega$, Realizable $k-\varepsilon$, standard (Wilcox) $k-\omega$, V^2f , and Spalart Allmaras. Lin et al. [13] compared their results with the experimental data obtained by Yang et al. [14], and they discovered the turbulent model SST $k-\omega$ predicts better than the other two tested turbulence model. The grid-independence study is conducted for each turbulence model with three numerical element sizes varying from 1 million to 5 million. Eventually, they used three million elements for their numerical study. The value of dimensionless wall distance (y^+) as an essential parameter for SST $k-\omega$ turbulent model for all cases achieved less than the unity ($y^+ < 1$). They reported the newly designed DSC increased the Nusselt number by 24% compared to the single inline jets. Also, rectangular jet configuration performed better than the round jets in DSC. In 2014, Yang et al. [14] numerically and experimentally studied unsteady impingement cooling on the leading edge. They used a single row of ten circular jets to evaluate jet impingement heat transfer. The jet Reynolds number (Re_j) varied from 10,000 to 20,000. They performed an analysis

using steady and unsteady SST $k-\omega$ and RNG $k-\epsilon$ turbulent model. An experimental investigation using a thermochromic liquid crystal (TLC) is employed to validate the numerical results. The turbulent model for both steady and unsteady cases is adopted as SST $k-\omega$. According to their investigation, the crossflow significantly affects the surface Nusselt number. Liu et al. [15] experimentally and numerically explored the effect of tangential jet impingement on the leading edge. They investigated the characteristics of flow and heat transfer of jet impingement on a concave surface, using transient thermochromic liquid crystal (TLC) with jet Reynolds numbers varying from 12,000 to 20,000 to validate the numerical computations. Various tangential jets are adjusted from the centerline of the concave surface. Liu et al. [15] tested three turbulence models for their numerical study. The comparison between realizable $k-\epsilon$, SST $k-\omega$, and $V2f$ turbulent model showed SST $k-\omega$ provided better matching with the experimental data. They concluded the jet Reynolds number and the jet nozzle position significantly effect on the heat transfer performance. Moreover, at jet Reynolds number less than 15000, the tangential jet improved heat transfer while $Re_j = 20,000$ yielded a negative effect on heat transfer enhancement from the tangential jet. They concluded as the jet Reynolds number increased, the Nusselt number on the concave surface increased due to the higher jet velocity. They revealed no significant effect for Reynolds number less than 15,000 for various jet nozzle positions, while more pronounced differences occurred at higher Reynolds numbers where the jet nozzle is located to the side.

Hamdan et al. [16] studied numerically and experimentally the tangential jet impingement on the curved target surface; employing three turbulence models such as $k-\epsilon$, $k-\omega$ and the Reynolds Stress Model (RSM). The RSM turbulent model found a

good agreement with experiment. Elnajjar et al. [17, 18] compared two impingement configurations experimentally: central impingement jets and side impingement under constant heat flux on the target curved surface. The range of the jet Reynolds number varied from 500 to 5000. The average surface Nusselt number and drag coefficients are used to evaluate the performance of each case. They reported that the central impingement design provides much better cooling performance up to 50% compared to the side located jet. Al-Hemyari et al. [19] numerically studied the effect of centrifugal force by impingement jet on the flat surface in 2D problem. The RNG k - ε turbulence model with enhanced wall function is employed in their numerical investigation. They reported centrifugal force alters impingement jet which makes overheating around the impingement area. Al-Hemyari et al. [20] numerically investigated jet impingement optimization using statistical model called response surface methodology (RSM) in 2D. Three parameters are involved in their study such as blowing ratio, jet angle and density ratio. They reported the optimum value of each parameter which provides the highest adiabatic film cooling effectiveness (AFCE). Lebiary et al. [21] experimentally and numerically assessed jet impingement cooling efficiency using different outlet flow directions from the leading edge cavity. They focused on heat transfer on the leading edge using three designs. In the first strategy, they let flow leave in the same direction as the incoming flow, while for the second design, the flow left the cavity in the opposite direction of the incoming flow. In the third approach, the flow left the leading-edge cavity from both directions. The realizable turbulent model k - ε with enhanced wall function is employed for numerical computations with turbulent jet Reynolds numbers ranging from 8,000 to 55,000. They pointed out the crossflow significantly affects the heat transfer coefficient. It deflected

the jet from its track to the concave surface, although the sides' heat removal improved. In the second design, the highest Nusselt number is at the target surface center. Taslim et al. [22] evaluated the surface roughness impact on jet impingement using smooth and roughened leading-edge target surfaces. They employed three designs for the target surface: smooth, notched horseshoe, and horseshoe target. Their study's numerical turbulence model entailed k - ϵ , and the range of jet Reynolds numbers varied from 10,000 to 50,000. They unveiled the highest impingement heat transfer rate on a smooth surface, followed by a notched-horseshoe, and lastly, a horseshoe roughened. However, overall heat transfer improved by 27% on a roughened surface, demonstrating the primary effect of ribs on the overall cooling compared to the smooth surface in the leading edge. Taslim et al. [23] numerically and experimentally studied the effect of showerhead holes on impingement cooling, used in the blade leading edge. They focused on heat transfer enhancement on the blade nose and the curved surface's sides (the pressure side and the suction side). The jet Reynolds number varied from 8,000 to 48,000. Based on their conclusion, having showerhead holes significantly enhances the surface's heat transfer. The standard k - ϵ turbulent model is employed in the numerical investigation. This comparison reveals a good agreement for the no-showerhead hole with a 10% discrepancy and about 30% difference with a showerhead holes.

Rao [24] experimentally and numerically explored how pin fin design impacts on jet impingement cooling. The jet Reynolds number ranged from 15,000 to 30,000. Two roughened surfaces attached with high and short pin-fins are employed in their study. Also, impingement cooling on the smooth surface without pins is conducted to compare with pin surfaces. They concluded that the full height pin-fin enhanced

overall heat transfer by 32.3% and increased channel pressure loss by 18%. Wang et al. [25] investigated numerically and experimentally turbine blade cooling with a single row at various jet impingement positions. The jet Reynolds number varied from 10,000 to 30,000, and TLC is used for the experimental validation. They used 12 round jets for cooling with tangential impingement. Two turbulence models, realizable $k-\varepsilon$ (RKE) and SST $k-\omega$ are examined. The results showed that the RKE approach had a better prediction capabilities than the SST $k-\omega$ model. Based on their findings, increasing the jet Reynolds number increased the local Nusselt number. Also, tangential jets improved uniform temperature contour on the leading edge; however, both arrangements produced similar overall Nusselt numbers. Fechter et al. [26] assessed impingement cooling with a narrow channel design. The numerical study implemented an experimental design to validate this, investigating the jet-to-target distance (H/D) and staggering jet position effect. A single row of five impingement holes is embedded inside the narrow channel for analysis. The Reynolds number for the numerical and experimental analysis varied from 15,000 to 40,000. According to their results, inline arrangement transferred heat best while changing impingement jet position decreased the Nusselt number. Furthermore, staggering the jets reduced the overall heat transfer, while in the CFD, both cases had a similar heat transfer. The turbulence SST $k-\omega$ model is used for the numerical investigations, and they found a good agreement with experimental data for overall Nusselt number distribution. However, in the stagnation region, the discrepancy remained around 30%.

Chi et al. [27] designed a new impingement cooling method to prevent a negative crossflow on heat removal rates. The anti-cross flow (ACF) impingement technique reduces channel crossflow's adverse effect, improving heat transfer. The

experimental study used the TLC technique. They employed numerical analysis for (CFD) SST $k-\omega$ turbulence model with a 7.8% error compared to the experimental results. They concluded that the ACF impingement significantly reduced the target surface temperature, insignificantly affecting the pressure drop. Zhou et al. [28] numerically investigated high-temperature differences influencing jet impingement cooling. The V^2f turbulent model, employed in their numerical study, is validated with available experimental data obtained by Baughn et al. [29]. In their study, they investigated the effect of density and the thermal property. Density decreased due to high temperature, lowering heat transfer. Also, increasing any of these properties enhanced heat transfer performance. Penumadu et al. [30] numerically scrutinized pressure drop and heat transfer for multiple jet impingement cooling, implementing various numerical models: Reynolds average Navier-Stokes (RANS) and Large Eddy Simulation (LED). These approaches are validated by comparing the findings with experimental data. The discrepancy in the heat transfer coefficient between CFD results and experimental results is around 10%. According to their findings, contraction at the nozzle entrance and less kinetic energy at the nozzles generated significant pressure loss. They also clogged the jet to create the highest local heat transfer. The overall heat transfer decreased by 6%, and the pressure dropped by 15%.

Wan et al. [31] conducted experimental and numerical studies on impingement cooling for a flat plate, using two roughened surfaces with inline and staggered pin fins. The Reynolds number ranged from 15,000 to 35,000. The turbulent SST $k-\omega$ is employed in their numerical study and found it to agree very well with experimental data. They concluded that inline pin fins on the plate significantly affected the transfer rate, improving the overall heat transfer by 34.5% compared to the casflat plate case.

According to their findings, inline pin fins performed better than staggered pin fins. Liu et al. [32] numerically explored jet impingement cooling with film holes on the target surface. The numerical study is validated by available experimental results [11, 33]. The turbulence model SST $k-\omega$ is employed in their numerical simulations, and the results agreed with the experimental data. As they reported, increasing the blowing ratio, the coolant mass ratio to the mainstream, and the heat transfer rate increased. Also, the film holes angle significantly impacted the heat transfer rate. Based on the available literature and the author's knowledge, few experts have examined a numerical simulation of jet impingement cooling considering blade rotation. Burberi et al. [34] performed numerical and experimental investigation for jet impingement cooling for a rotating gas turbine blade leading edge. They studied rotation's influence on the internal heat transfer coefficient. The large eddy simulation (LED) turbulence model is employed for their numerical computations. The test consists of three impinging jets and six rows of film holes, with four extraction holes on each row. According to their conclusions, the rotation significantly affected the Nusselt number distribution over the surface. They also reported that rotation does not significantly influence the local jet Nusselt number, and it only shifted each impingement jet's peak value.

Simone Paccati et al. [35] numerically investigated the effect of rotation and jet configuration on impingement cooling. Two jet arrangements and diameters are considered with the same passage area. For each case, a simulation is performed at the stationary and rotating conditions for the turbulent Reynolds number $Re_j = 8200$. Two approaches such as Reynolds Average Navier Stocks (RANS) and Scale Adaptive Simulation (SAS), are tested, and SAS is adopted for their study. They reported the

rotational effect altered jets laterally and negatively affected heat transfer slightly. This effect is observed in numerical and experimental studies. Safi et al. [36] numerically studied the effect of rotation on jet impingement cooling. The Reynolds number varied from 7,500 to 30,000 in their numerical investigation, and the turbulent SST $k-\omega$ is used in their study. Mesh independent studies are conducted for two Reynolds numbers based on the overall Nusselt number on the target surface. They concluded that the rotation has a minor negative effect on cooling performance and offered a Nusselt number correlation based on the jet Reynolds number, and the jet rotation number. Also, they showed that impingement jets highly get affected by rotation and the crossflow. In another numerical study, Safi et al. [37] investigated the effect of angular velocity on mass flow rate for rotating impingement leading edge. Turbulent jet Reynolds numbers varied from 7,500 to 30,000. Also, the rotation ranged from 0 to 750 rpm. They concluded that the rotation significantly affected the mass flow rate at low Reynolds number while at high Reynolds number, the effect of rotation is diminished.

2.5.2 Jet Impingement Cooling-Experimental Studies

Researchers have conducted several experimental studies on jet impingement cooling techniques with and without rotation. Chupp et al. [38] conducted the earliest parametric investigation on jet impingement, exploring the effect of a curved surface on heat transfer. Based on their conclusion, the Nusselt number of the target surface increased by decreasing jet-to-target distance (l/d_j) and increasing jet Reynolds number (Re_j). Finally, they demonstrated increasing target curvature-to-jet diameter (D/d_{jet}) positively impacted the target surface Nusselt number. They finalized the following correlation for the leading edge Nusselt number:

$$Nu = 0.44 Re_{jet}^{0.7} \left(\frac{d}{s}\right)^{0.8} \exp \left[-0.85 \left(\frac{l}{d}\right) \left(\frac{d}{s}\right) \left(\frac{d}{D}\right)^{0.4} \right] \quad (2)$$

Goldstein and Behbahani [39] experimentally studied the effect of crossflow and Reynold number on jet impingement heat transfer. The effect of jet to target distance (l/d_j) is also considered in their experimental investigation. They employed a flat plate with 12.7 mm diameter jet holes as a target surface. As they reported, increasing jet to target distance (l/d_j), crossflow dominated the jets, shifting the Nusselt number jets' peak on the target surface. Kercher and Tabakoff [40] examined impingement jets on heat transfer influence on the flat surface, considering crossflow. Their experimental data developed a correlation of heat transfer performance of jet impingement under crossflow. They also concluded that as the distance between jets to the target plate (l/d_j) decreased, the heat transfer increased. They also reported the crossflow (the spent air accumulating inside the chamber created) decreased local jet heat transfer due to altering and shifting the jets away from the target surface. Based on their conclusion, increasing the number of jets while having the same mass flow rate improves heat transfer. Florschuetz et al. [41] experimentally and theoretically (2D model) studied heat transfer distribution of a single row of multiple jets and staggered impingement holes considering parameters such as streamwise spacing, spanwise spacing, and channel height. They developed an experimentally verified correlation for the crossflow effect. The researchers reported that crossflow had more strength in staggered holes than a single row of multiple jets. The effect of surface curvature is a significant consideration to jet impingement thermal performance. Fenot et al. [42] experimentally studied the effect of high relative curvature defined as (d_j/D_{ch}) on heat transfer efficiency of jet impingement cooling, using parameters, such as jet Reynolds

number, jet temperature, jet to jet spacing (s/d_j), and jet-to-target distance on relative curvature. The scholars stated the relative curvature had two opposite effects on impingement cooling. Firstly, it can slightly increase the Nusselt number on impinged surface. Secondly, due to the jet flow confinement inside the curvature, the Nusselt number distribution decreased. In their study, infrared thermography camera (IR) measured temperature. In a similar experimental study, Lee et al. [43] assessed the effect of surface curvature (d_j/D_{ch}) on heat transfer, portraying Nusselt number distribution increased as curvature increased.

In 1990, Bunker et al. [11] experimentally studied impingement cooling on the leading edge in the absence of film coolant extraction. For the experimental setup, a single row of multiple jets is used, and the temperature indicating coatings method is adopted for the temperature measurements. The effect of different factors such as jet Reynolds number, leading-edge curvature, the jet-to-target surface distance are selected for heat transfer evaluation. Results indicated decreased leading-edge sharpness (leading-edge curvature radius) and jet-to-target surface spacing, enhancing heat transfer efficiency. Also, they noted as the jet Reynolds number increased, heat transfer on the surface also increased. They also professed reducing jet to jet distance for heat transfer enhancement. In 2006, Taslim et al. [23] experimentally and numerically evaluated the effect of film holes extraction on internal impingement heat transfer. The Reynolds number they employed varied from 8,000 to 48,000. They found out that heat transfer on the target plate significantly increased in the presence of extraction film holes. Also, experimental and numerical results agreed for the case where extraction film holes are absent. Nevertheless, in the case of having film holes, the average difference between numerical and experimental investigation is calculated

to be around 30%. In 2001, Taslim et al. [44] experimentally explored the effect of target wall roughness on impingement heat transfer coefficient. They used curved and roughened target surfaces with four roughness shapes: smooth wall, a high surface roughness wall, a conical bump, and a radial rib. The turbulent Reynolds number up to 40,000 is used in their calculation. They noted rough surfaces strongly enhanced heat transfer. Also, conical bumps have higher heat transfer compared to the other roughened surfaces, leading to an increased heat transfer of up to 40%. In an other study, Taslim et al. [22] further investigated numerically and experimentally the effect of different surface roughness, like a horseshoe and notched-horseshoe roughness on impingement cooling gas turbine blade leading edge. For comparison, they took some experimental data from their previous study [44]. Finally, they determined overall heat transfer enhancement with roughened surfaces where heat transfer increased to 27%. They also showed the maximum heat transfer impingement occurred with a smooth wall. Also, good agreement is found between their CFD and experimental investigation reported in [22]. Taslim et al. established that as jet Reynolds number increased, jets' heat transfer coefficient also increased [22, 23, 44]. Martin and Wright [45] experimentally investigated the impact of jet temperature on the blade leading edge. The cylindrical shape is chosen for their experimental study. A single row of multiple jets is employed to evaluate the thermal behavior on the target surface where the jet Reynolds number is varied from 5,000 to 20,000, jet to jet spacing distance (s/d_j) is varied from two to eight, jet to target distance (l/d_j) is varied from two to eight, and the target curvature diameter to jet diameter (D/d_j) is ranged from 3.6 to 5.5. As they mentioned, higher the Reynolds number, the higher the Nusselt number on the target surface.

Reduction in the jet-to-target distance and jet-to-jet spacing enhanced heat transfer. However, for (l/d_j) and (s/d_j) above 4, the heat transfer efficiency decreased. The results are compared with the Chupp et al. [38] correlation and the difference between the two is less than 15 %. Also, some modification has been done on the correlation for higher Reynolds number. They also noted minor enhancement in the average Nusselt number as the diameter of the leading-edge increased. Metzger et al. [46] studied how the numbers of jet holes affected thermal efficiency. They reported multiple jets performed differently compared to the single impingement jet. The Reynolds number significantly influenced Nusselt number performance, while the effect of jet-to-target spacing is not prominent. Florschuetz et al. [47] reported that in the case of strong crossflow, and large jet-to-target spacing, jets get deflected by the cross flow easily.

Moreover, crossflow changes jet direction, shifts and deflects the impingement away from the target surface. Kumar and Han [48] experimentally assessed impingement heat transfer in two rectangular pass channels with rotation. Two rows of multiple jets are used in their study, where the direction of jets opposed each other (one row in the same direction as rotation and the second-row opposite to the rotating direction). Turbulent jet Reynolds number varied from 4000 to 10,000, and the jet rotation number (Ro_j) ranged from 0 to 0.0133, where the maximum rotation of the test section reached 800 rpm. For the target plate, two surfaces (smooth and ribbed walls) are used. The study concluded the following: firstly, rotation negatively affected heat transfer due to the centrifugal and Coriolis force, and jets are deflected away from the target plate. Secondly, for the stationary condition, when increasing the jet Reynolds number from 4,000 to 10,000, the ratio of ribbed to smooth wall Nusselt

number rose from 13% to 47%. It is related to the flow separation, reattachment, and secondary flow created by impinging jets over ribs. This ratio is less for the rotating condition than the stationary situation due to the centrifugal and Coriolis force that can reduce the impingement over ribs. The heat transfer coefficient is reduced up to 20% for the rotating ribbed wall. Also, the ratio of average Nusselt number of the rotation to non-rotating condition decreased as rpm increased. They also developed two correlations for the average Nusselt number for the first and second impingement channels.

Sunk Kook Hong et al. [49] experimentally investigated rotation and jet impingement thermal evaluation. Jet Rotation number ($Ro_j = 0.075$) and the jet Reynolds number ($Re_j = 5000$) are considered fixed in their experimental study. Two jet-to-target distance (l/d_j) with the value of two and six are employed in their investigation. Naphthalene sublimation is used for temperature measurements. They observed that the rotation strongly affects jet deflection inside the cavity for ($l/d_j = 6$), decreasing heat transfer. For ($l/d_j = 2$), the rotation minorly influenced heat transfer proficiency on the target surface. In 2012, Hongwu et al. [50] experimentally explored how the Reynolds number and the jet angle impacted heat transfer on leading-edge with film cooling extraction under rotating conditions. The angles between the rotating axis and injection holes equaled 0° , 30° , and 45° . The jet Reynolds number ranged from 2000 to 12,000, and the rotation number varied from 0 to 0.278. Also, jet-to-target surface spacing ($l/d_j = 2$) remained fixed. TLC is adopted for the temperature measurements.

The following conclusions are obtained from the experimental study. Film cooling holes change the flow behavior inside the cavity, enhancing heat transfer. The higher

the jet Reynolds number, the higher the heat transfer rate. They concluded rotation is negatively affected heat transfer. Different tests are performed for $Re_j = 4000$ and $Ro = 0.139$ at three angles. The results indicated Nusselt number values at the stagnation point fell by 33%, 30%, and 35%, and the average Nusselt number on the target surface decreased by 33%, 35%, and 36%, respectively. The heat transfer reduction on the suction side (10%) and the pressure side (20%) differed, where $Re_j = 4000$ and $Ro_j = 0.139$.

Elston et al. [51] empirically examined rotation on the leading edge, using a single row of multiple jets. Their experimental facility is taken from Wright and Elston with some test section modifications [52]. Some parameters, like jet-to-jet spacing ($s/d_j = 4$), jet-to-target surface spacing ($l/d_j = 3.2$) and target wall curvature to jet diameter ($D/d_j = 6.4$) remained fixed. Thin heating plates are implemented into the leading-edge channel to heat the surface, and T-type thermocouples are used for the temperature measurements. The maximum rotational speed of 500 rpm is used where rotation number (Ro) reached 1.4 and the Buoyancy number varied from 0 to 6.6 near the channel inlet. Also, the jet Reynolds number varied from 6,000 to 24,000. The following findings emerged from their experimental study: The variation of Nusselt number distribution observed in all rotating cases compared to the stationary conditions. The rotation positively impacted heat removal for a pure jet impingement (first jet, without the crossflow) due to the mixing with the secondary flow. Finally, for the remaining jets, chiefly for those with stronger crossflow, the rotational effect remained negligible, and rotation did not strongly affect the Nusselt number distribution.

Burberi and Massini et al. [34, 53] experimentally and numerically investigated the effect of rotation on jet impingement heat transfer of gas turbine blade leading edge. The jet Reynolds number varied from 10,000 to 40,000, and the jet rotation number (Ro_j) varied from 0 to 0.05. Four rows of showerhead holes and film cooling extraction are implemented into the leading edge for numerical and experimental investigations. In the experimental setup, constant heat flux is applied on the leading-edge using an Inconel alloy sheet with 25.4 μm thickness. Steady TLCs are employed for the temperature measurements in their experimental study, revealing strong crossflow can easily deflect the jets away from the target surface, resulting in jet Nusselt number variation on the target surface. The average value of jet Nusselt number is not altered during rotation, but the heat transfer shifted to the suction side. They also displayed rotation remained minimal at the hub for a pure jet (without crossflow), contrasting with Elston et al. study [51]. Elston et al. showed rotation positively affected heat transfer efficiency for a pure jet impingement due to the mixing with the secondary rotational flow. These diverging results can be due to the existing extraction film holes in Berburi et al. experimental design. They demonstrated good agreement between numerical and experimental investigations, validating their numerical results.

Chapter 3: Numerical Formulation

Computational Fluid Dynamics (CFD) engenders a numerical methodology for simulating fluid flow. It enables the professionals and analysts to foresee qualities of a framework, including flow velocity, pressure, temperature, and heat transfer characteristics. Numerical analysis in this work employed Fluent ANSYS Workbench of version 15.0. CFD analysis consisting of multiple stages: initial, a pre-processing application using CFD geometry establishing the model geometry. Boundaries such as walls, inlets, and outlets are also defined in this phase. When the geometry and the boundary conditions for the problem are completed, the computational domain defining the problem is divided using CFD meshing application into quadrilateral or triangular cells in 2D; or hexagonal or tetrahedral cells in 3D, forming a mesh or grid. This mesh is then imported to FLUENT, generating the flow field solutions at mesh points. Notably, proper boundary conditions are applied in the computational domain. The CFD Solver FLUENT creates the stream field information at each mesh point after solving the appropriate governing equations. After FLUENT creates the flow field, it sends it to an information processor (CFD-Post) to produce line plots, plots, and flow variable contours. Likewise, this information can be sent to other applications, such as Excel, to permit correlations with estimations and information directly. A 3D steady-state turbulent flow of circular jet impingement on a gas turbine blade's curved surface is considered in this section. The effect of rotation and the jet Reynolds Number on the leading edge's cooling performance is also examined.

3.1 Governing Equations

The governing equations of turbulent flow entail partial differential equations, including continuity, momentum, energy, and turbulence model equations. This section will briefly describe the continuity equation, momentum equation, energy equation, and turbulence model equations. In Cartesian format, the following equations are realized.

3.1.1 Continuity Equation

The following equation is the general form of conservation of mass used for simulating incompressible flows [6].

$$\frac{\partial}{\partial x_j}(U_j) = 0 \quad (3)$$

3.1.2 Momentum Equation (Navier-Stokes Equations)

The momentum equations are derived by applying Newton's second law of motion to the fluid's differential volume. According to Newton's second law, the momentum change rate over a differential volume of fluid equals the sum of all external forces acting on this fluid volume. The resulting momentum equations in Cartesian coordinates take the general form [6]:

$$\rho \frac{\partial}{\partial t}(U_i) + \rho \frac{\partial}{\partial x_j}(U_j U_i) = -\frac{\partial P}{\partial x_i} + \frac{\partial}{\partial x_j} \left(\mu_{eff} \left(\frac{\partial U_i}{\partial x_j} + \frac{\partial U_j}{\partial x_i} \right) \right) \quad (4)$$

3.1.3 Energy Equation

The energy equation, derived from the first law of thermodynamics, denotes the fluid particle's energy rate equals the sum of heat exchange and the work exchange rate associated with the particle. The resulting energy equation in the general form [6]:

$$\rho \frac{\partial}{\partial t} (h_{tot}) - \frac{\partial p}{\partial t} + \rho \frac{\partial}{\partial x_j} (U h_{tot}) = \frac{\partial}{\partial x_j} \left(\lambda \frac{\partial \tau}{\partial x_j} + \left(\frac{\mu_t}{Pr_t} \right) \frac{\partial h}{\partial x_i} \right) + \nabla \cdot (U \cdot \tau) + S_E \quad (5)$$

3.2 Turbulence Modeling

Various models of numerical calculation detail fluid flow and heat transfer: Reynolds Average Navier Stokes (RANS), large eddy simulation (LED), and direct numerical simulation (DSN). Among these models, Reynolds Average Navier Stokes equations (RANS) are commonly used for the problems.

3.2.1 Turbulence Modeling Introduction

Reynolds Average Navier Stokes (RANS) turbulence model consists of one or two equations, where the model can be selected based on the problem complexity and domains. These models include:

- Spalart-Allmaras— one turbulent equation model used primarily for two-dimensional problems.
- Standard $k-\varepsilon$ — suitable for modeling flow far from the wall.
- RNG $k-\varepsilon$ – Suitable for complex shear flows problems.
- Realizable $k-\varepsilon$ — Similar to RNG $k-\varepsilon$ but more accurate and has better convergence than RNG.
- Standard $k-\omega$ — Suitable for complex boundary layer flows.

- SST $k-\omega$ — Combination of $k-\omega$ and $k-\varepsilon$. Suitable for boundary wall and far from the wall.

After reviewing the literature, the proper turbulence model for jet impingement problem is determined to be SST $k-\omega$, given the model can predict flow behavior near the boundaries and far from the wall with an acceptable error. The turbulent model $k-\omega$ predicts turbulence using two partial differential equations for k and ω variables, standing for turbulence kinetic energy and the specific rate of dissipation [54].

3.2.2 SST $k-\omega$ Model

The shear stress transport (SST) $k-\omega$ turbulence model contains some near-wall enhancement for Wilcox's $k-\omega$ model. A combination of the Wilcox $k-\omega$ turbulent model and $k-\varepsilon$ model known as SST $k-\omega$ model is adopted for the simulation. It combines the flow behavior near the boundary by standard $k-\omega$ model and the $k-\varepsilon$ model to simulate free streamflow. Menter [55] created the SST $k-\omega$ model to combine the exact and robust definition of the $k-\omega$ technique in the near-wall region with the free-stream independence of the $k-\varepsilon$ model in the far-field. The $k-\varepsilon$ model is transformed into a $k-\omega$ formulation to accomplish this. Compared to the standard $k-\omega$ formulation, the SST $k-\omega$ model contains the following refinements:

- The standard $k-\omega$ and the converted $k-\varepsilon$ models are multiplied by a blending function, and the two models are included. The blending function is planned to be one in the near-wall region, switching on the standard $k-\omega$ model and zero away from the surface, enacting the changed k -model.
- The turbulent viscosity definition is improved to simulate the transport of the turbulent shear stress. Based on these features, the SST $k-\omega$ model becomes more

accurate and valid for more classes of flows (adverse pressure gradient flows, airfoils, and transonic shock waves) than the standard k - ω model.

The SST k - ω equations composed as follows:

k -Equation:

$$\frac{\partial (\rho k)}{\partial t} + \frac{\partial}{\partial x_j} (\rho U_j k) = \frac{\partial}{\partial x_j} \left[\left(\mu + \frac{\mu_t}{\sigma_{k3}} \right) \frac{\partial k}{\partial x_j} \right] + P_k - \beta' \rho k \omega + P_{kb} \quad (6)$$

ω -Equation:

$$\begin{aligned} \frac{\partial (\rho \omega)}{\partial t} + \frac{\partial}{\partial x_j} (\rho U_j \omega) \\ = \frac{\partial}{\partial x_j} \left[\left(\mu + \frac{\mu_t}{\sigma_{\omega 3}} \right) \frac{\partial \omega}{\partial x_j} \right] + (1 - F_1) 2\rho \frac{1}{\sigma_{\omega 2} \omega} \left(\frac{\partial k}{\partial x_j} \right) \left(\frac{\partial \omega}{\partial x_j} \right) \\ + \alpha_3 \frac{\omega}{k} P_k - \beta_3 \rho \omega^2 + P_{\omega b} \end{aligned} \quad (7)$$

The reported set of equations are presented in a general form for compressible flow, meanwhile, for the case we are studying the flow is incompressible where the density is constant, and the Mach number is a way below 0.3.

The Buoyancy turbulent term for the ω -equation:

$$P_{\omega b} = \frac{\omega}{k} ((\alpha + 1) C_{3 \max}(P_{kb}, 0) - P_{kb}) \quad (8)$$

The coefficients of the new model consist of a linear combination of the relating coefficients of the basic models:

$$\Phi_3 = F_1 \Phi_1 + (1 - F_1) \Phi_2 \quad (9)$$

The rest of the coefficients are shown as follows:

$$\beta' = 0.09$$

$$a_1 = 5/9$$

$$\beta_1 = 0.075$$

$$\sigma_{k1} = 2$$

$$\sigma_{\omega 1} = 2$$

$$\alpha_2 = 0.44$$

$$\beta_2 = 0.0828$$

$$\sigma_{k2} = 1$$

$$\sigma_{\omega 2} = \frac{1}{0.856}$$

The k - ω based SST model computes the transport of the turbulent shear stress and provides exceptionally accurate predictions of the starting and amount of flow separation under an adverse pressure gradient. In the SST k - ω model, the eddy viscosity does not remain constant for finding the transport of the turbulent shear stress. Therefore, the behavior of transport can be treated by a limiter to the formulation of the eddy viscosity:

$$v_t = \frac{a_1 k}{\max(a_1 \omega, SF_2)} \quad (10)$$

where

$$v_t = \frac{\mu_t}{\rho} \quad (11)$$

$$F_1 = \tanh \left(\min \left(\max \left(\frac{\sqrt{k}}{\beta' \omega y}, \frac{500}{y^2 \omega} \right), \frac{4 \rho k}{CD_{kw} \sigma_{\omega 2} y^2} \right)^4 \right) \quad (12)$$

$$F_2 = \tanh \left(\max \left(\frac{2 \sqrt{k}}{\beta' \omega y}, \frac{500 \nu}{y^2 \omega} \right)^2 \right) \quad (13)$$

where

$$CD_{kw} = \max \left[2\rho \frac{1}{\sigma_{\omega 2} \omega} \frac{\partial k}{\partial x_j}, 1.0 \times 10^{-10} \right] \quad (14)$$

y^+ – the distance to the nearest wall.

ν – kinematic viscosity, (m^2/s).

F_2 – blending function similar to F_1 , restricting the limiter to the wall boundary layer.

S – Invariant measure of the strain rate, ($1/s$).

3.3 Description of Physical Model

This section describes the geometry and the dimensions of the leading edge used to create the physical geometry under investigation. Figure 10 shows the computational domain created using the ANSYS geometry package. A zero wall thickness is adopted for the model. The geometry consisted of a supply rectangular cross-section channel. Through the channel, coolant air is provided to the seven jets. The jets are impinging on the semicircular cavity's target surface, representing the leading edge. Markedly, the inlet supply channel and the outlet sections of the semicircular cavity are extended (elongated) to guarantee a uniform flow to and out of the geometry.

The extension in the supply channel inlet section ensures a uniform supply flow to the seven jets. Also, it helps with better convergence of the numerical analysis. A uniform regulated cooling air cooling enters from the bottom side of the supply channel, supplying the seven circular jets, entering the semicircular cavity, impinging on the target surface and discharging from the top to the surrounding, as the cavity is blocked from the bottom. Therefore, the only path available for the cooling to exit the leading edge is the top opening. The closest jet to the inlet flow is addressed as jet number one, and the jet closest to the outlet side is addressed to as jet number seven.

For the simulation cases used to validate the experiment runs, a simple modification is applied to the simulation geometry, so the inlet supply channel matches the real experiment case. The cooling air supply hose is connected to the square cross-section channel in the experiment setup using an adapter with a 10 mm diameter. Therefore, the cooling air expands from a 1 cm adapter diameter to a square cross-section channel of 30 mm by 30 mm. This modification is applied for the validation of CFD cases. Both designs are shown in Figure 10. Other dimensions and details are presented in Figure 11.

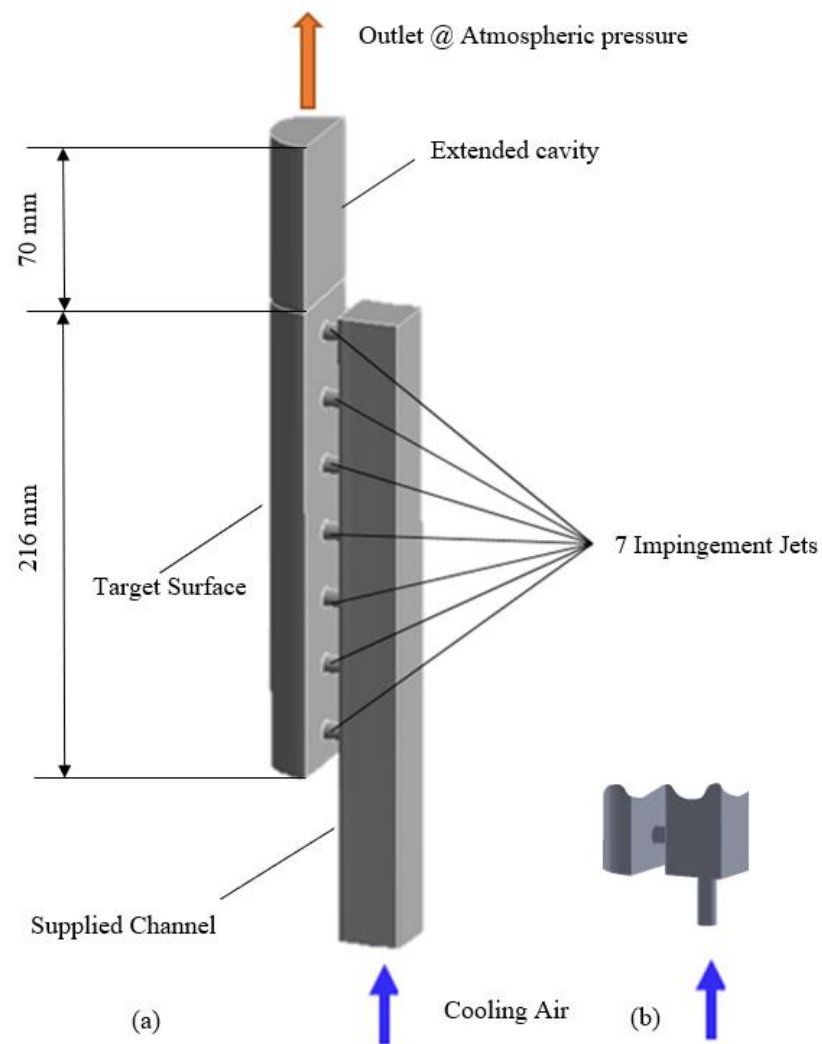


Figure 10: Semicircular leading edge with rectangular supplied channel, (a) rectangular inlet supplied channel, (b) adapter connected to rectangular supplied channel used in the experiment for a CFD validation

3.3.1 Assumptions

- The flow is incompressible and all thermo-physical properties are consider constant.
- The viscous heat dissipation in the energy equation is neglected since calculated Brinkman number (Br) is very small.
- The inlet channel flow velocity and temperature are uniform.

- The semi-circle leading edge surface is exposed to uniform constant heat flux (1000 W/m^2).

The diameter of the curved semicircular surface is $D_c = 50 \text{ mm}$. The distance from the center of the leading edge to the rotating x-axis is $R_{arm} = 50 \text{ cm}$. Other dimensions are listed in Table 1:

Table 1: Dimensions and geometric model details

Parameter	Value
jet diameter (d_j)	8 mm
jet to jet distance (s/d_j)	4
jet to target distance (l/d_j)	25
jet thickness (t/d_j)	1.5
curved diameter (D_c)	50 mm
Arm radius (R_{arm})	500 mm
Leading Edge Length (L_{LE})	216 mm
Supplied channel width (w)	30 mm
Channel Hydraulic Diameter (D_H)	30 mm
Number of Jets (n)	7
1st jet distance from the bottom	12 mm
7th jet distance from upper side	12 mm

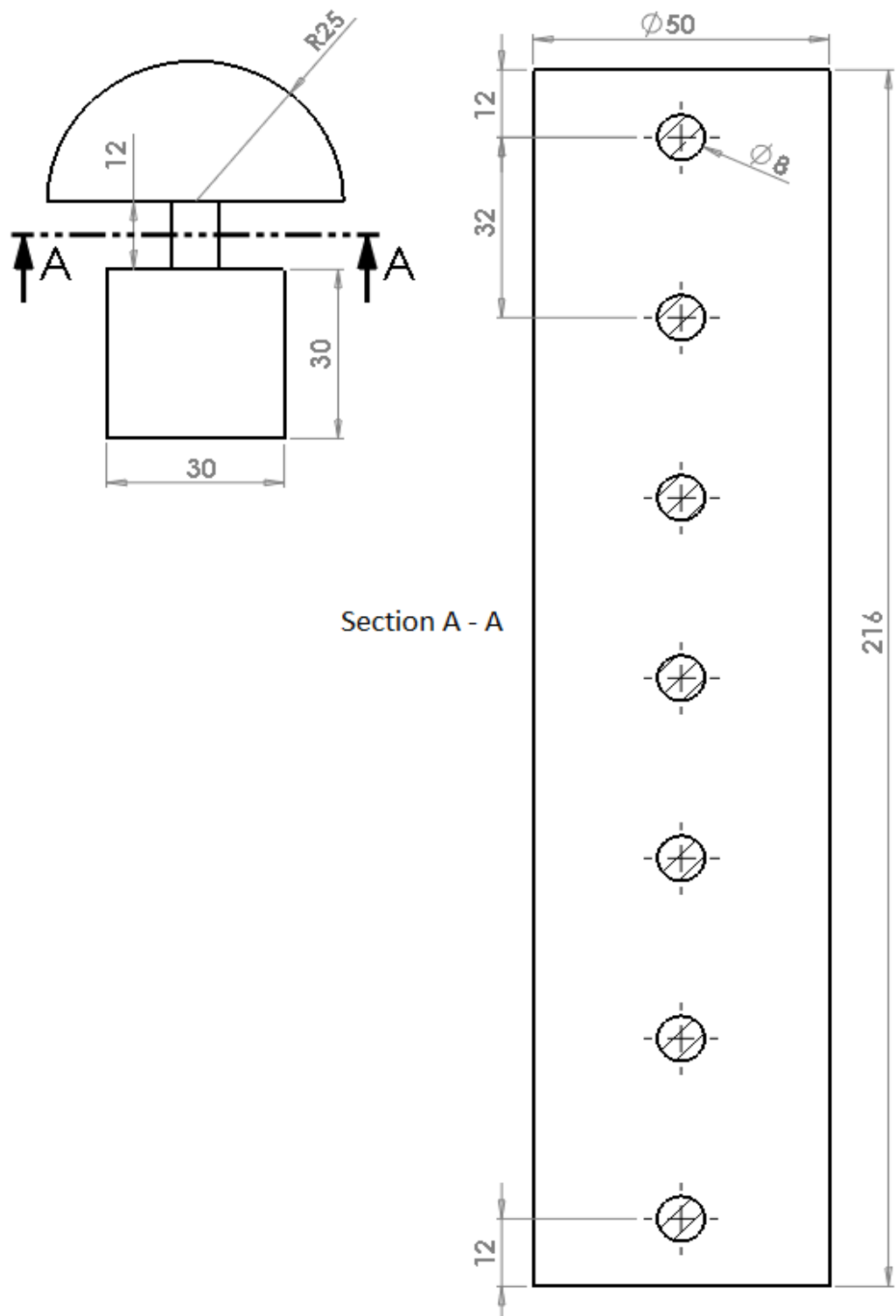


Figure 11: Geometry and dimensions of the leading edge (Dimensions are in mm)

3.4 Meshing

3.4.1 Mesh Description

Tetrahedron elements are used for all cases with a patch conforming algorithm to create a proper mesh. As shown in Figure 12, boundary layer mesh is used for walls, especially for the target surface, to meet the requirement for SST $k-\omega$ turbulence model. Based on the requirement for SST turbulent model, y^+ is maintained around ~ 1 for all cases, and the growth rate is kept 1.2 from the wall by default. Figure 12 shows the cross-section of the final mesh used in numerical calculation.

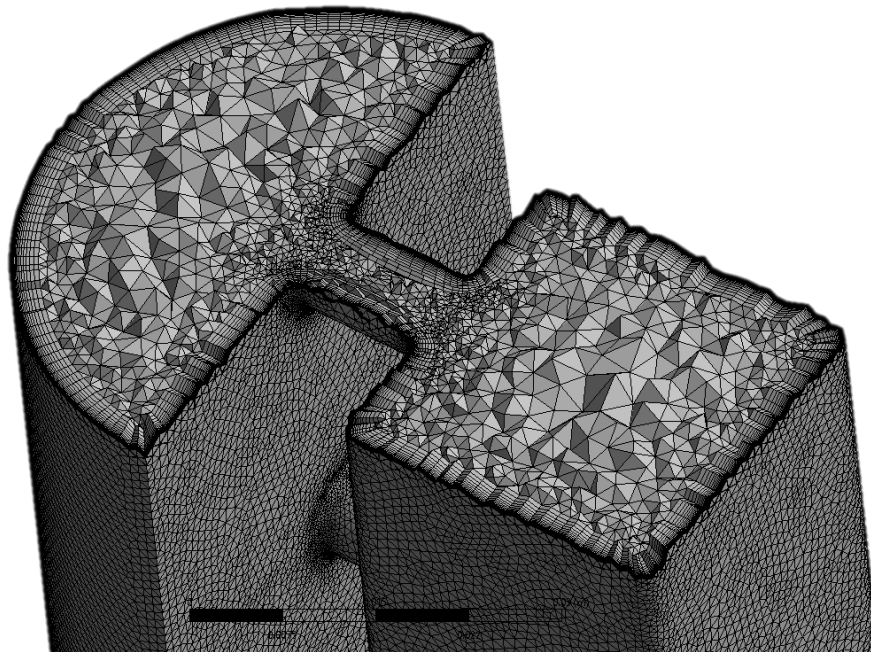


Figure 12: Model with tetrahedrons mesh with 8 million elements

3.4.2 Wall Treatment Method

Usually, the adjacent wall affects the turbulence flow, where typically, wall produces a shearing effect on the flow. The boundary layer results from passing fluid

along the wall. Therefore, the velocity gradient varies from zero at the wall to the free stream value far from the wall.

These specifications are required to get y^+ less than the unity for $k-\omega$ SST turbulent model. Therefore first layer thickness is calculated based on the desired y^+ as follows:

$$y^+ = \frac{\rho \cdot U_\tau \cdot \Delta y_1}{\mu} \rightarrow \Delta y_1 = \frac{\mu \cdot y^+}{\rho \cdot U_\tau} \quad (15)$$

Δy_1 – first layer thickness, mm

ρ – density, kg/m³

μ - dynamic viscosity, Pa.s

U_τ – frictional velocity, m/s

y^+ - Non dimensionless parameter

$$U_\tau = \sqrt{\frac{\tau_w}{\rho}} \quad (16)$$

τ_w – wall shear stress, N/m²

$$\tau_w = \frac{1}{2} \cdot C_f \cdot \rho \cdot U^2 \quad (17)$$

U – free stream velocity, m/s

C_f – empirical estimate ($C_f = 0.079 \cdot Re^{-0.25}$ for internal flows)

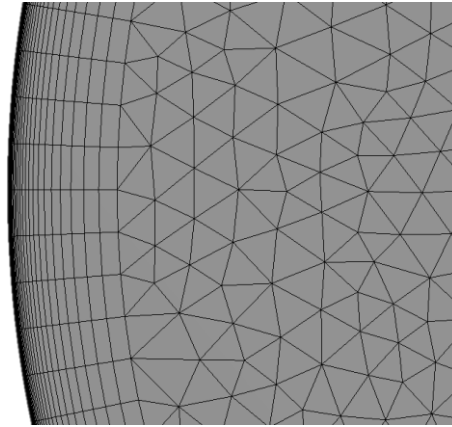


Figure 13: Boundary layer mesh on the target surface

3.4.3 Grid Independent Study

The mesh independent study employed five element sizes for $Re_j = 5,000$ and $Re_j = 30,000$. For each case, the average Nusselt number on the target surface is adopted for comparison. The results of the mesh study are shown in Table 2.

$$Error\% = \frac{|Nu_{n-elem} - Nu_{8mil}|}{Nu_{8mil}} * 100\%$$

Table 2: Average Nusselt number for each case

$Re_j = 30,000$			
Case	Number of Elements	Nu-Avg	Error, %
1	778,619	84.1	7.54
2	1,180,841	80.0	2.30
3	1,685,419	78.3	0.13
4	3,886,351	77.6	0.77
5	8,017,527	78.2	0.00
$Re_j = 5,000$			
Case	Number of Elements	Nu-Avg	Error, %
1	500,000	56.1	7.7
2	904,000	53.3	2.3
3	1,900,182	52.2	0.2
4	3,886,351	51.7	0.8
5	8,017,527	52.1	0.0

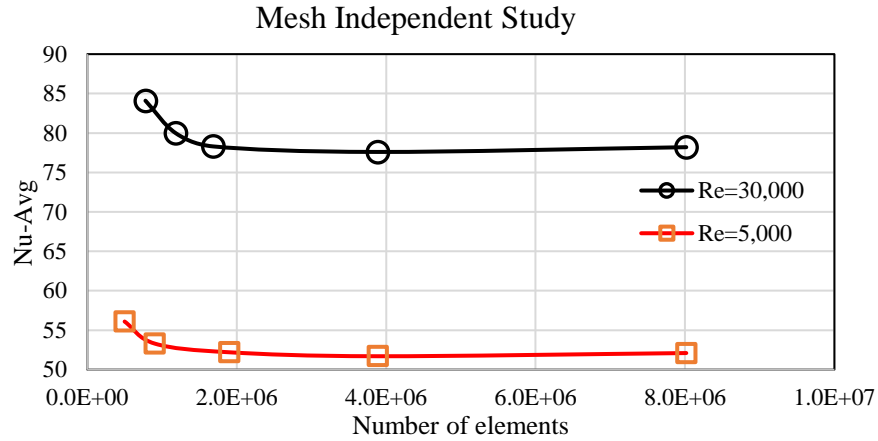


Figure 14: Grid independent study for $Re_j = 5,000$ and $Re_j = 30,000$

3.5 CFD Solution

3.5.1 Discretization Scheme

Several discretization schemes are available. Initially, every model is run with the first-order upwind scheme, and the subsequent is changed to the second-order upwind scheme. Hence, it flows unidirectionally in most domains. So, experts have recommended using second-order schemes for strong convection. The second-order upwind scheme fulfills the property of transportiveness and is more accurate than the first-order one. A significant drawback of this scheme is its unboundedness.

3.5.2 Boundary Conditions

Cooling air enters the rectangular channel at 35°C with an inlet velocity corresponding to the required jet Reynolds numbers, varying from 7,500 to 30,000. Consequently, the airflow moving to the supply channel passes through seven circular jets and impinging on the curved surface. The semicircular cavity target surface is exposed to a constant heat flux of 1000 W/m². The accumulated impingement jets move in the

z-axis to leave the cavity from the top open to the surrounding. Also, the model rotates around the x-axis from 0 to 750 rpm. The cooling air properties are shown in Table 3.

Table 3: Properties of cooling air

Parameter	Value
Inlet Cooling Temperature, T_{inlet} (K)	308
Thermal conductivity, k (W/m.K)	0.02625
Dynamic viscosity, μ (kg/m.s)	1.895 e-5
Density, ρ (kg/m ³)	1.145

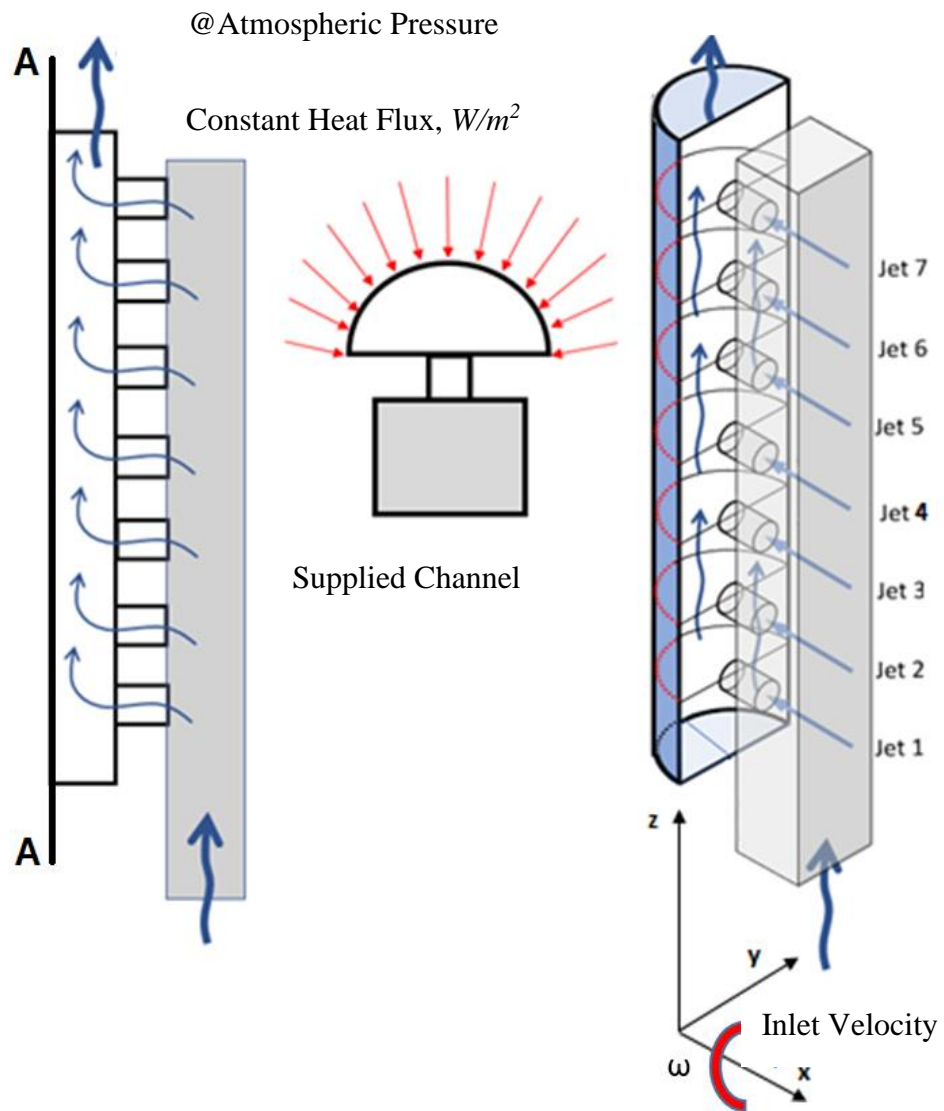


Figure 15: Model description

Table 4: Domain and boundary conditions of the modeled leading edge

Parameters	Value
Cooling air temperature, K	308
Constant Heat flux, (W/m^2)	600
Jet Reynolds number	7,500 – 30,000
Outlet pressure, Pa	0
Rotation, rpm	0 – 750

3.5.3 Solver Setting

The choice of solver settings in FLUENT is based on existing literature and guidelines of the near-wall 3D turbulence model. The following solver settings are used in all the cases in this thesis:

- Double precision, segregated steady solver.
- Standard method for pressure.
- Second-order upwind discretization for momentum and energy equations, the first order for turbulent kinetic energy.
- Under-relaxation factors for pressure, density, body forces, momentum, turbulent kinetic energy, turbulent dissipation rate, turbulent viscosity, and energy are equal to 0.3, 1, 1, 0.2, 0.8, 0.8, 1, and 0.9, respectively.
- SIMPLE algorithm with pressure-velocity coupling.
- SST $k-\omega$ turbulence model.

3.5.4 Measure of Convergence

For all the CFD runs, using the same geometry, the same mesh, different Reynolds numbers, and different rotational numbers, an average estimated time for the simulation convergence was about 15 hours per case, using a high-performance computer with 24 processors. The numerical solution convergence was achieved when the temperature residual reaches less than 10^{-7} and the velocities and continuity residuals reach less than 10^{-5} , as shown in Table 5. By monitoring average nusselt number, Figure 16, one can realize that average Nusselt number reaches convergence earlier than the parameters shown in Table 5.

Table 5: Conversions residuals

Parameter	Residual
x-velocity	1×10^{-5}
y-velocity	1×10^{-5}
z-velocity	1×10^{-5}
Continuity	1×10^{-5}
Specific dissipation energy/ dissipation	1×10^{-5}
Turbulent kinetic energy	1×10^{-5}
Energy	1×10^{-7}

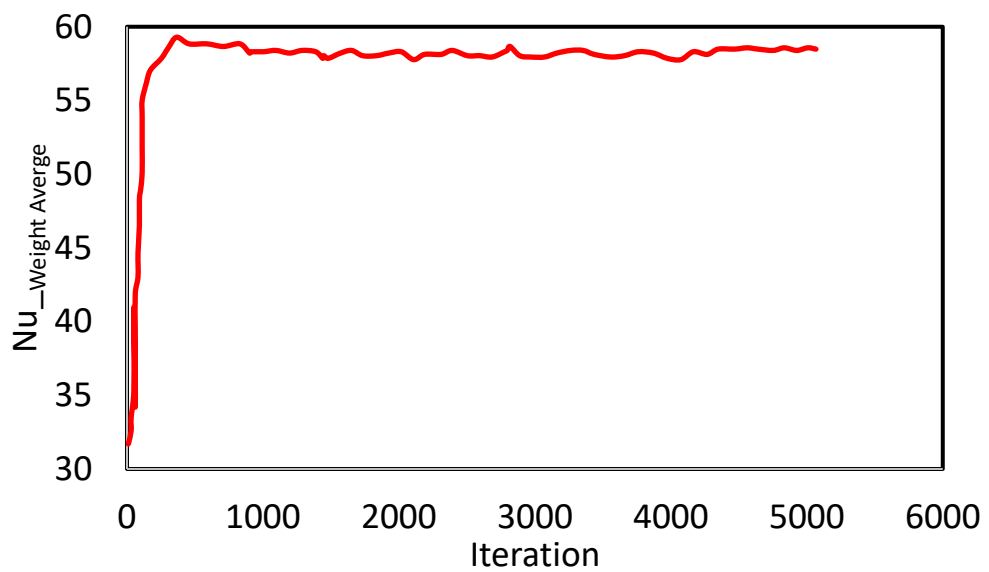


Figure 16: Monitoring average Nusselt number on the target surface

Chapter 4: Experimental Setup and Details

4.1 Overview of Experimental Setup

The current experimental study aims to design and build a setup that simulates the jet impingement cooling of the rotating gas turbine leading edge. The experimental results will help validate the reported numerical data. A steady-state air coolant will be supplied from a 950 Liter storage tank compressed to 10 Bar into the setup's test section. The target surface is heated with a flexible heater with constant heat flux, simulating the hot gas flow. The experiments used a jet Reynolds number of 7,500 for the rotating condition of 0, 50, 100, 150, and 200 rpm. TLC provided the temperature mapping, and an array of localized thermocouples distributed over the target surface are employed. Seven T-type thermocouples are located in front of each impingement jets. One thermocouple is located at the inlet of the supply channel and one at the chamber's exit.

4.2 Test Facility

Most of the parts used in the setup are custom made and ordered from different suppliers. The setup is designed at UAEU and manufactured at Industrial Area in Al Ain city and took around two years to build up and run due to the experiment's complexity and sensitivity. The leading edge is designed to be flexible and easy to change, allowing other cooling techniques by changing the high density polyethylene (HDPE) material's inner part. The system can also study any rotating model in other fields rather than thermal, such as assessing flow behavior.

The current experimental setup is similar to Elston et al. [51]. In their study, the temperature measurements are performed by employing an array of thermocouples. The pressure inside the test section is regulated to the specific value by adding one more rotary union at the cooling air exit. In the current study, the thermocouples and TLC technique are combined for the temperature measurements. Also, the leading-edge outlet is open to the atmospheric pressure. In this design, the upper jets are exposed to a higher crossflow similar to the actual turbine blade. Nevertheless, in their study, the pressure inside the chamber remained more close to the actual one. The best scenario is to control the chamber pressure and regulate the coolant exit from the top of the leading edge. The combined design is practical but brings some complexity to the leading edge.

4.2.1 Test Rig Description

Figure 17 portrays the overall experimental setup, consisting of an air compressor connected to three storage tanks with an overall capacity of 950 Liter. A pressure regulator controlling the outlet air pressure from the storage tank and a needle valve to regulate the flow rate is employed. A Tokyo-Keiso thermal flow meter type (TF-4000) is used for measuring the coolant flow rate. A rotary union manufactured by Deublin USA allowed the coolant air stream to be transferred between the rotating and static components. A slip ring manufactured by MOFLON— China is used to transfer the powering signals from the power supply to the heater and send the thermocouple signals from the test section to the data logger. Four ball bearings balanced the rotating part, a PVC hose inside the rotating pipe to prevent leakage and flow disturbance. A high-speed camera model (Guppy Pro F-125) made in the USA with 32 FPS captured the images of the leading-edge surface liquid crystal temperature

mapping during rotation. The camera base contained an adjustable arm to position the camera. The camera's lighting is arranged using four LED lights (YN 600 L), fixed around the camera without any reflection from the curved acrylic surface. A homemade helical heat exchanger is designed for heating the cooling air to the required temperature.

A data logger model (Delta OHM HD-32.8) made in Italy is employed for acquiring and storing the temperature data, as well as transferring it to the PC. Surface thermocouples type-T made by Omega measured the local jet temperature on the target surface and the inlet and cooling air outlet. A 3-phase frequency converter with 5.5 kW made by Omran-Japan controlled the AC motor rotation. A counterweight balance the leading-edge rotating arm. A tachometer made in Germany model TACH-20 measured the rpm. Finally, a DC power supply model 305F made in China drove the flexible heater. All setup components are listed in Table 6.

Below described all the experimental parts:

1. Leading edge, 2. Slip ring, 3. Bearing, 4. Cross joint, 5. Rotating arm, 6. Counter weight, 7. Pulley, 8. Electric motor, 9. Rotary union, 10. Camera, 11. Adjustable camera holder, 12. Setup housing, 13. Belt, 14. Air compressor 15. Moisture separator and Pressure regulator, 16. Heat exchanger, 17. Needle valve, 18. Digital flow meter, 19. Inlet adapter, 20. Target surface, 21. Desktop computer, 22. Data logger, 23. DC power supply, 24. Frequency controller, 25. Tachometer.

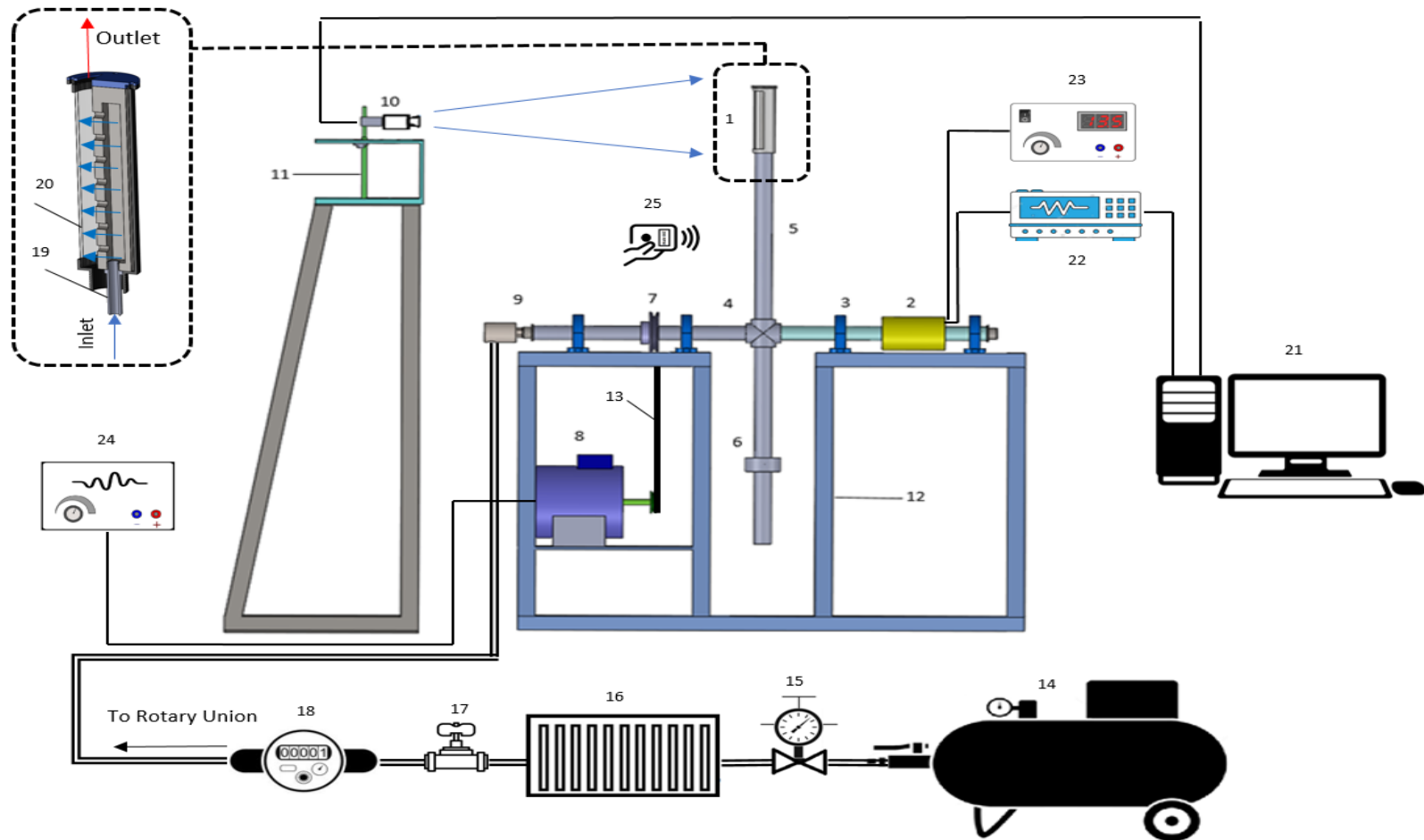


Figure 17: Experimental setup overview



Figure 18: Actual experimental setup

Table 6: Setup components

No	Item	Model / Part number	Manufacturer	QTY
1	Slip Ring	Custom made	MOFLON - China	1
2	Rotary Union	Custom made	Deublin - USA	1
3	Flexible Heater	Custom made	EVOLC – China	1
4	Liquid Crystal Sheet	R30C5W	Hallcrest - UK	1
5	Data Logger	Delta OHM HD-32.8	Italy	1
6	DC Power Supply	305 F	China	1
7	Tachometer	TACH 20	Germany	1
8	Infrared Camera	E320	FLIR - US	1
9	Digital Multimeter	Omegaette	Omega - USA	1
10	Frequency Controller	3 Phase – 5.5 kW	Omron - Japan	1
11	LED Light	YN 600 L	China	3
12	Thermal Flow Meter	TF-4000	Tokyo Keiso - Japan	1
13	High-Speed Camera	Guppy Pro F-125	USA	1
14	Electric Motor	3 HP	Prakash – India	1
15	Thermocouples	T-type	Omega - USA	10
16	Isolator ON/OFF Switch	20 AMP	Schneider - France	2
17	Compressor	3 HP – 270 L	ABAC – Italy	1
18	Extra Tanks	Custom made	UAEU	2
19	Needle Valve	30000315	Toolz – Nigeria	1
20	Pressure Regulator	SNS – SY8M05	China	1
21	Heat Exchanger	Custom made	UAEU	1
22	Stainless Steel Pipe	304 L	Technos - Dubai	-
23	Cross Joint Stainless Steel	Custom made	Al Ain – Inds. Area	1
24	Bearing	P 211	Asahi - Japan	4
25	Filler	HDPE	India	-
26	Setup Housing	Custom made	Al Ain – Inds. Area	1
27	Adjustable Camera Base	Custom made	Al Ain – Inds. Area	1
28	Caster Wheel	-	-	4
29	Acrylic Tube	55 mm Diameter	Sign trade – Al Ain	-
30	Belt & Pulley	-	-	1
31	Counter Weight	Custom made	Al Ain – Inds. Area	1
32	Hose and Adapters	-	Technos – Dubai	-
33	Desktop Computer	-	UAEU	2

4.2.2 Compressed Air Supply

Generally, the gas turbine blade is exposed to a hot gas temperature coming from the combustion chamber. For cooling purposes, a fraction of the compressed air is taken from the last compressor stage (primarily used for the high-pressure turbine) and moved to the turbine blades, removing the heat and leaving the blade from the top through a series of film holes into the turbine section.

The cooling air temperature used in the experiment is matched with the liquid crystal wideband. The range of adopted liquid crystals used is around 11°C, where the temperature varied from 29°C to 40°C based on the calibration measurements. Several experiments are performed with the compressor using different tank configurations to find the best scenario providing steady-state cooling air. The third design is selected for the experiment, offering a uniform flow temperature. The outlet air temperature measured around 24°C, requiring heating to get in the liquid crystal wideband. Therefore, a heat exchanger is designed and used for increasing cooling air temperature.

4.2.2.1 Flow Metering

The air is compressed using a 3 HP AVAC compressor with 270 L main tank capacity coupled with two extra 340 L tanks, giving an overall 950 L coolant for each experiment. A digital flow meter measured the total flow rate moving to the supply channel for $Re_j = 7,500$. The jet velocity is calculated based on the given jet Reynolds number, therefore knowing the jet velocity, the mass flow rate is calculated. The total mass flow rate passing through the supply channel is distributed among the seven jet holes. For the sake of simplicity, the cooling air is distributed equally among all the

impingement jets to find the total mass flow rate; therefore, the total mass flow rate is calculated as follows:

$$\dot{m}_{ch} = 7 \cdot \dot{m}_j = 7 \cdot \rho \cdot V_j \cdot A_j = \rho \cdot V_{ch} \cdot A_{ch} \quad (18)$$

where \dot{m}_{ch} is the total mass flow rate entering the supply channel, \dot{m}_j is the average jet mass flow rate calculating based on $Re_j = 7,500$, and A_j represents the jet cross-section, V_{ch} is the channel velocity, and A_{ch} is the cross-sectional supply channel area.

4.2.2.2 Flow Temperature Control

In this section, the proper arrangement of tanks is evaluated, using three air designs temperature outlet. For all cases, the air is compressed using a 3 HP ABAC compressor. Three experiments are performed and described in Figure 19 to testify and measure the outlet flow temperature for a steady mass flow rate.

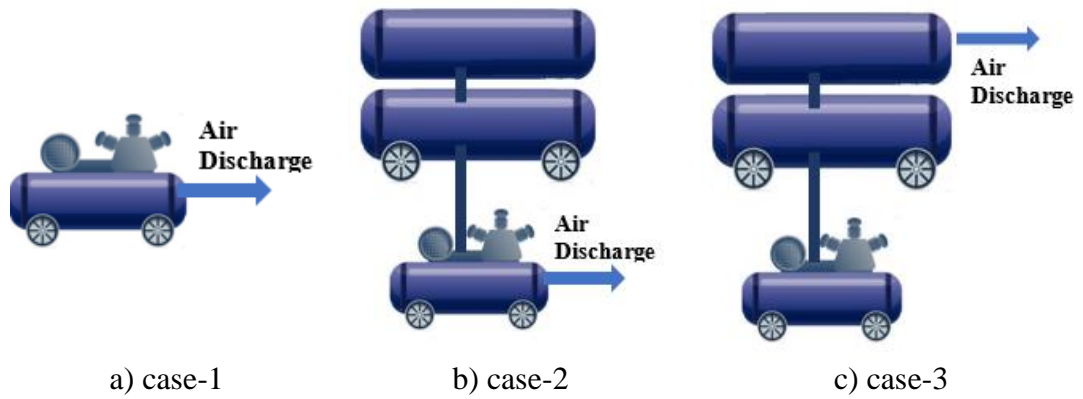


Figure 19: Three supplied-air configurations

The result indicated the air temperature reached 50°C in the main tank to get a steady-state mass flow rate while the compressor is running. This case is not applicable since given the outlet temperature exceeded the liquid crystal wideband.

Furthermore, the compressor must continuously work to reach steady-state conditions. When turning off the compressor to use only compressed air inside the main tank, the mass flow rate will remain unsteady, and the amount of air is not sufficient. To ensure the amount of cooling air guarantees to perform each run of the experiment, two more tanks are added to case number 1, as shown in Figure 19 (a) and (b). The lab ambient temperature is around 20°C, and two added tanks are exposed to the environment. As the compressed air passed through the pipe connection and moved to other tanks, the air temperature drops to 24°C; however, the experiment required temperature is about 27°C. Therefore, a heat exchanger helped to increase the cooling air temperature before entering the test section.

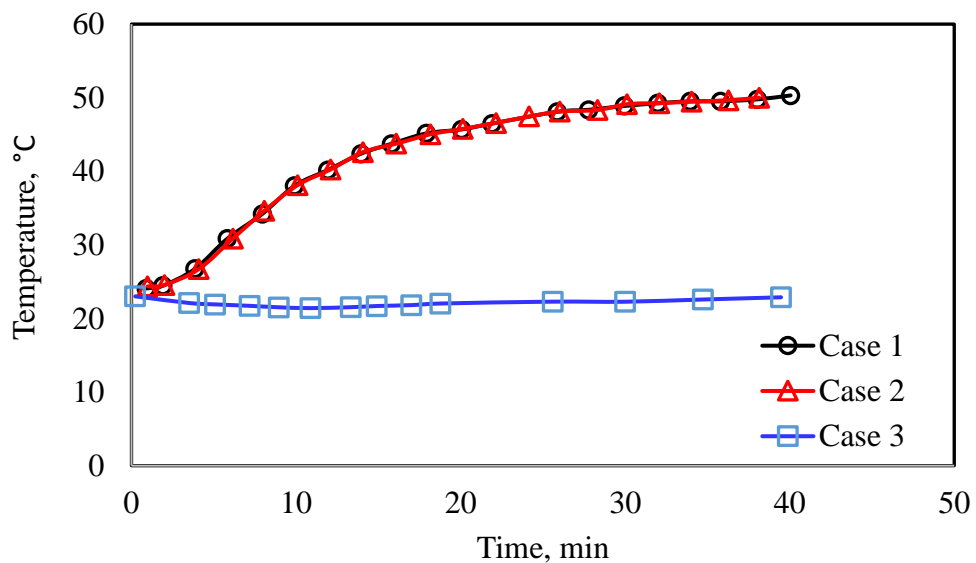


Figure 20: Cooling air outlet temperature for three different cases [56]

As shown in Figure 20, no difference existed in the first and the second cases' outlet temperature. The temperature remained steady for cases one and two after 40 minutes. The third case is more practical as the temperature steadied after 20 minutes,

and the air temperature fell below the liquid crystal wideband, heating it to 27°C using a heat exchanger. Four electrical heaters with 2000 W output power are submerged in the water bath to boil the water and maintain the water temperature at 100°C. The water bath had an inlet and outlet, where the cooling air from the compressor enters the helical coil, collecting heat from the boiled water and leaving the bath at the required temperature of 27°C. As some losses occurred from the heat exchanger to the test section due to the convection heat transfer, the inlet temperature is measured at the leading-edge inlet. For this matter, a T-type thermocouple is fixed at the supply channel inlet while monitoring the inlet temperature to ensure the experiment is running with the required cooling air temperature.

4.2.3 Hot Gas Simulation

Gas turbine blades are exposing to a hot gas coming from the combustion chamber. A flexible electronic heater with a constant heat flux (1000 W/m^2) is employed for the leading-edge target surface to simulate the condition. Generally the heat flux is not uniformly distributed on the leading edge surface in the actual turbine blade due to the root's flow behavior and the blade's top. Based on the actual gas turbine blade shown in Figure 21, the maximum temperature due to the convection occurred almost at the center of the turbine blade, but in this experiment and the CFD simulation, the researchers assumed a uniform heat flux along the target surface. The maximum heat transfer happens at the blade center, and it has a minimum value at the tip and the root due to conduction heat transfer as well as the flow behaviour. The heater applied a constant heat flux uniformly along the leading edge, using a thin

heating element distributing temperature uniformly around its surface. A DC power supply poared the heater through the slip ring at various rotating conditions.

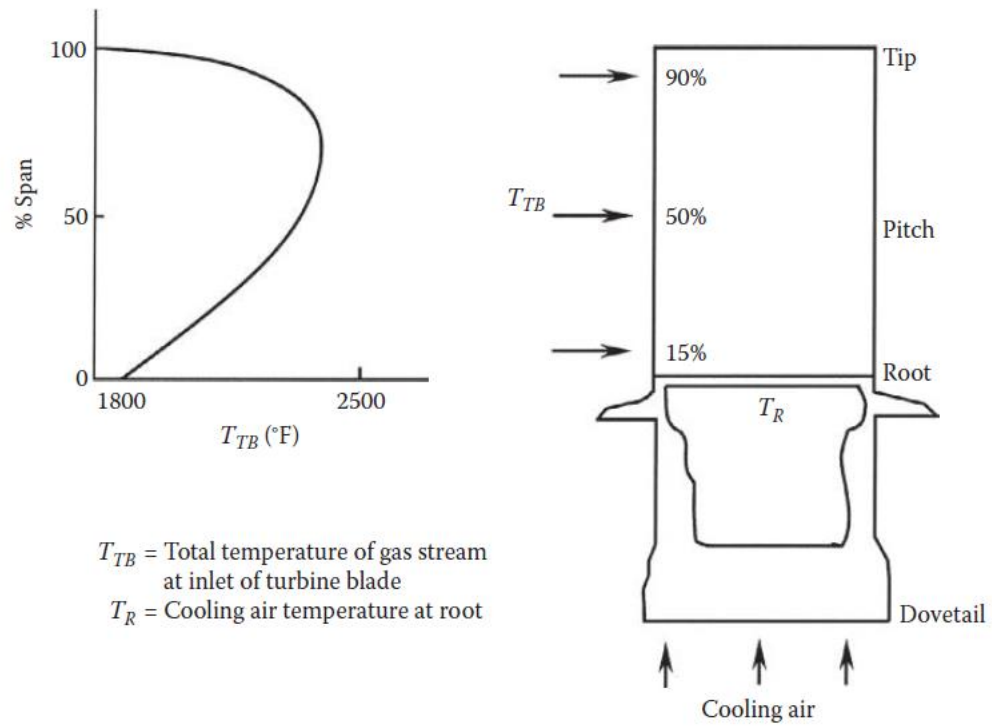


Figure 21: Temperature distribution along the actual turbine rotor blade [4]

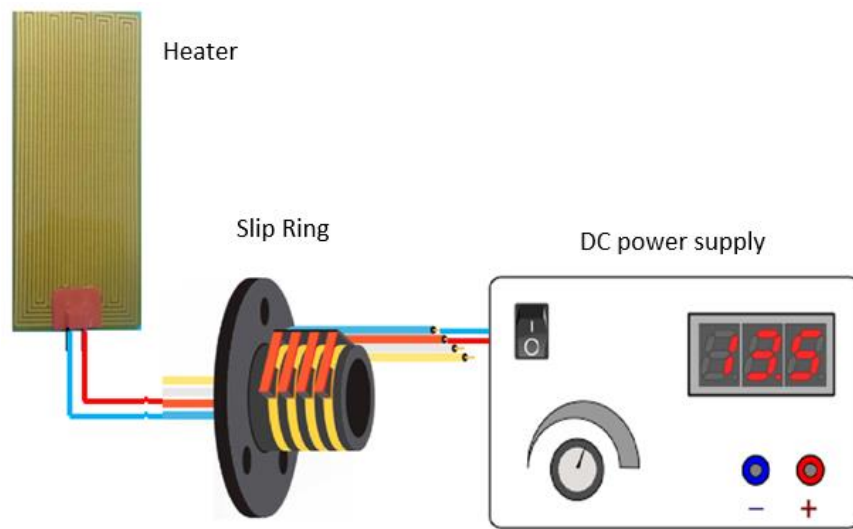


Figure 22: Flexible heater arrangement

4.2.4 Temperature Measurements

Several techniques are conducted for measuring the target surface temperature. In the current study, the target surface is under rotating conditions. At rotating conditions, two temperature methods are employed in the experiment: TLC technique and array of thermocouples.

4.2.4.1 Thermochromic Liquid Crystals Technique

In recent years' authors have started using novel technique to measure temperature knowing as thermochromic liquid crystal technique (TLC), to study heat transfer problems [50, 53, 57, 58]. The effect of rotation on gas turbine blade thermal performance is one of the fields to which the method is applied. Each liquid crystal type has a unique temperature range, a wideband. By exposing a liquid crystal to a temperature within the same range, crystals change the phase and temperature. They form as a color. The liquid crystals used in the experiment entailed R30C10W Hall Crest manufactured. The lowest temperature in any TLC forms red, while the highest

temperature appears blue. Liquid crystals pasted on the Kapton heater are covered by a transparent tube to prevent any effect from the environment during rotation and observe the temperature distribution on the heated surface.

TLC calibration represents the first step in data processing to convert the target surface color map's images to the corresponding temperature value map. The adopted calibration method is depending a steady state TLC calibration by running a separate test under the same lighting arrangements, where the test surface is heated under constant heat flux condition, the temperature of the heated region is captured by IR Camera also measured by a thermocouple located at the center of the tested regions in an isolated area from any hot or cold air stream. Simultaneously an image is a captured. This process is repeated to cover the TLC wideband. After processing the image pixels and converting them to Hue values, for each test an average Hue value is obtained which later fitted to the corresponding temperature values on the curved surface. For demonstration, see Figure 23.

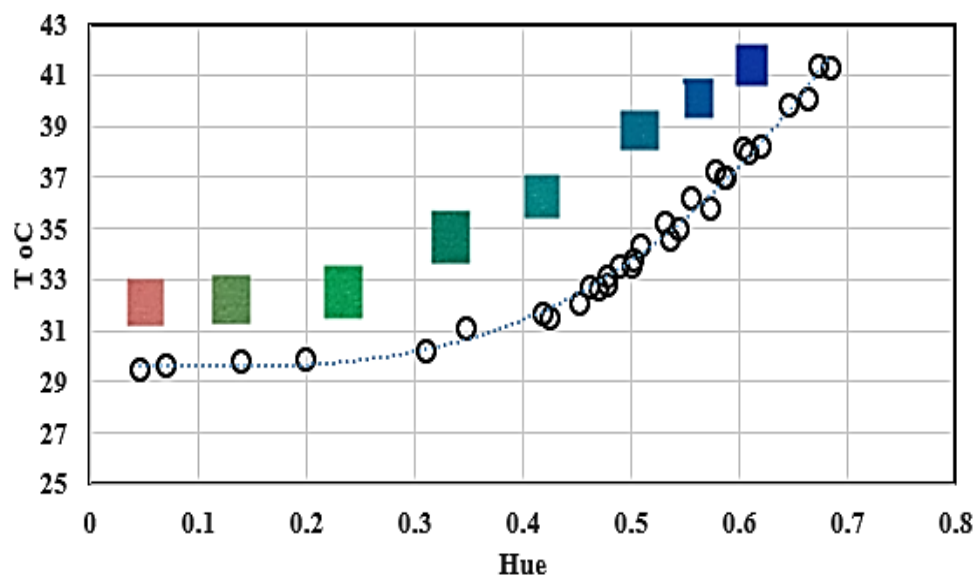


Figure 23: Liquid Crystal Calibration Hue vs. Temperature

4.2.4.2 Thermocouple Measurement

In this method, the local area temperature is measured using an array of thermocouples. Seven T-type surface thermocouples made by Omega are attached to the target surface to measure the temperature at the focal point of each impingement jet. Figure 24 shows the actual heater with the thermocouples pasted on the surface and the schematic thermocouples connection to HD32.8.16 data logger using slip ring. Each thermocouple is pasted in front of the corresponding jet, having a thin wire carefully fixed on the curved surface to minimize the effect of flow behavior on thermal performance inside the cavity during impingement.

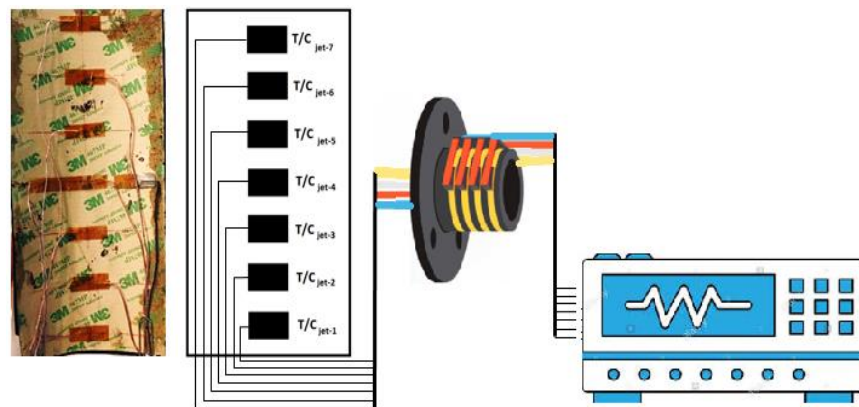


Figure 24: Connecting thermocouples to datalogger through a slip ring

4.2.5 Camera and Lighting Setup

During rotating conditions, the temperature mapping on the target surface created by the liquid crystals coated on the target surface is captured by a high-speed camera. Therefore, the camera is located in front of the leading edge and captures the rotating target surface. The major interest in this validation is to capture qualitatively the behavior of the target surface temperature mapping between the CFD target surface contours and the liquid crystal temperature mapping. Quantitatively, the interest is

focused on the center line temperature variation from one jet to another along the test section. Therefore the images are taken at one location on the leading edge center and the stagnation point. But the leading-edge geometry's curvature is not considered. Figure 25 outlines the camera location. The flexible heater entails the red color covered by the liquid crystal (green color) and the transparent acrylic tube.



Figure 25: Target surface configuration with camera position

1. Transparent material 2. Liquid crystal sheet 3. Capton heater 4. Guppy F-125 camera

4.3 Test Section

The leading edge of the gas turbine blade is simulated in this section. Impingement cooling holes with the supply channel is manufactured using HDPE material. The HDPE sections consisted of two connected parts forming a single impingement shape. The reason of having them in the separate parts is the challenges we faced during manufacturing for the rectangular supply channel.

The length of the leading edge is $L_{LE} = 216$ mm, and the jet diameter is $d_j = 8$ mm. The inlet hole diameter is $D_{ch-in} = 9$ mm, and the jet thickness equaled $t = 12$ mm. The jet to jet distance is $l = 32$ mm. A semi-cylindrical acrylic tube provided a curved

leading edge. The leading-edge diameter is $D_{LE} = 50$ mm, and the distance from the jet to target equaled $l = 25$ mm.

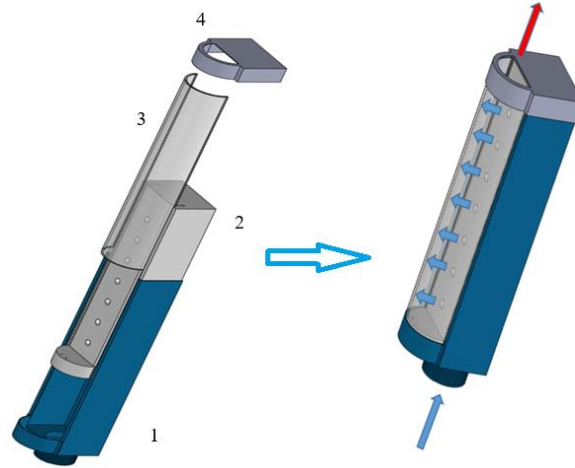


Figure 26: Experimental test section

1. Housing, 2. Filler, 3. Transparent acrylic tube, 4. Cap

The semi-circular acrylic tube, attached to the Nylon impingement model, is covered with 2 mm metal sheet housing and affixed to the rotating arm using a male thread designed on the bottom. The arm radius is $R_{mean} = 500$ mm. Figure 26 details the test section.

As shown in Figure 26, the test section is designed to have a flexible filler. The filler inside the leading edge can be replaced with another configuration to study other parameters such as a different number of jets, jet diameter, and jet to target distance. A semi acrylic tube with the transparent material covered the whole leading edge to record the TLC mapping. An adapter is affixed to the bottom of the leading edge to connect with the hose, preventing leakage.

4.4 Experimental Procedure

The experiment, performed at the UAEU facility, implemented the designed and build home setup, considering all the safety and precautions. The following steps summarize the procedures to run the test:

- Charging three-storage tanks by running the compressor for around 30 minutes until the pressure reaches 10 bar.
- Coolant mass flow rate must correspond to $Re_j = 7,500$. Regulating the air storage tank flow to 2 bar using a pressure regulator and setting the needle valve to a flow rate of 165 L/min ensures the required mass flow rate.
- The cooling air temperature passing to the test section is controlled by a heat exchanger located between the tanks and the test section. The temperature-controlled to guarantee a temperature around 27°C at the inlet of the leading edge. The cooling air temperature is monitored at three locations: one thermometer at the compressor's exit and the rotary union inlet, and the primary one using a T-type thermocouple to the inlet of the leading edge.
- After controlling the coolant mass flow rate and its temperature to the test section, a DC power supply at 19-20 V powers the leading-edge flexible heater.
- After getting steady temperature distribution on the target surface, the electric motor is turned on and the rotation is controlled using frequency controller and the rpm is monitored accurately using a digital Tachometer TACH20.
- Four LED lights are used to make the test section brighter. Then, the camera is programmed to record many images at the frame rate of 32 per second. The

most critical factors in setting the camera constitute exposure time and gain value, where each rotation differs in terms of image quality. We used the same exposure time and the gain value for all the rotating conditions to have the same quality images for data processing. After running several experiments, the exposure time 200 μ S and 20 for the gain value are selected.

- After finalizing the mass flow rate, the rpm, the heat flux, and the lighting arrangements, the camera will capture images of leading-edge surfaces at various rotations.
- Parallel to the process of setting the cooling air flow rate, temperature, and experimentation, the data logger collects and stores all thermocouples measurements.

4.5 Validation Test Cases

For the validation, due to the limited compressed air supply, experimental validation is limited to jet Reynolds number of 7500 and rotation of 50, 100, 150, and 200 rpm. Table 7 list all validation cases:

Table 7: Case validation study

$Re_j = 7500$	
Case Number	rpm
Case 1	0
Case 2	50
Case 3	100
Case 4	150
Case 5	200

Chapter 5: Results and Discussion

In this chapter, numerical results and analysis are performed using Fluent module of ANSYS Workbench, the commercial numerical simulation software. The results report the effect of jet Reynolds number and the jet rotation number on impingement cooling behavior such as streamlines, local and overall surface Nusselt number, and jet mass flow rate. Firstly, the numerical results at $Re_j = 7,500$ are validated using experimental data for five different rotating conditions varied from 0 to 200 rpm. . After validating and observing a design imperfection at the test section's inlet which will be explained later in the discussion part, the model's final design is modified and employed in the numerical analysis.

5.1 Validation

A concern about any numerical study involves how the results mimic physical reality; thus, the numerical validation quality during the experiment reflects the accuracy of the numerical results. In this investigation, numerical results are validated with experimental studies performed by the designed test rig. Two temperature measurements using TLC and array of thermocouples are employed in the experiment. TLC comprehensively mapped temperature on the leading edge which will be used to investigate the center line temperature on the curved surface. Also, seven surface thermocouples are located in front of each jet's physical location on the target surface to provide the localized temperature. The test section of both the numerical analysis and the experimental investigation are considerably similar. A few differences between the two geometries are taken into consideration during the result comparison, summarized as:

- Leading-edge thickness is zero thickness in the numerical analysis and 4 mm in the actual experiment.
- Constant heat flux of 600 W/m^2 remained uniform in the numerical analysis; meanwhile, the supplied heat varied in the experimental setup due to the temperature's non-uniform distribution due heat transfer losses and the end effect which will be explained in the discussion chapter.
- Environmental losses are not accounted in the numerical analysis; however, they existed in the experiment.

For the validation, two groups of results are emerged. The first group, Figure 27 to Figure 31, consisted of three temperature contours produced from the numerical analysis, the experimental TLC imaging, and the TLC-calibrated contours. The second data group used for validation are presented in Figure 32 to Figure 36, comprised of the localized surface thermocouple temperature at the centerline of the leading edge corresponding to the seven jet locations; and two distributed temperatures at the leading edge centerline, extracted from the numerical analysis and the TLC calibrated temperature contours.

5.1.1 Temperature Contours Evaluation

Figure 27 to Figure 31 plot three temperature contours, corresponding to the numerical analysis, the experimental TLC image, and the calibrated-TLC temperature contours, for 0 (stationary), 50, 100, 150, and 200 rpm, respectively. As illustrated in Figure 26, the flow enters the test section from the bottom of the square channel and exits at the top of the semi-circular channel. The middle black dots (Figure 27) represent the physical locations in front of the seven jets, where seven thermocouples

are placed. For validation purposes, the numerical analysis, the TLC temperature contours and localized thermocouple measurements for all tested cases are compared. The jet impingements matched in shape and magnitude, as portrayed in the second data results, especially for jets three to seven. Even the unexpected behavior at jets one and two is appropriately captured in the experiment and the numerical analysis. Overall, a good agreement exists between the experiments and numerical results. Hence, the SST $k-\omega$ turbulence model is a proper model to simulate the jet impingement in a rotating swirl environment.

Figure 27 presents the stationary case results (0 rpm), where several observations are captured by looking at the three contour plots. For jets three to seven, jet impingement revealed an elliptically shaped region with low-temperature. This behavior is absent for jets one and two (the bottom side of the image), where jet impingement is diluted and vanished. Hence high-temperature regions are detected. The weak effect of jets one and two results from the low mass fraction observed at these jets, as explained later when discussing the mass fraction and streamline results (Figure 37 to Figure 43). As shown in Figure 27, the jet impingement region for jets one and two had higher temperatures than the other jet impingement regions. The same observations are occurred for rest of the cases, illustrated in Figure 28 to Figure 31, corresponding to 50,100, 150, and 200 rpm cases, respectively.

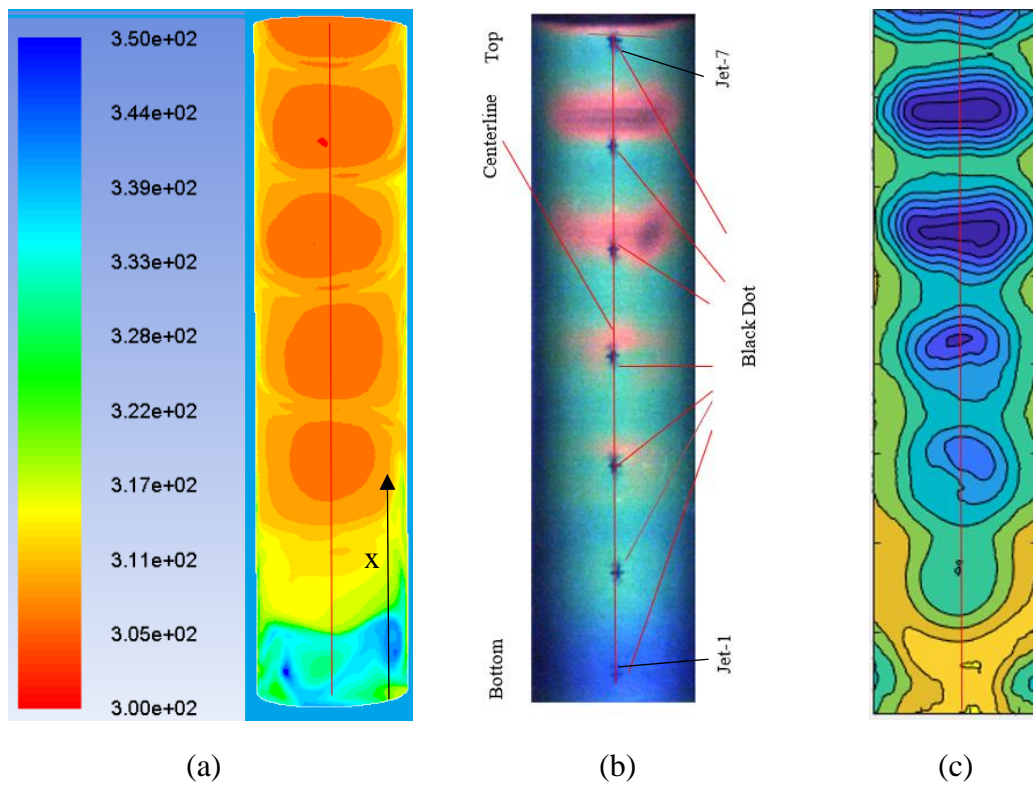


Figure 27: Target surface temperature counters at 0 rpm (stationary case) is displayed using (a) CFD temperature contours, (b) experiment TLC image and (c) TLC calibrated contours

In Figure 27, the vertical black line along the curved surface represents the center line. Black dots on the figure (b) represent the location of pasted surface thermocouples. Also the direction of flow is shown by x-arrow moving from the bottom.

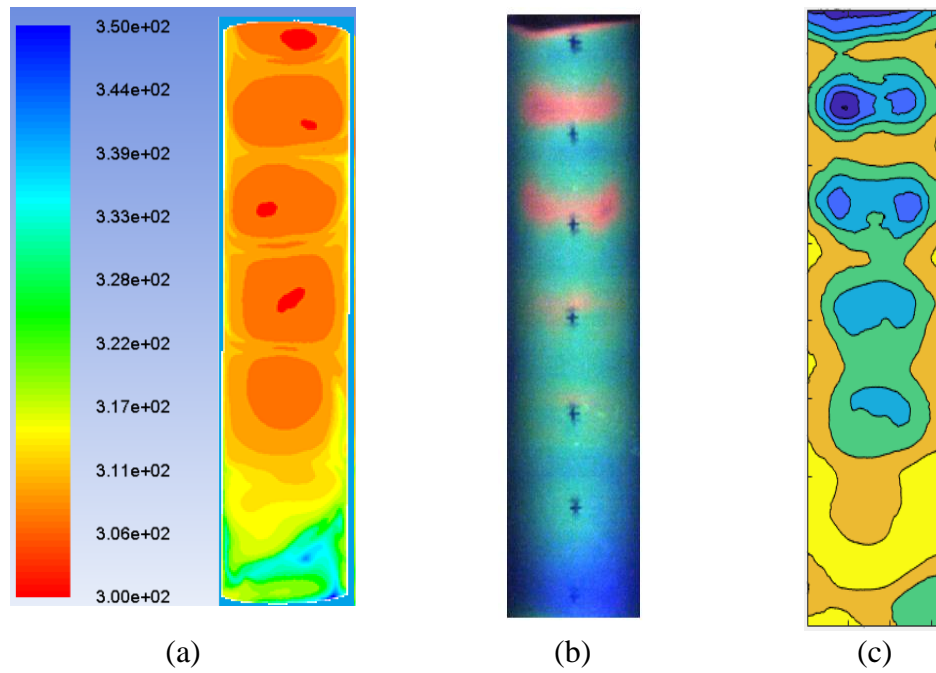


Figure 28: Target surface temperature counters at 50 rpm is displayed using (a) CFD temperature contours, (b) experiment TLC image and (c) TLC calibrated contours

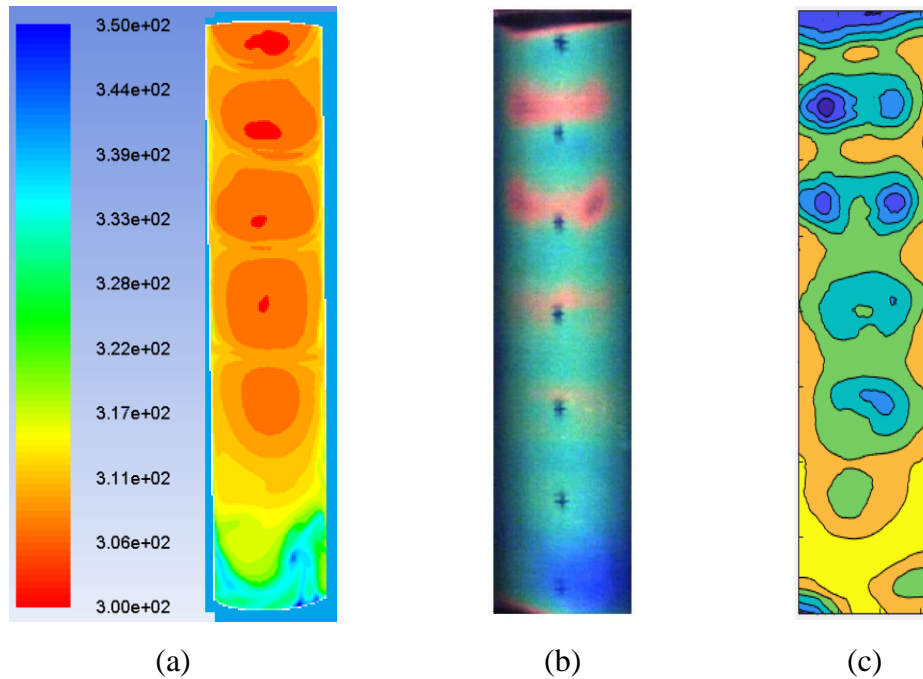


Figure 29: Target surface temperature counters at 100 rpm is displayed using (a) CFD temperature contours, (b) experiment TLC image and (c) TLC calibrated contours

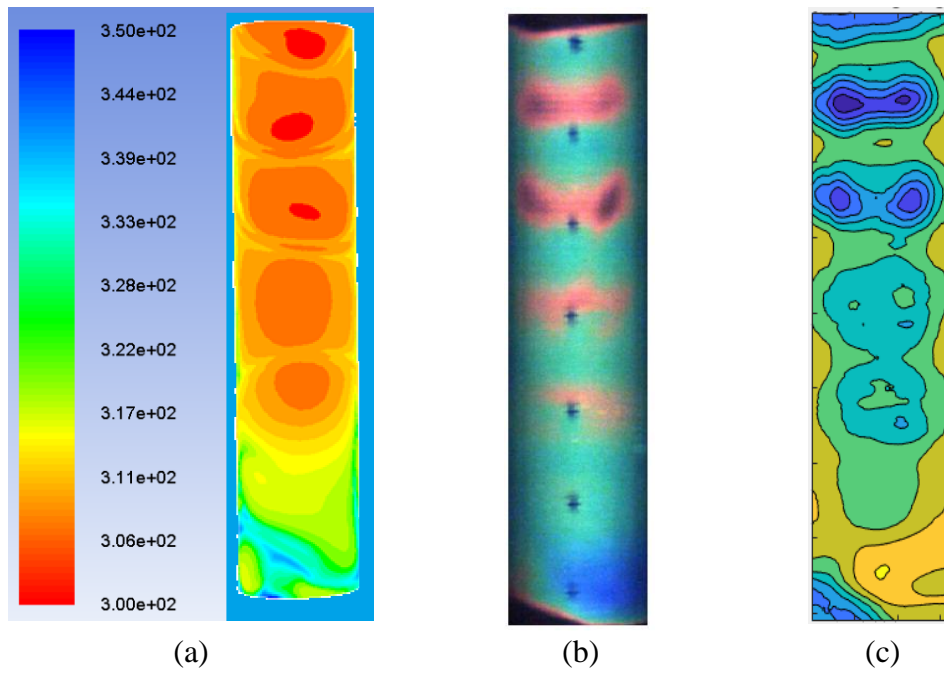


Figure 30: Target surface temperature counters at 150 rpm is displayed using (a) CFD temperature contours, (b) experiment TLC image and (c) TLC calibrated contours

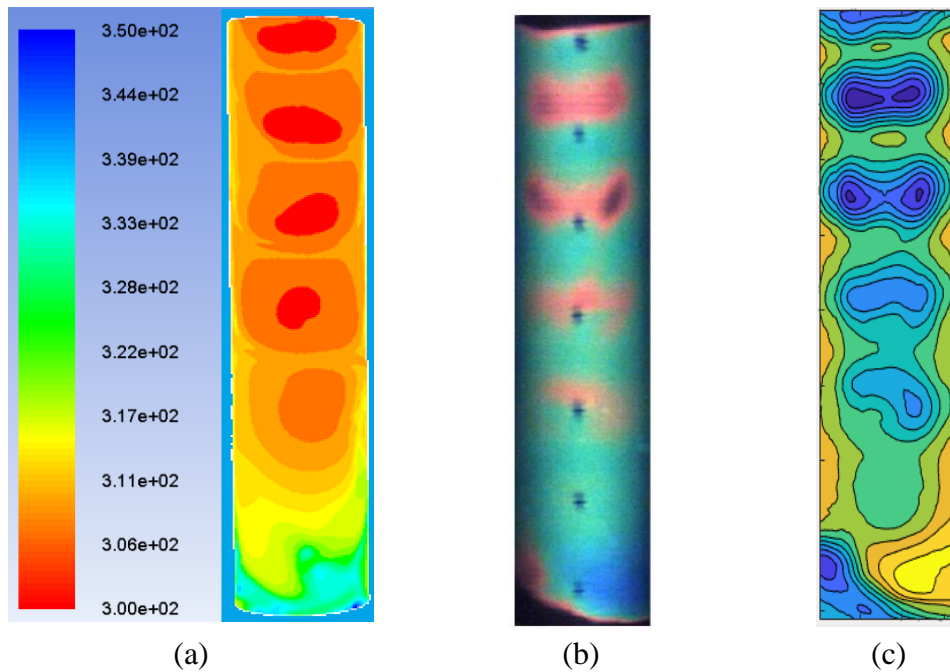


Figure 31: Target surface temperature counters at 200 rpm is displayed using (a) CFD temperature contours, (b) experiment TLC image and (c) TLC calibrated contours

The second set of results, represented in Figure 32 to Figure 36, display temperature distribution along the centerline of the target surface at $Re_j = 7,500$ for all rotating conditions varied from stationary to 200 rpm. The local temperature portrayed in these figures is from the numerical analysis, the TLC calibrated contours image and the localized thermocouple measurements. As mentioned in the experimental setup, array of thermocouples are located at the curved target surface in front of each impingement jets. Hence, seven thermocouples monitored the temperature of these points. Notably, the thermocouple measurement values are calibrated with an alcohol thermometer to avoid any offset in the reading and assure uncertainty of 0.3 degrees. On average, the correction due to calibration represented less than 3% of the total measured temperature values.

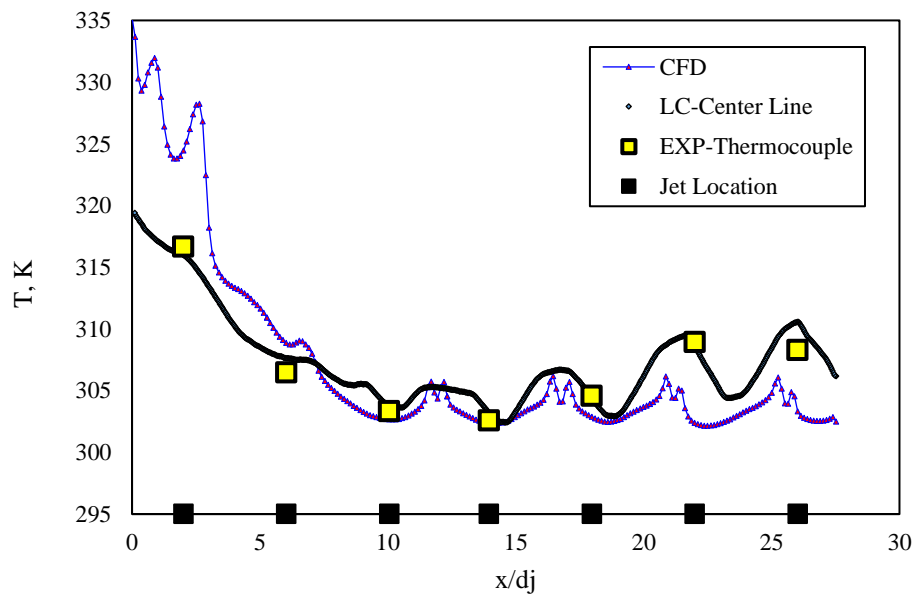


Figure 32: Centerline temperature distribution at 0 rpm

As shown in Figure 32 to Figure 36, the temperature values for jets three, four, and five under all rotation speeds have matched excellently ($\pm 1\%$). The temperature values are collected using three techniques: CFD analysis, TLC calibrated temperature, and thermocouple results. The CFD results for jets one and two overestimate the thermocouple readings and the TLC-calibrated temperature measurements as well as. For jets six and seven, the CFD results underestimated the experimental results. The CFD results for the stationary case (0 rpm) demonstrated the least deviation from the experimental result compared to the rotating cases. Comparing the results for jets one and two in Figure 32 to Figure 36 signifies as rotation speed increases, the deviation between the numerical results and the experimental data also increases.

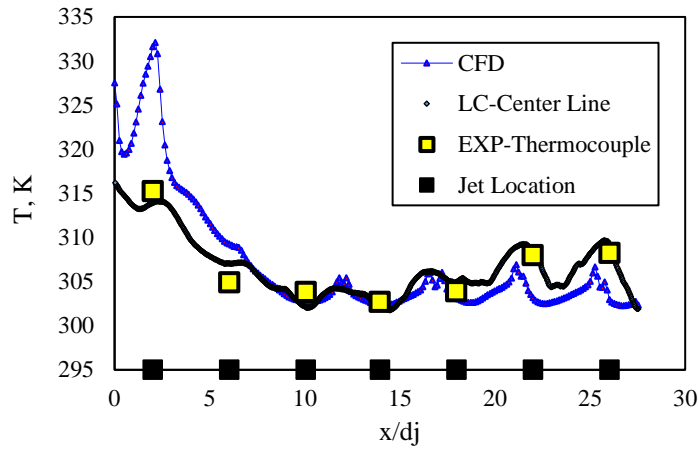


Figure 33: Centerline temperature distribution at 50 rpm

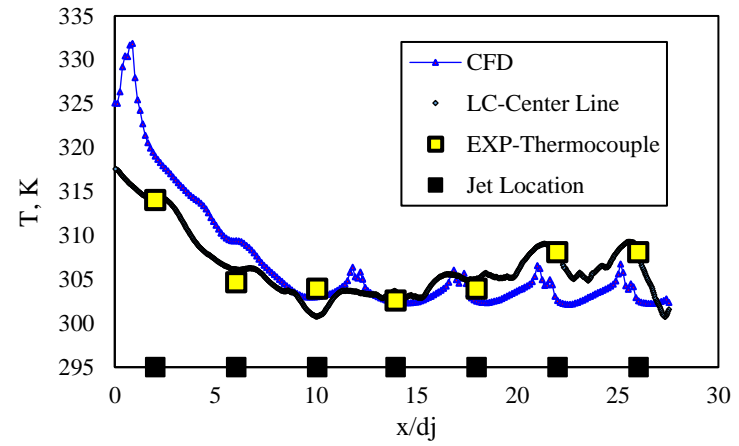


Figure 34: Centerline temperature distribution at 100 rpm

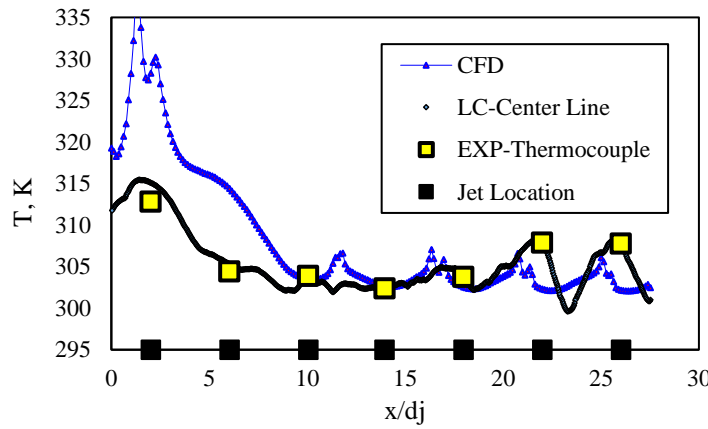


Figure 35: Centerline temperature distribution at 150 rpm

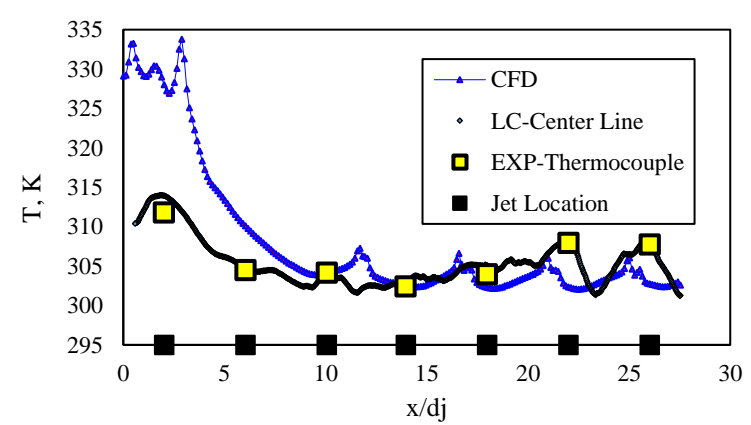


Figure 36: Centerline temperature distribution at 200 rpm

5.1.2 Impingement Flow Behavior

Jet mass flow rate and streamline contour for each jet at various rotating speed are extracted from the CFD to better understand and evaluate the flow inside the leading-edge cavity to make a clear observation.

5.1.2.1 Jet Mass Fraction

Two additional figures from the numerical analysis have been generated and presented to explain the temperature distribution contour, as shown in Figure 37 and Figure 38. The mass flow fraction for each jet is shown in Figure 37. Also, Figure 38 portrays the streamlines of the symmetry plane passing through the centerline. The results in Figure 37 explain the unexpected weakness for jets one and two. These jets (one and two) experienced backflow, and the mass fraction reversal observed around 10% for jet one and around 3% for jet 2. Backflow prevents any jet impingements and reduces heat removal; thus, the target surface experiences high-temperatures. The backflow engenders a penalty for having a small inlet diameter, directing the flow to the square supply channel. Compared to the square supply channel, the adapter hydraulic diameter, forms an internal jet flow, causes circulating near the inlet due to the sudden area expansion. The circulation region produces negative pressure near jets one and two, generating backflow. For the rest of the jets (three to seven), positive mass flow fractions are reported. This flow behavior affected the temperature and it is observed during both experimental and numerical analysis.

The CFD results for jets one and two overestimated the experimental temperature because the CFD model did not account for lateral heat transfer in the acrylic material thickness. To avoid overestimating the experimental results, one needs

to consider the conjugate lateral heat transfer, incorporating inside the wall thickness. Jets three, four, and five had minimum lateral heat transfer because they are in the middle and far from the channel edge, minimizing the lateral heat transfer. Hence the CFD model adequately estimated the temperature around these jets. For jets six and seven, the CFD results underestimated the experimental temperature. The CFD underestimated the temperature due to the outlet of the experimental test section, differing little from the CFD. A small metal step is used in the experimental setup at the outlet, holding the semicircular acrylic and preventing rotational disintegration. The metal step trapped some upstream fluid, inhibiting it from leaving smoothly as planned and calculated in the CFD model. The trapped upstream fluid reduced the heat transfer from the wall to the main flow; hence, the surface experienced high temperatures near the outlet (mainly at jets six and seven, the closest jets). Since the metal step is not modeled in the CFD to simplify numerical mesh construction, the CFD did not experience such trapped upstream fluid. Thus, near jets six and seven, the CFD results demonstrated better cooling and lower temperatures than the experimental data.

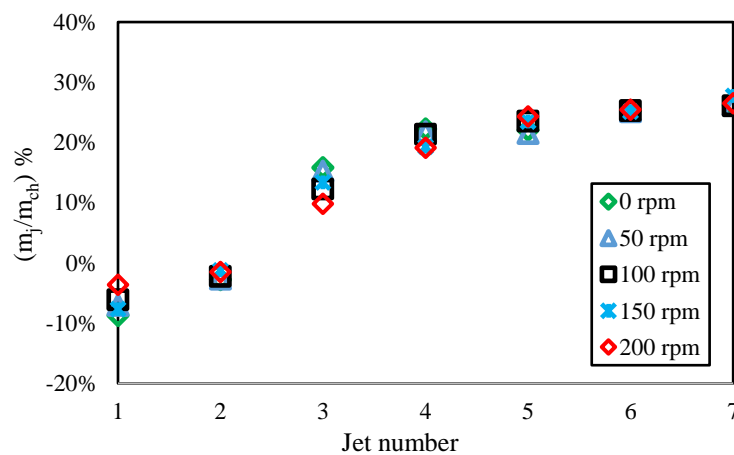


Figure 37: The mass flow rate fraction percentage for all jets

5.1.2.2 Streamlines

Generally, a good agreement between the experimental and numerical results is established. A careful investigation of the streamlines for the center cross-sectional area is shown in Figure 38. Also, a circulation flow structure near the feeding channel inlet is clearly reported. This flow circulation formed due to the small feeding channel inlet. The feed channel's adapter is connected a 9 mm hose to a 30 mm x 30 mm rectangular supply channel, as presented in Figure 10(b). The small adapter compared to the large feeding channel cross-section created a free jet circulation zone. The circulation zone has experimentally revealed deteriorated cooling near jets one and two. A flow circulation created by jet three produced a partial convection heat transfer for the region of jets one and two, then the cooling air leaves the cavity from jet one and two, depicting the negative mass flow shown in Figure 37.

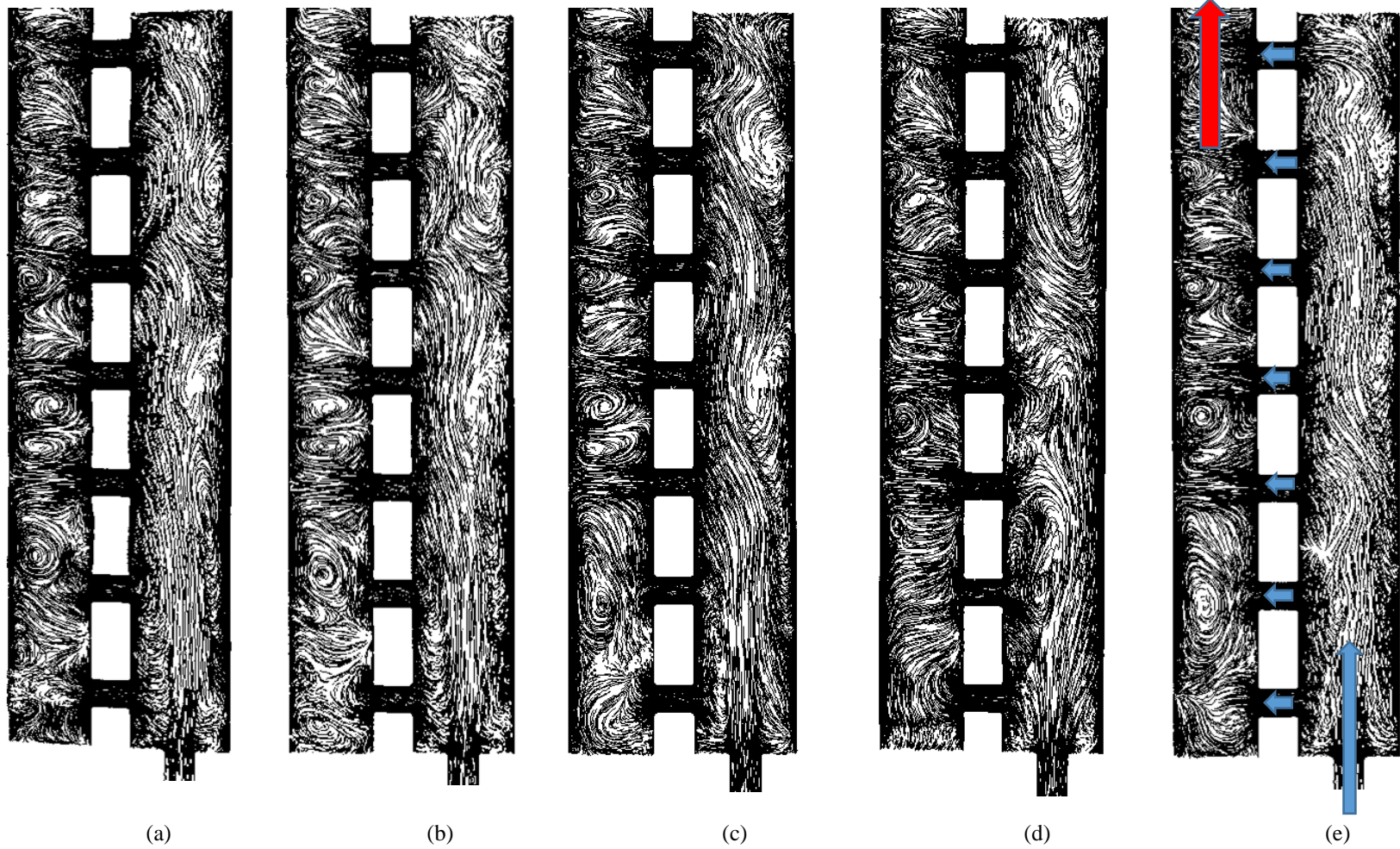


Figure 38: Center plane streamlines at $Re_j = 7,500$ at different rotational speed, (a) stationary, (b) 50 rpm, (c) 100 rpm, (d) 150 rpm, (e) 200 rpm

The cross-sectional streamlines for each jet are illustrated in Figure 39. As expected, impingement flow cooling is absent mainly in jets one and two for all rotating conditions. Impingement flow is strong and clear in jets three and four in all cases, while for upper jets, the crossflow created by jets three and four destroyed and deflected the jet direction. This phenomenon is apparent in Figure 38 as well. Figure 39 to Figure 43 provide more information at stationary and 200 rpm for jet one and four. A reverse flow occurred in jet one, as portrayed in the figures.

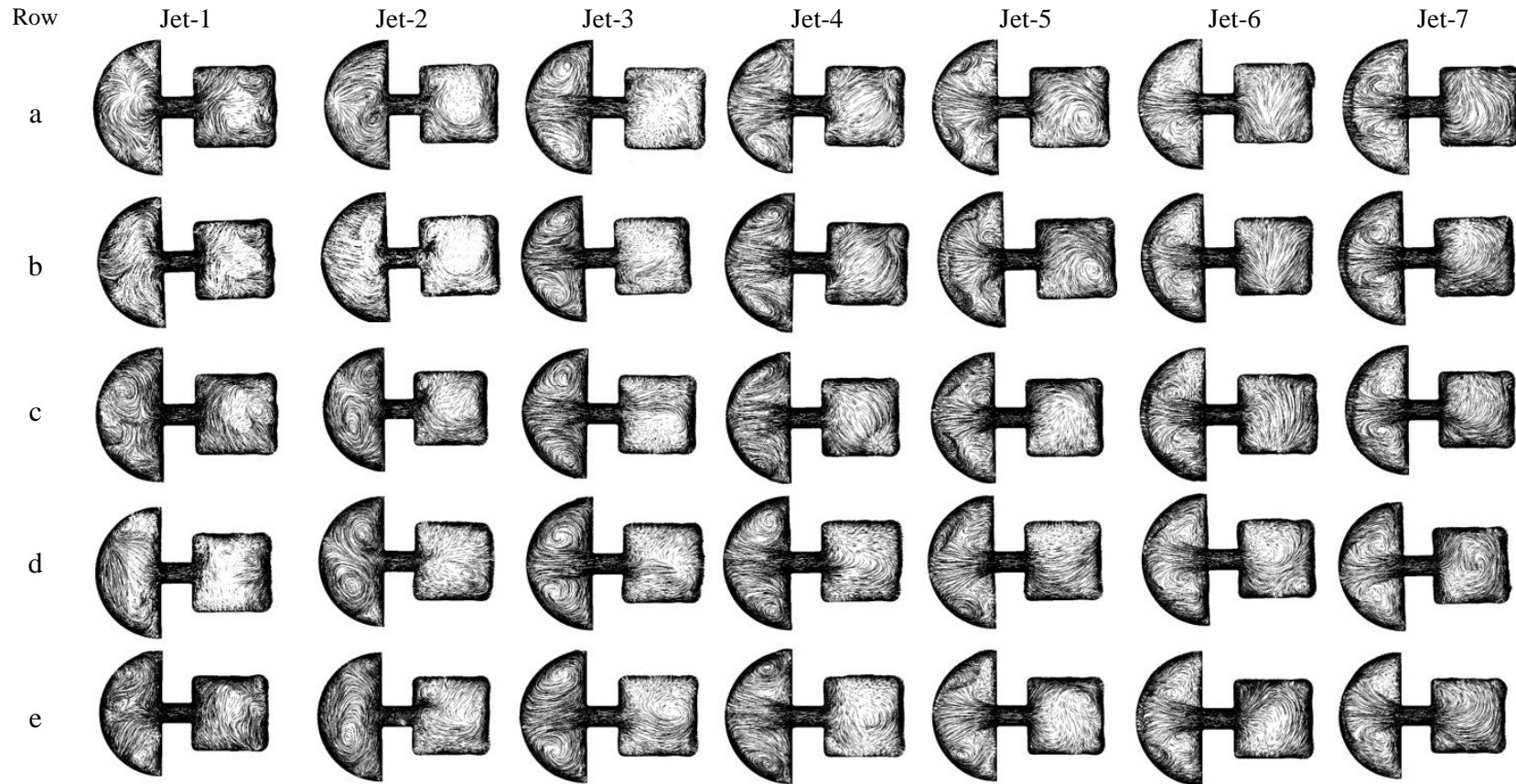


Figure 39: Streamlines of the jet cross sectional area, Row(a) Stationary, Row(b) 50 rpm, Row(c) 100 rpm, Row(d) 150 and Row(e) 200 rpm

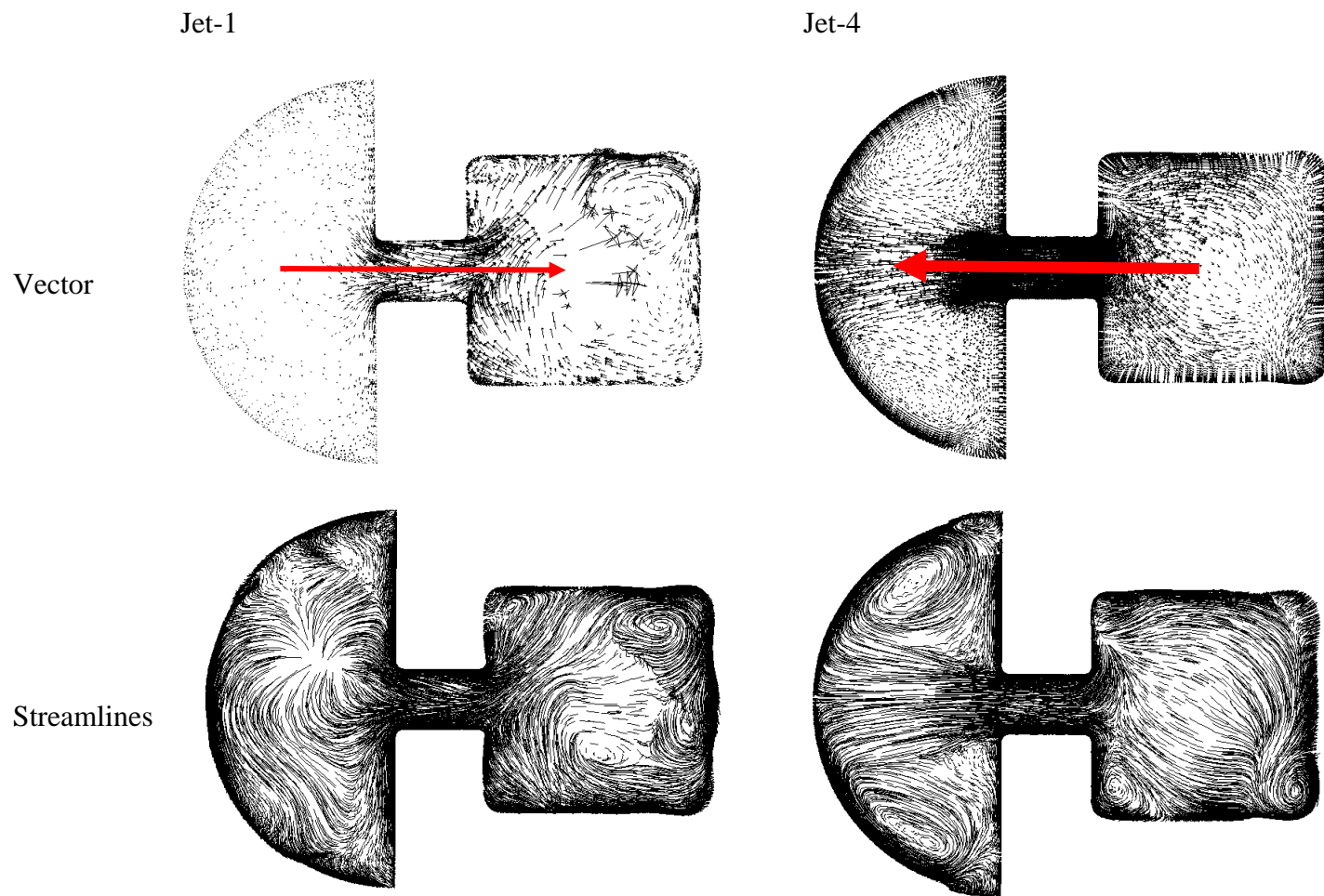


Figure 40: Vector and streamlines for jet number 1 and 4 at 0 rpm (stationary condition)

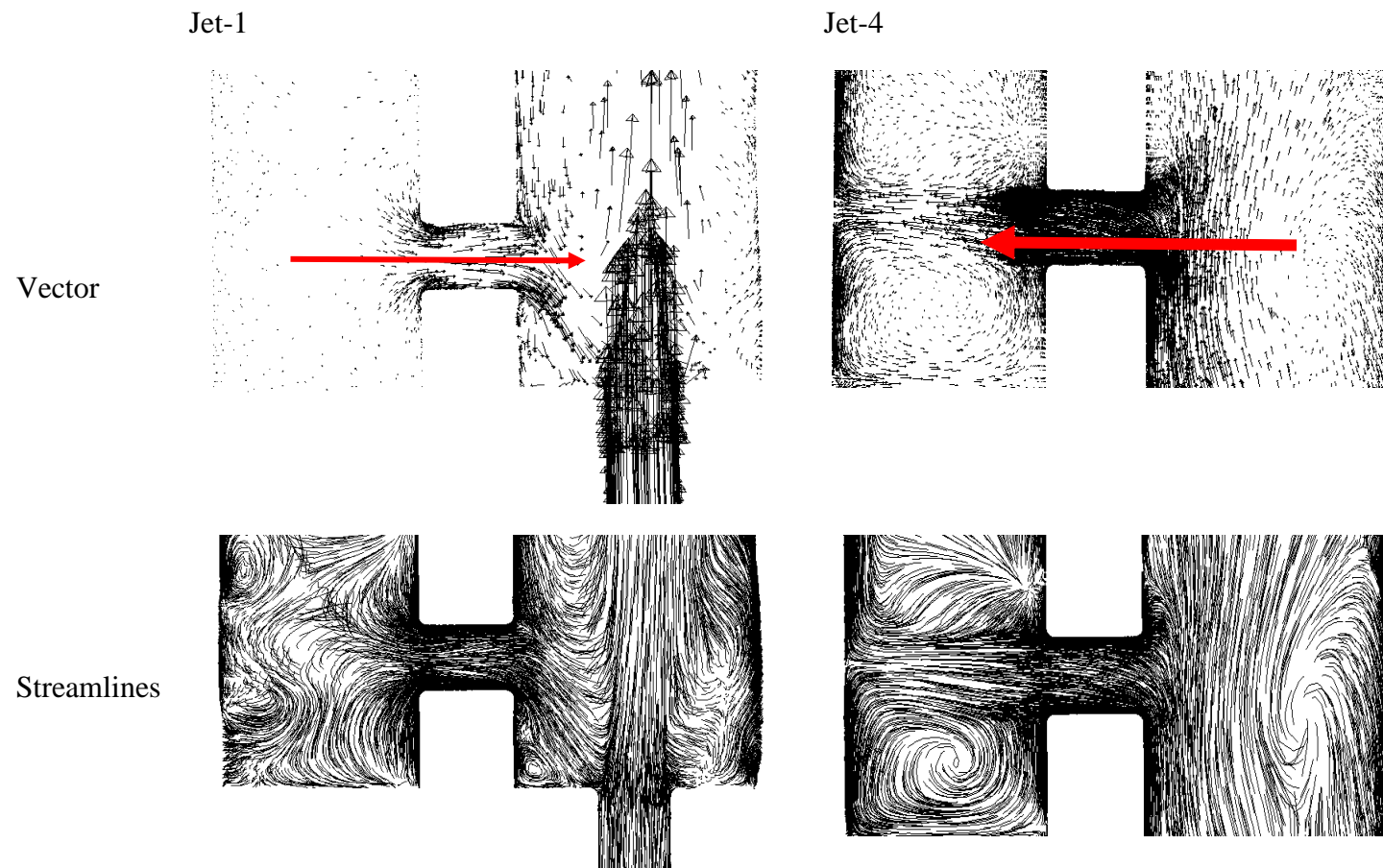


Figure 41: Vectors and streamlines for jet number 1 and 4 at the center plane at 0 rpm (stationary condition)

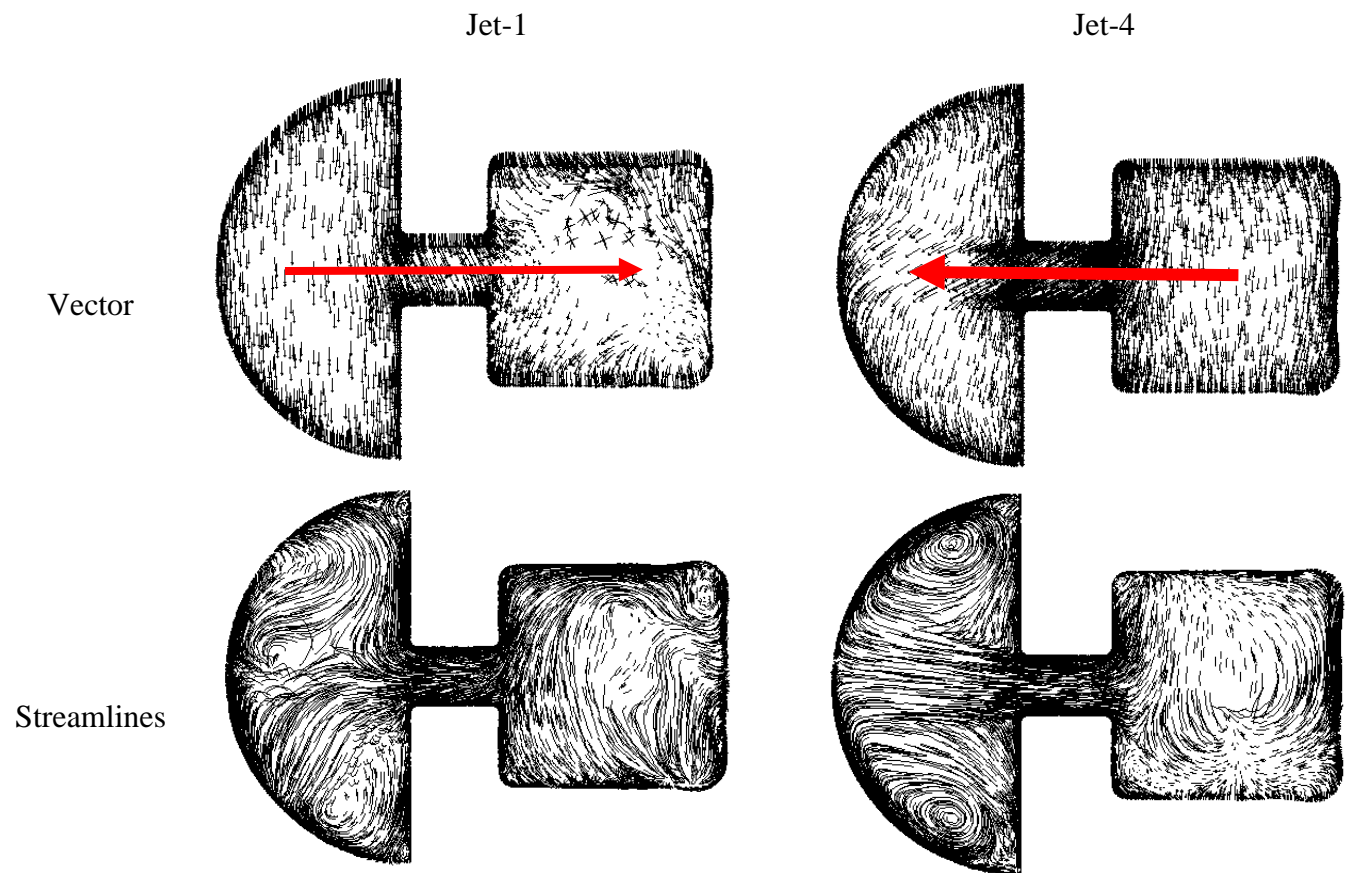


Figure 42: Vector and streamlines for jet number 1 and 4 at 200 rpm

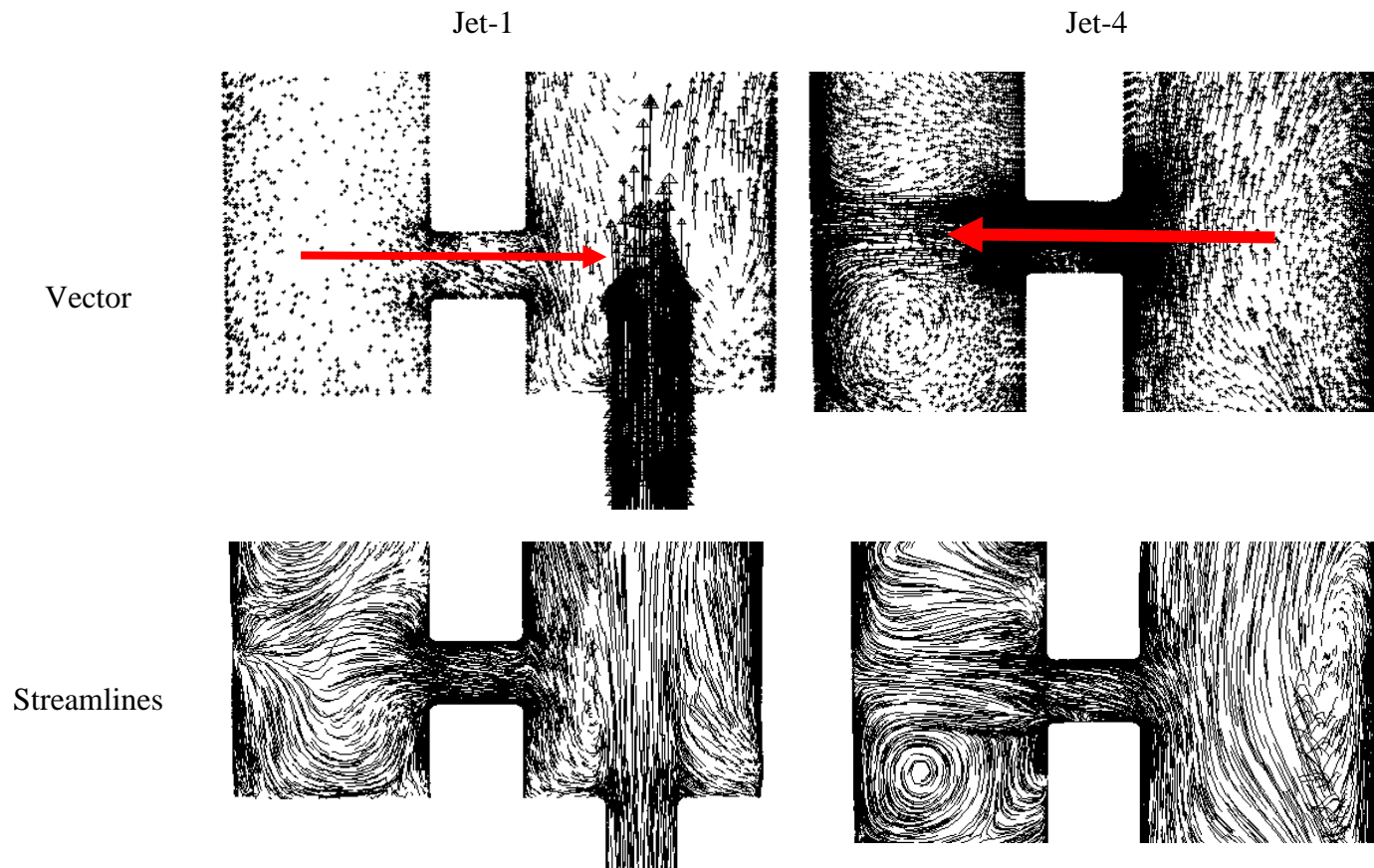


Figure 43: Vectors and streamlines for jet number 1 and 4 at the center plane at 200 rpm

A retrofit to the validated CFD model is adopted to better evaluate the impact of crossflow, the rotation and the flow behavior inside the channel. Therefore, by changing the adapter's size from 10 mm diameter to an extended 30 mm x 30 mm rectangular channel, the entrance is modified as shown in Figure 44. This retrofit helped eliminate the circulation zone and makes a better understanding of crossflow and angular velocity behaviour.

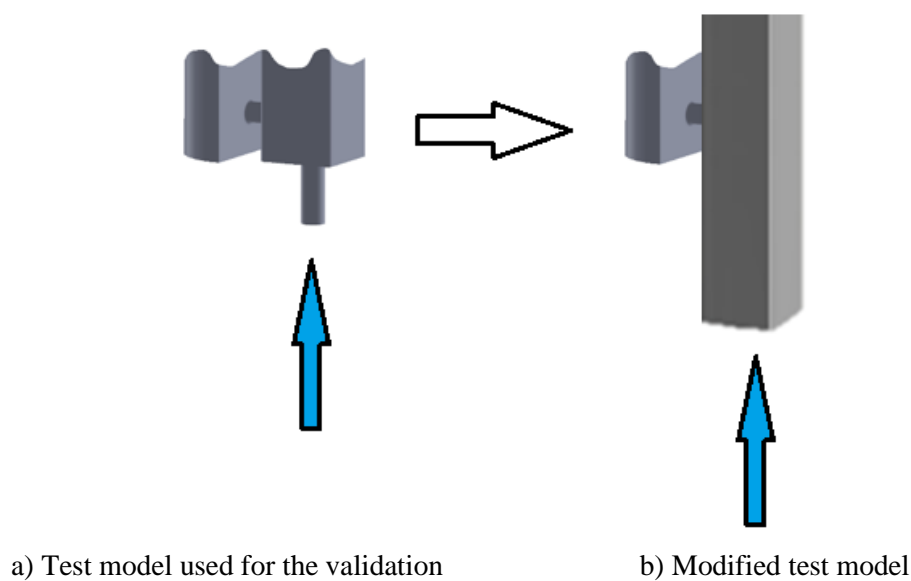


Figure 44: Modification of the inlet for the supply channel

5.2 Numerical Results for the Modified Test Section

5.2.1 Streamlines of Cross-Sectional Area for Each Individual Jet

In Figure 45 to Figure 50, the streamlines of a semi-circular cross-section passing in the center of jets one, three, five, and seven are plotted. Markedly, the streamlines behaved similarly to the streamlines in a steady-state. The streamlines represent the locus of the temporary locations of all particles that have passed through

a fixed point in the space (jet inlet) at any instant of time. Figure 45 to Figure 50 plotted one jet Reynolds number and four rpm values.

Figure 45 depicts flow of Reynolds number of 7,500 for various jets under different angular speeds. Figure 45(a), (b), (c), and (d) display the results of odd-numbered jets, respectively, under constant Reynolds number ($Re_j = 7,500$) and angular speed (rpm = 0). As shown in Figure 45(a), (b), (c), and (d), the zones with less dense lines grew as flow moved from jet one to seven. A less dense area means the flow is moving out-of-plane, indicating crossflow. A crossflow signifies the flow moves radially, crossing over the jet flow perpendicular to the radial. As expected and due to mass conservation, crossflow increased as fluid moved from jet one to seven. The crossflow broke the jet flow structure, reducing jet cooling. Similar trends are observed even at a higher number, as illustrated in Figure 46 to Figure 50. However, crossflow weakened with higher Reynolds numbers. A high jet Reynolds number depicts high jet inertia, making the jet flow less susceptible to crossflow.

The effect of angular speed can be observed in Figure 45(a), (e), (i), and (m), plotted for jet one under the angular speed of 0, 250, 500, and 750 rpm, respectively. In these figures, the deflection of jet direction rises as angular velocity increases. The angular velocity affects the flow in the channel, deflecting the jet to the bottom, forming a smaller circulation zone in the bottom and more extensive circulation at the top. Similar behavior is observed for high jet and Reynolds numbers (shown in Figure 46 to Figure 48). This effect weakened with higher jet numbers (jet five) since the crossflow dominated the flow structure and reduced rotational impact, as displayed in Figure 45(c), (g), (k), and (o). Moreover, this impact diminished with high jet Reynolds

numbers (for example, $Re_j = 30,000$), for the jet inertia dominated the flow structure and minimized rotational effects, as shown in Figure 50(a), (e), (i), and (m).

Figure 45 to Figure 50 demonstrate that jet impingement flow structure weakens as crossflow or rpm increases while strengthening as jet Reynolds numbers increase. The flow structure diminishes due to the interference between the crossflow and the jet flow. The same things happen between rpm and jet flow, where high rpm distorts the jet impingement course. The high Reynolds number causes high jet inertia, supporting the jet flow structure and substantially impinging the jet.

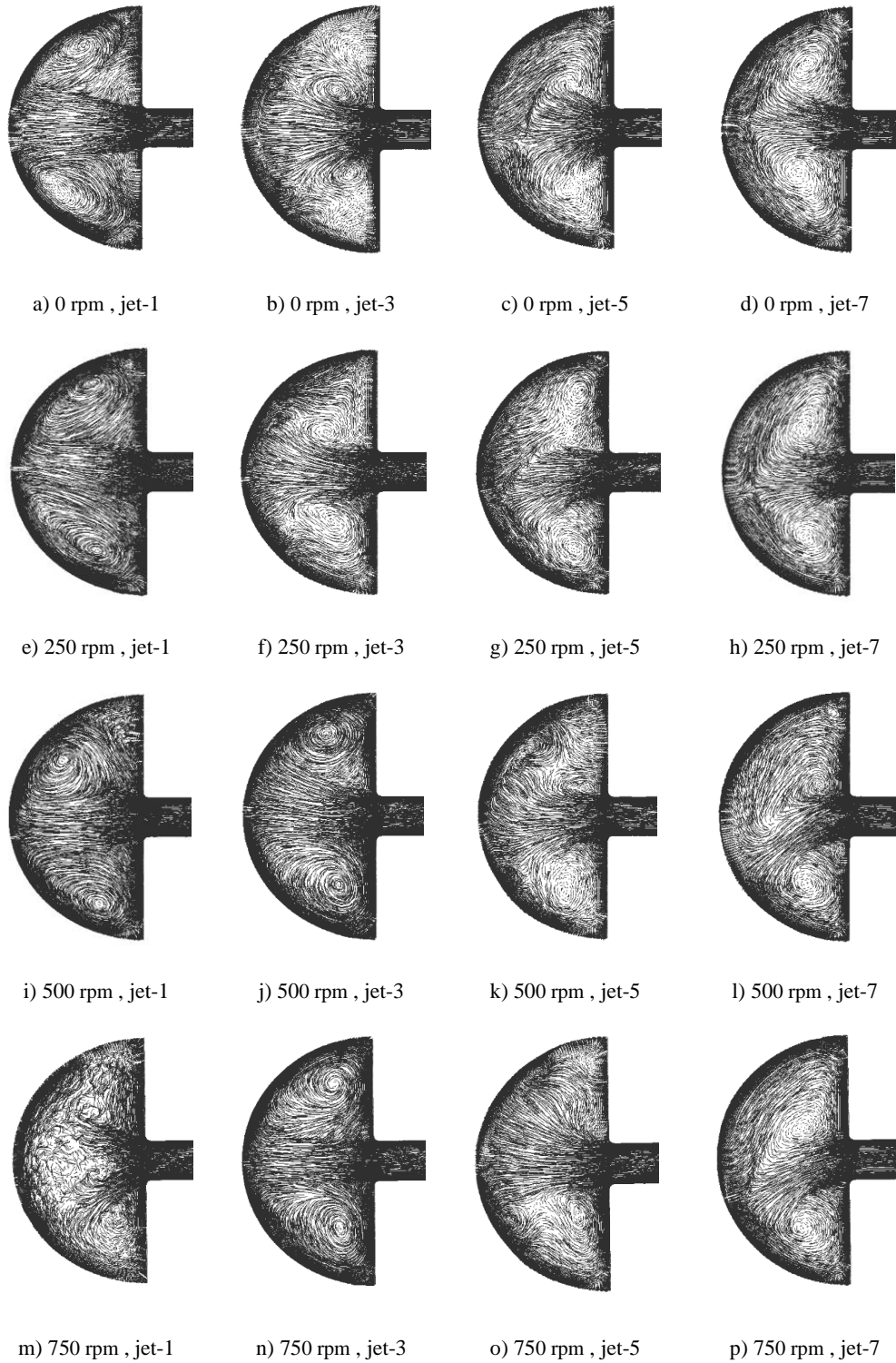


Figure 45: Streamlines on vertical cross section for jet number 1, 3, 5 and 7 for $Re_j = 7,500$ at different rpm

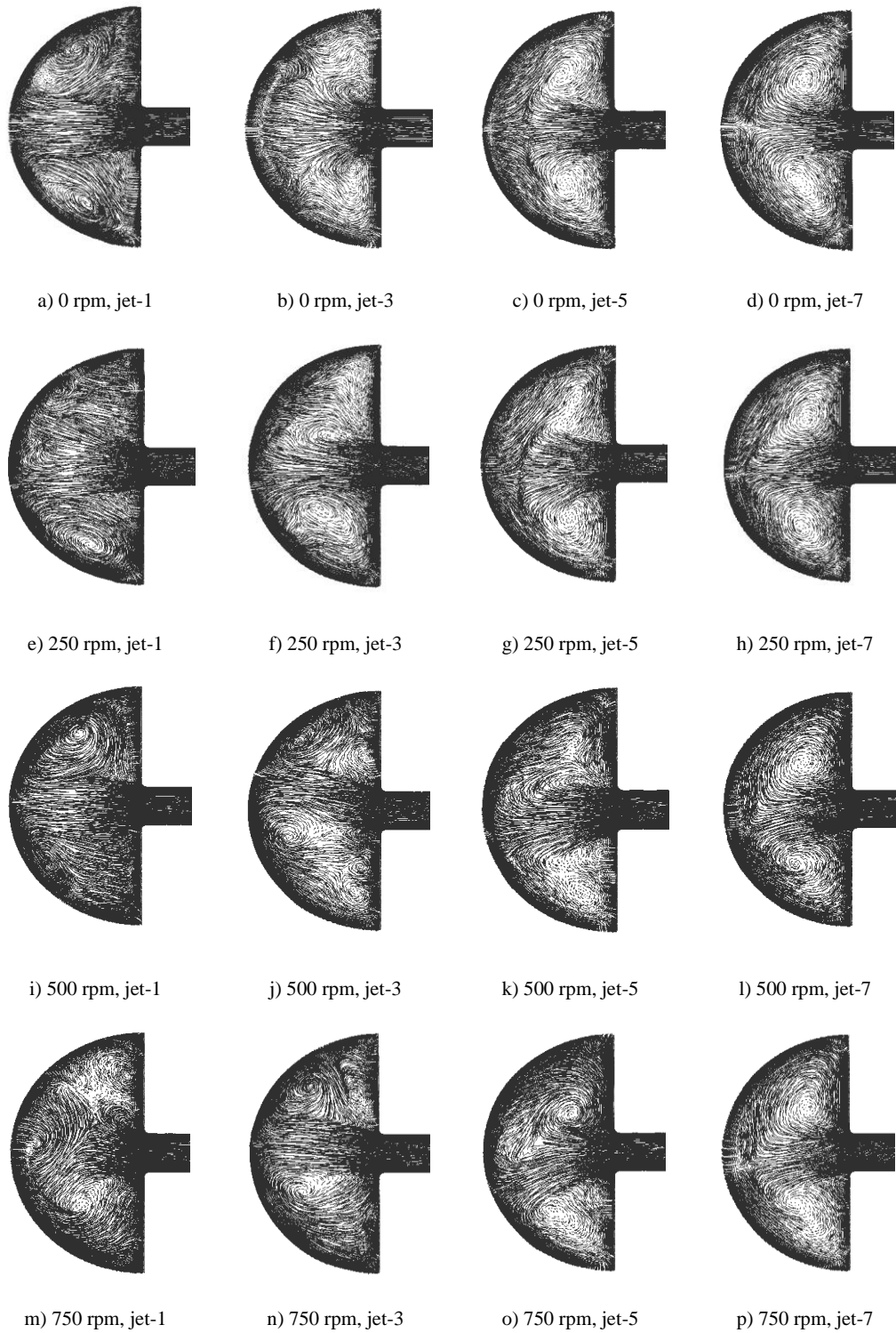


Figure 46: Streamlines on vertical cross section for jet number 1, 3, 5 and 7 for $Re_j = 10,000$ at different rpm

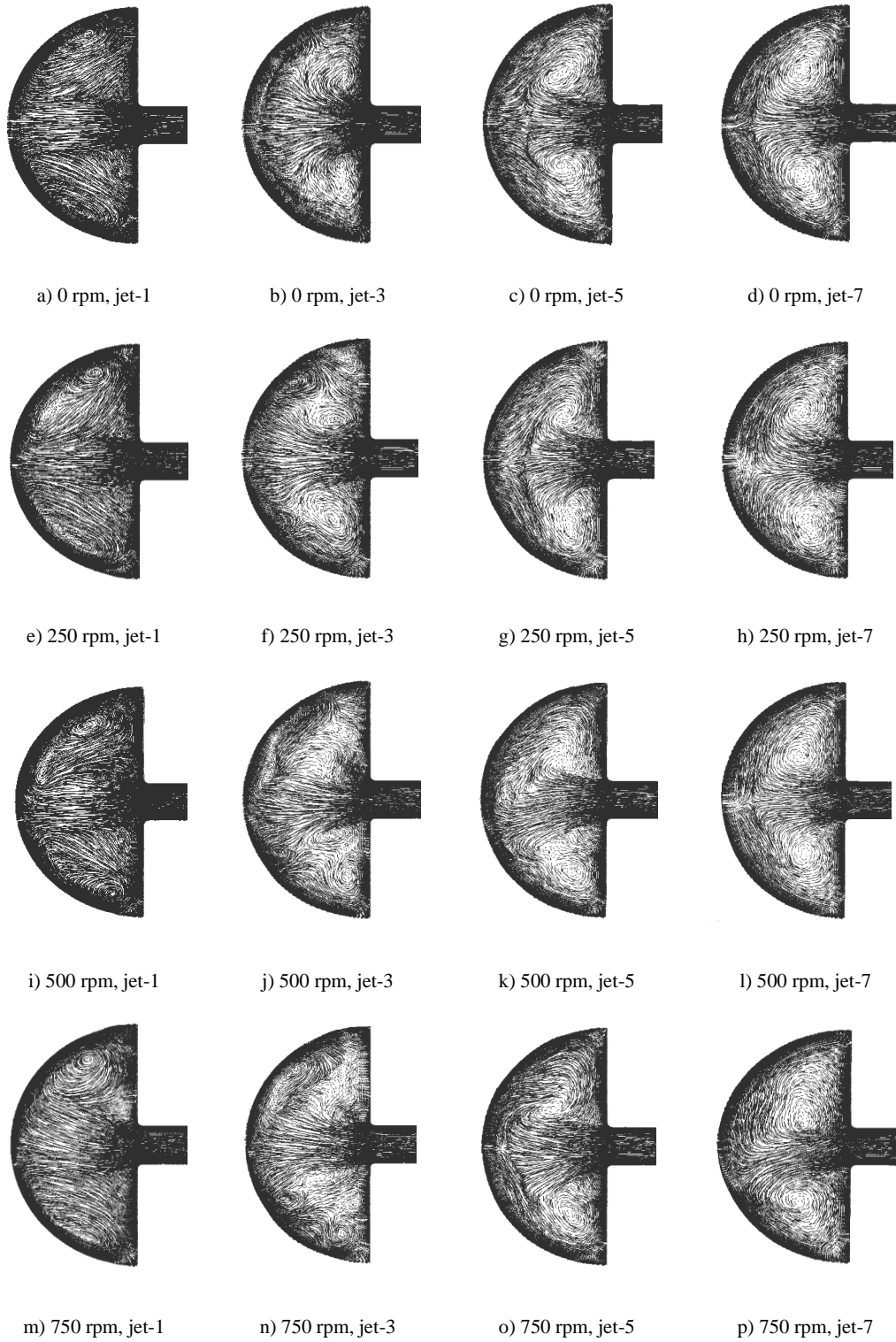


Figure 47: Streamlines on vertical cross section for jet number 1, 3, 5 and 7 for $Re_j = 15,000$ at different rpm

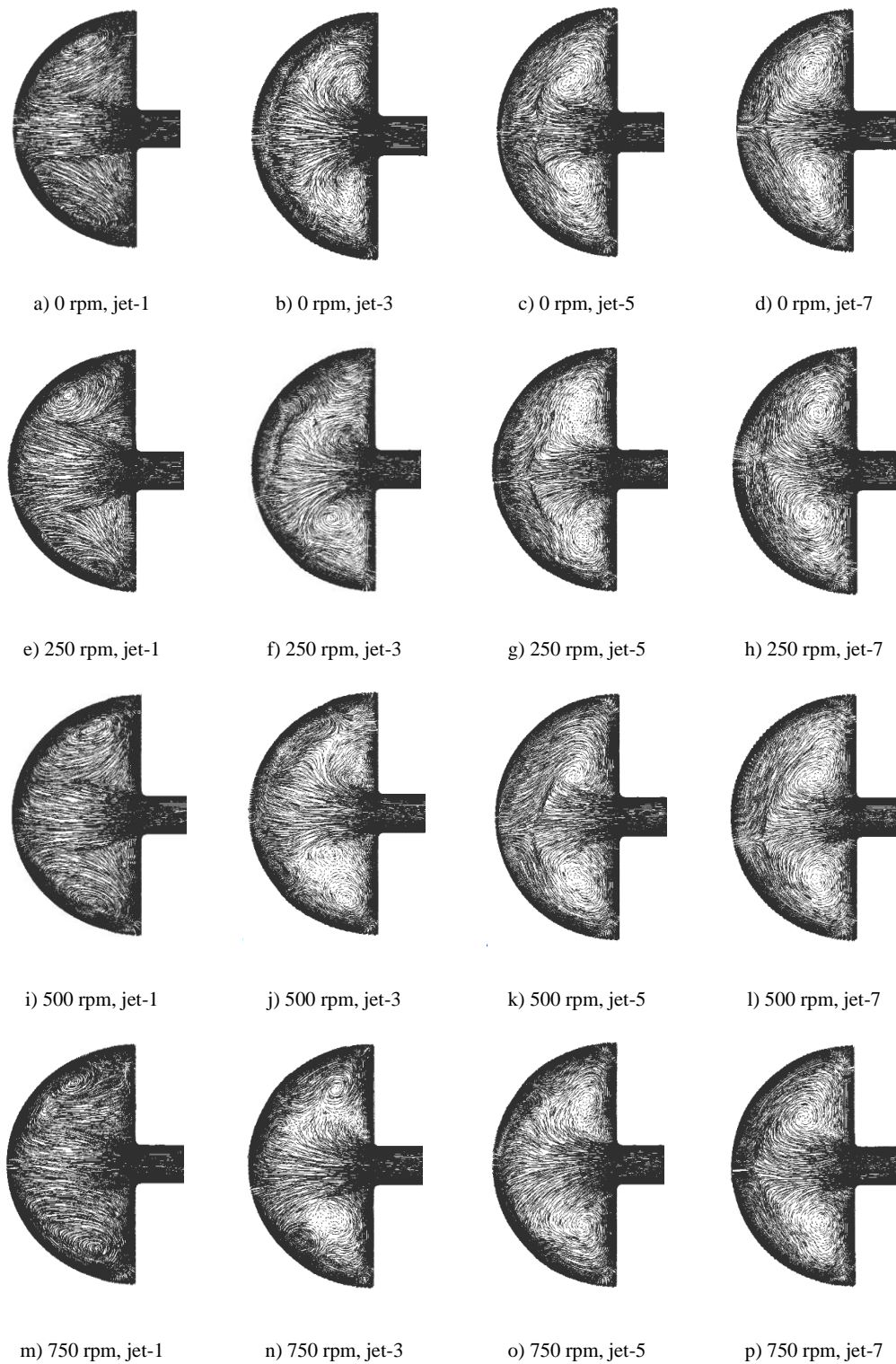


Figure 48: Streamlines on vertical cross section for jet number 1, 3, 5 and 7 for $Re_j = 20,000$ at different rpm

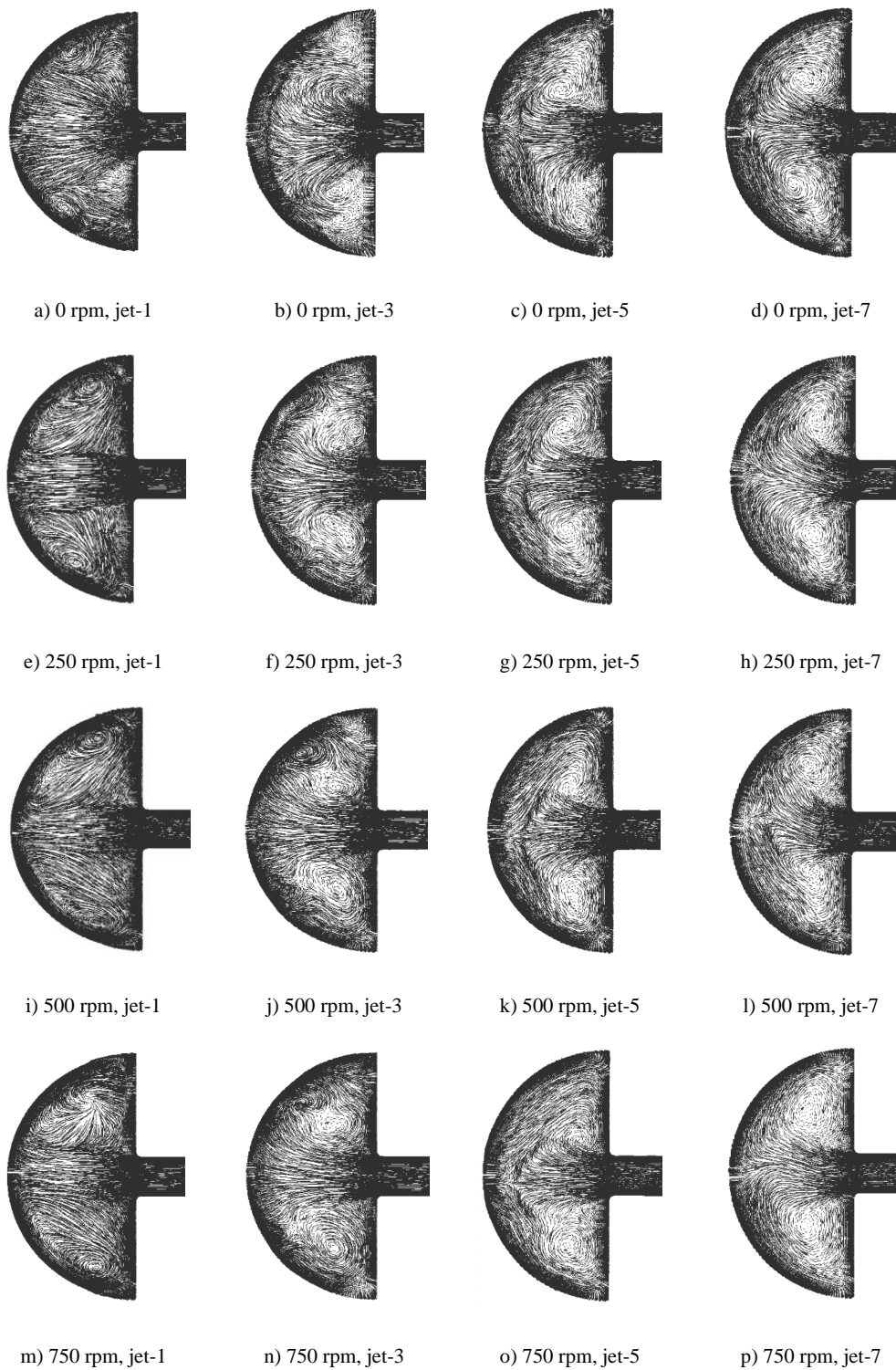


Figure 49: Streamlines on vertical cross section for jet number 1, 3, 5 and 7 for $Re_j = 25,000$ at different rpm

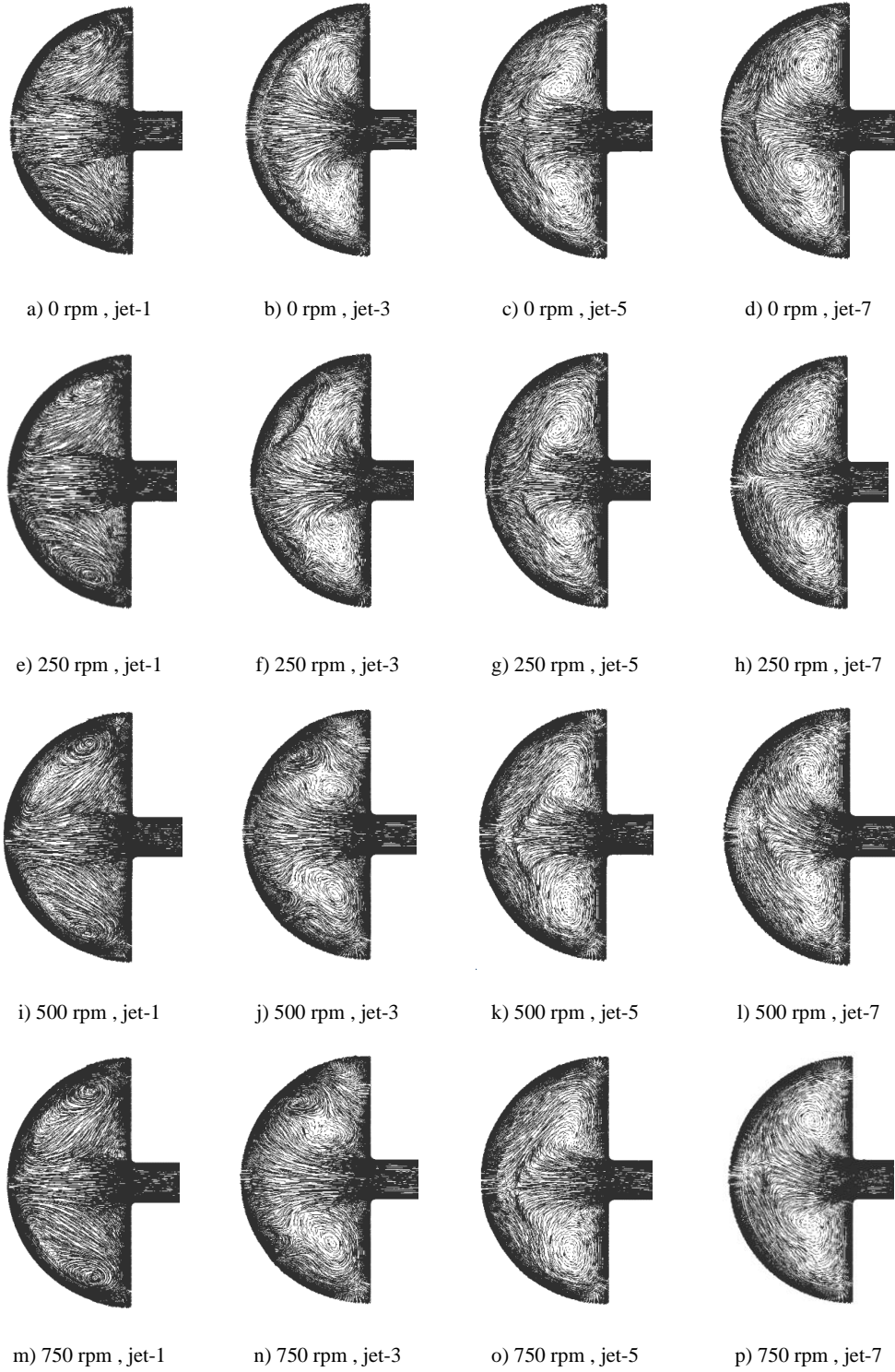
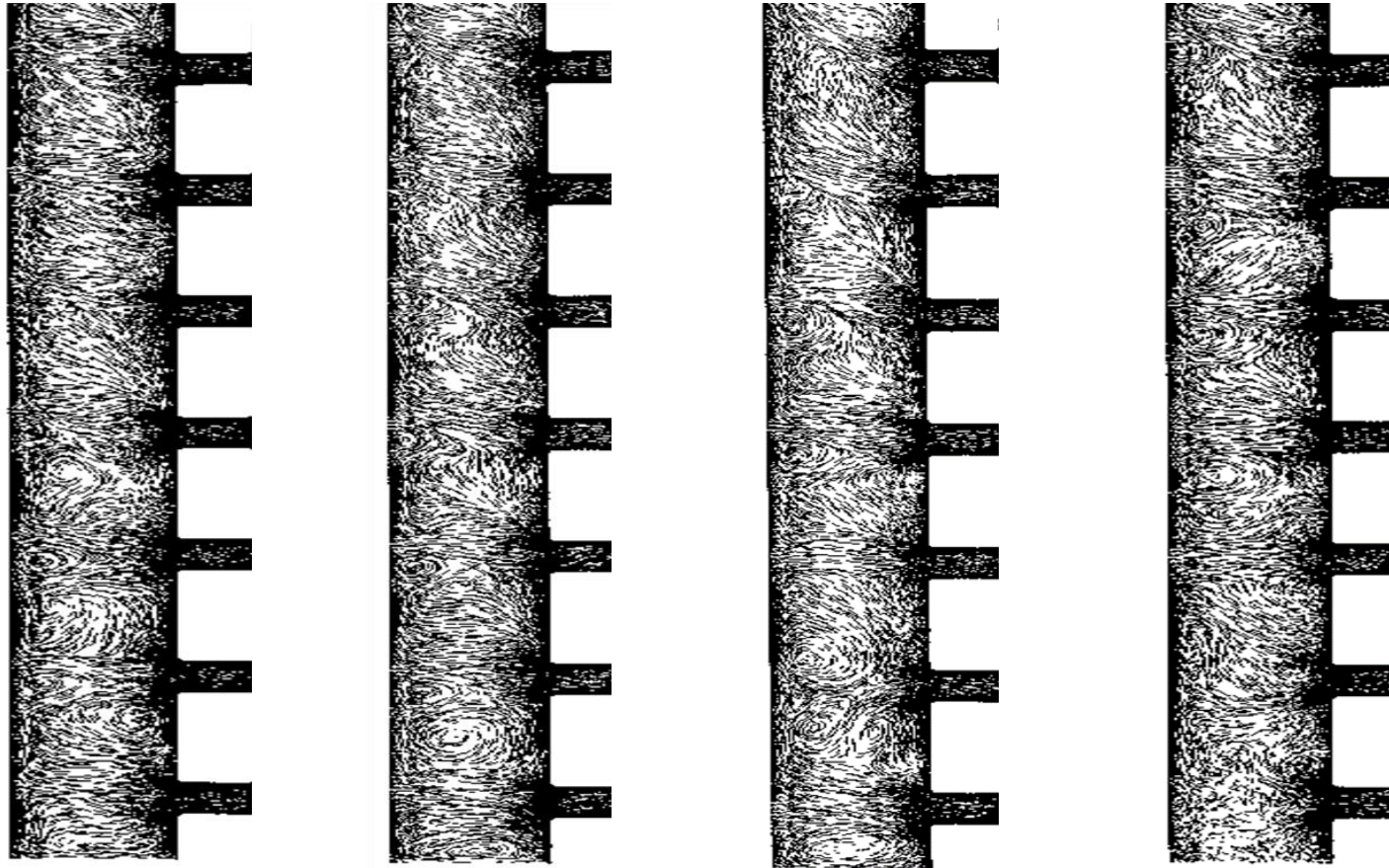


Figure 50: Streamlines on vertical cross section for jet number 1, 3, 5 and 7 for $Re_j = 30,000$ at different rpm

5.2.2 Center Plane Streamlines

Figure 51 to Figure 56 portray the streamlines at a rectangular plane running across the semi-circular channel (plane r-z) and passing through the seven jets. Each figure plots one jet Reynolds number at four rotations. Figure 51(a) illustrates jet impingement shift upward due to the crossflow, as observed in all cases. The effect of rotation and high Reynolds numbers is not apparent in these images because the variation remained minimal.



(a)

(b)

(c)

(d)

Figure 51: Streamlines on center plane for $Re_j = 7,500$ with different rpm, (a) stationary, (b) 250 rpm, (c) 500 rpm, (d) 750 rpm

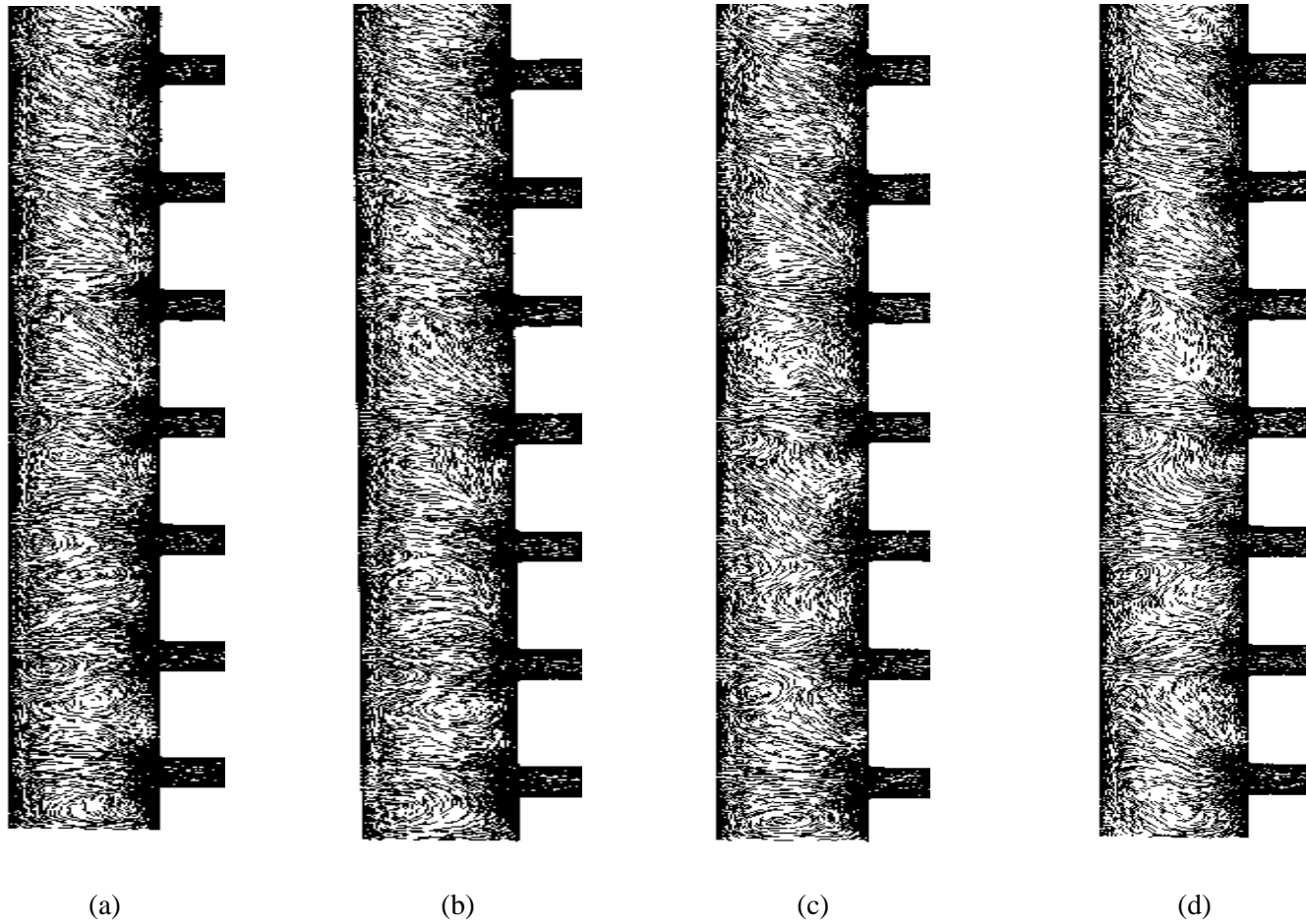


Figure 52: Streamlines on center plane for $Re_j = 10,000$ with different rpm, (a) stationary, (b) 250 rpm, (c) 500 rpm, (d) 750 rpm

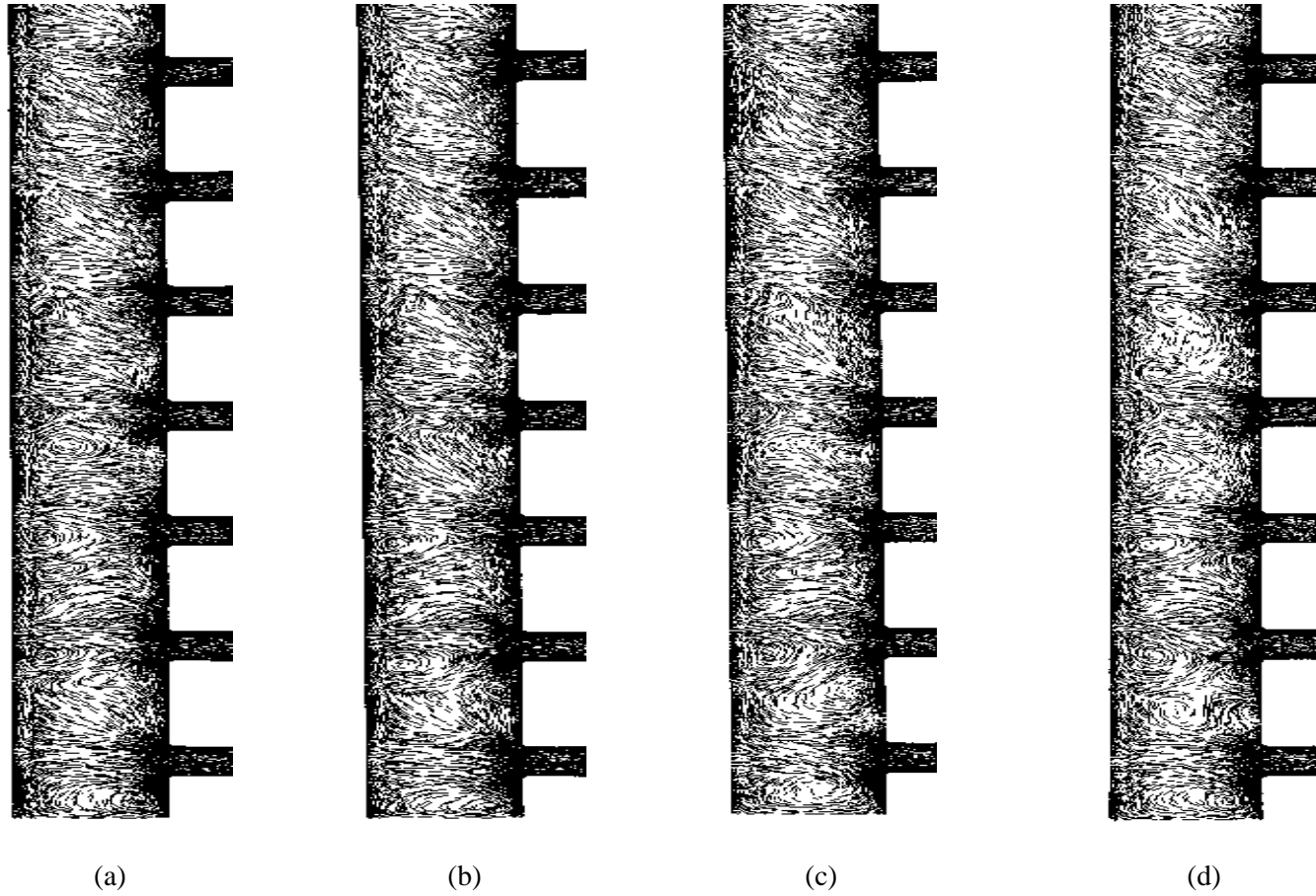


Figure 53: Streamlines on center plane for $Re_j = 15,000$ with different rpm, (a) stationary, (b) 250 rpm, (c) 500 rpm, (d) 750 rpm

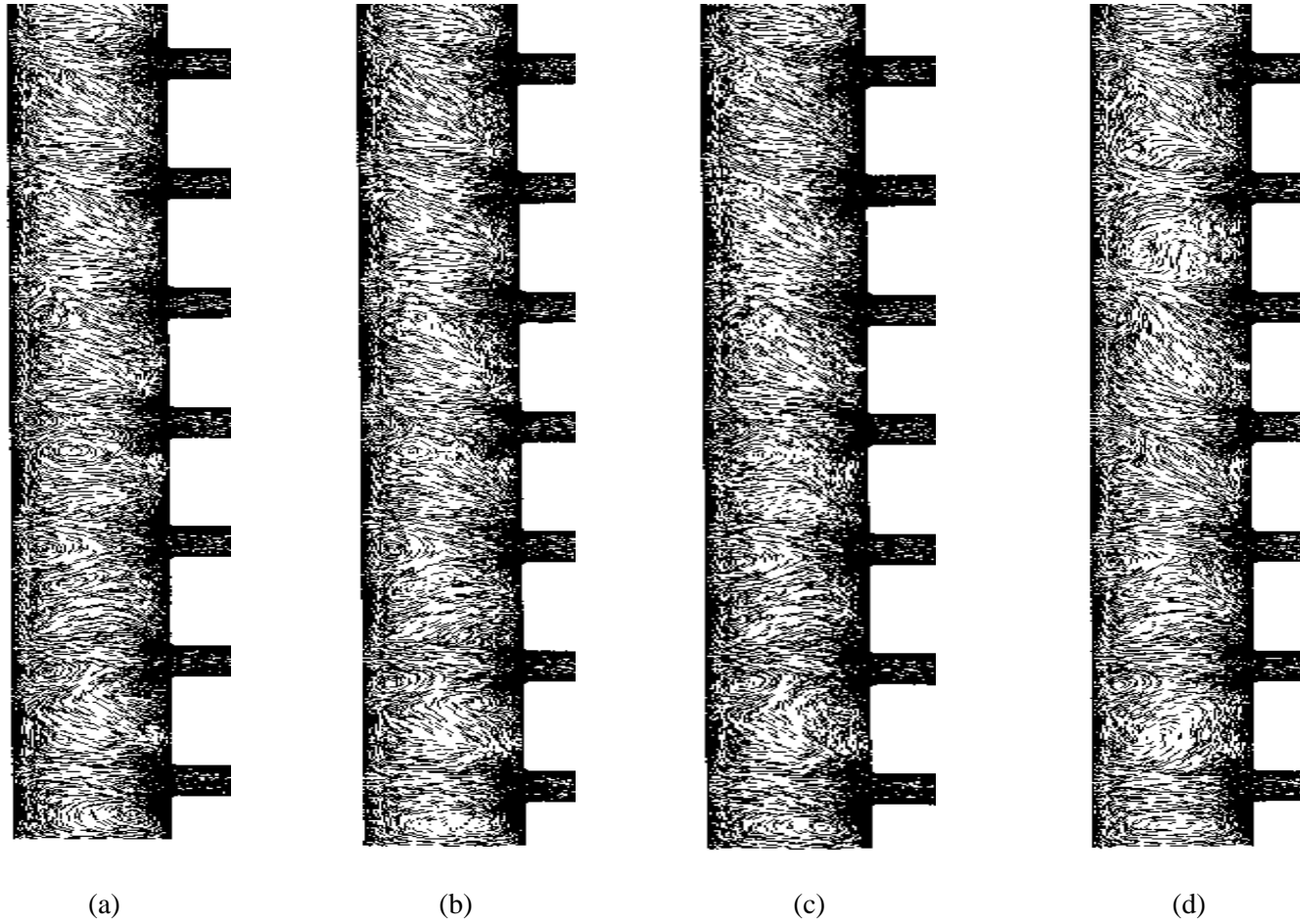


Figure 54: Streamlines on center plane for $Re_j = 20,000$ with different rpm, (a) stationary, (b) 250 rpm, (c) 500 rpm, (d) 750 rpm

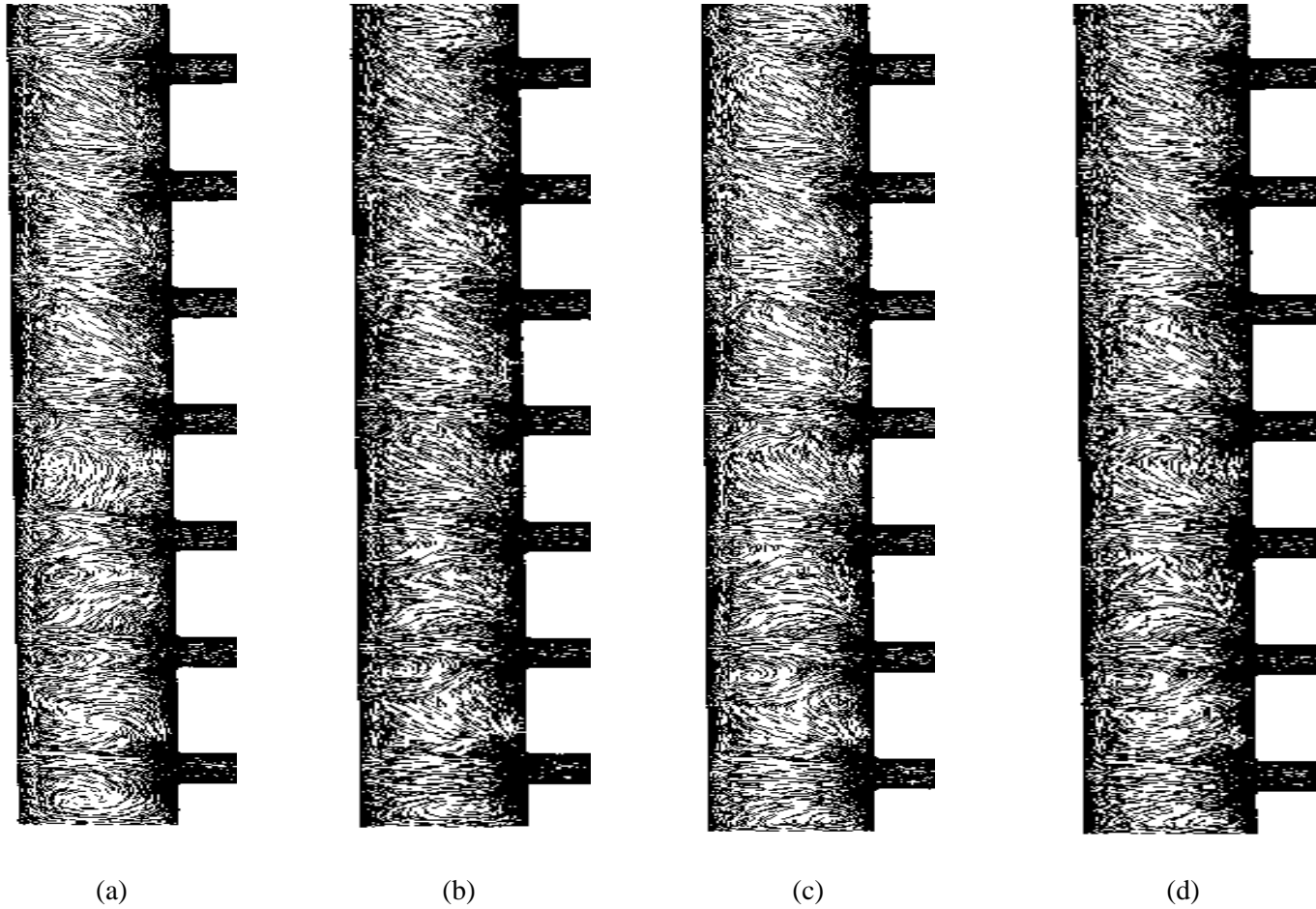


Figure 55: Streamlines on center plane for $Re_j = 25,000$ with different rpm, (a) stationary, (b) 250 rpm, (c) 500 rpm, (d) 750 rpm

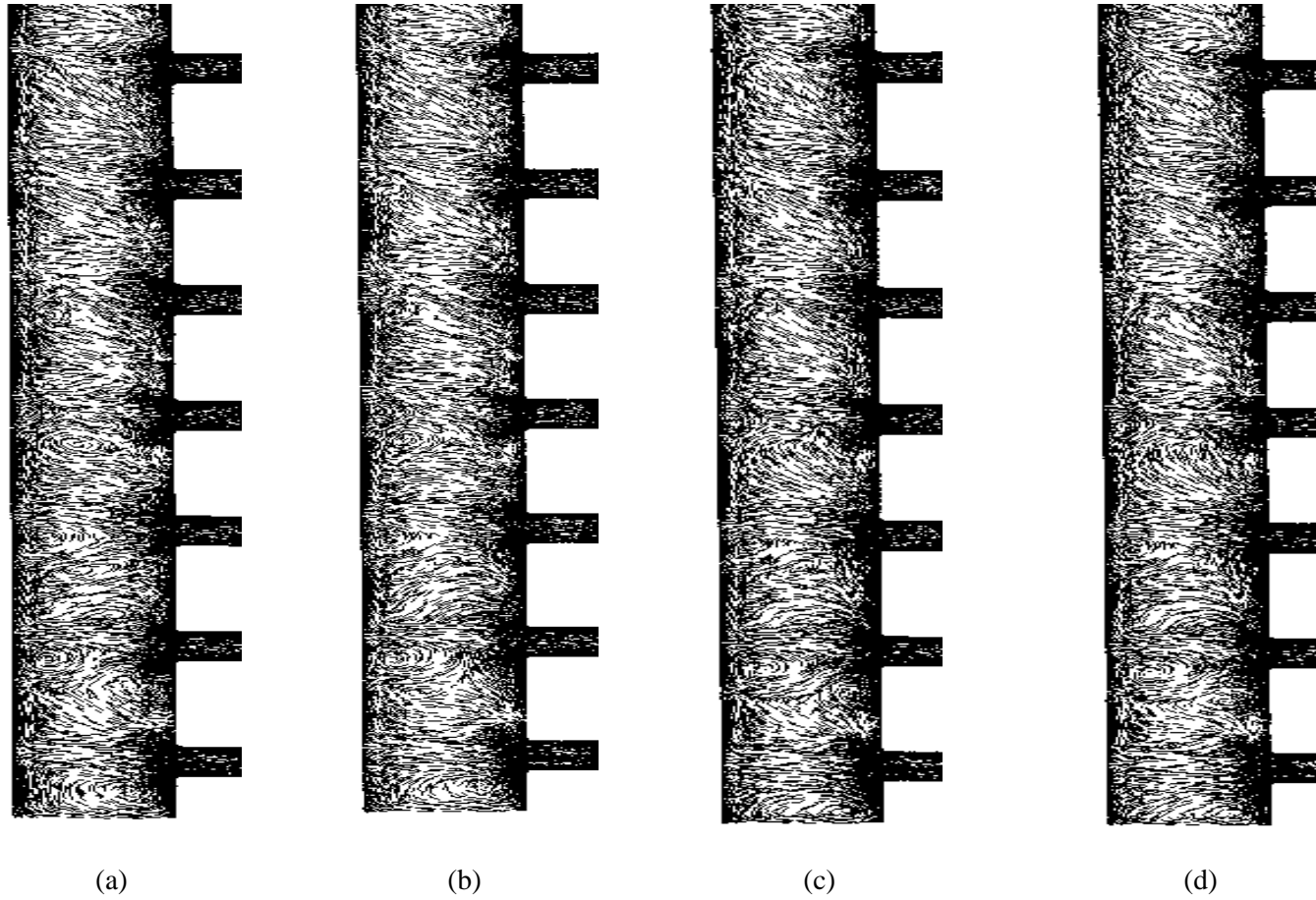


Figure 56: Streamlines on center plane for $Re_j = 30,000$ with different rpm, (a) stationary, (b) 250 rpm, (c) 500 rpm, (d) 750 rpm

5.2.3 Nusselt Number Contour

Figure 57 to Figure 62 show the local Nusselt number contours for all cases. Notably, a proper jet impingement means the jet flow reaches the semi-circular surface, causing proper cooling leading to low temperature and subsequently high local Nusselt number. After examining Figure 57(a), the seven jets' location remains evident when they strike the semi-circle surface. It illustrates a high Nusselt number, indicating high heat transfer. As demonstrated in Figure 57, as angular speed increased from 0 to 750 rpm, the radial flow increases, promoting crossflow and pushing the jet flow to start impinging downstream (in a radial direction). Figure 57(d) depicts five localized cooling regions out of seven regions, as expected. Only five localized cooling spots reached 750 rpm, because the centrifugal force dominated the flow structure, pushing the jet flow upward. Hence, less mass fraction moved through jets one and two, generating weak jet flow. However, as the jet Reynolds number increased (Figure 62(d)), the jet flow inertia substantially grew, ensuring proper impingement. Thus, the seven jet locations are marked. Due to the Coriolis force, the rotation shifted impingement to the sides at high rpm, as shown in Figure 57(b-d). In these figures, the flow lost its symmetry around the vertical axis at 0 rpm (Figure 57a). The pick of the local Nusselt number shifted to the sides due to the deflected jet impingement created by the rotation. At a high jet Reynold number, angular speed diminished, and jet inertia dominated the flow structure. Consequently, a widespread contour for the seven jets is observed in Figure 62. The local Nusselt number for each jet has its minimum displacement at a high jet Reynolds number at any rotation. Given the heat flux remained constant for all cases, higher the jet Reynolds number, the higher the Nusselt

number for all cases. Also, the Nusselt number distribution remained more uniform at higher Reynolds number.

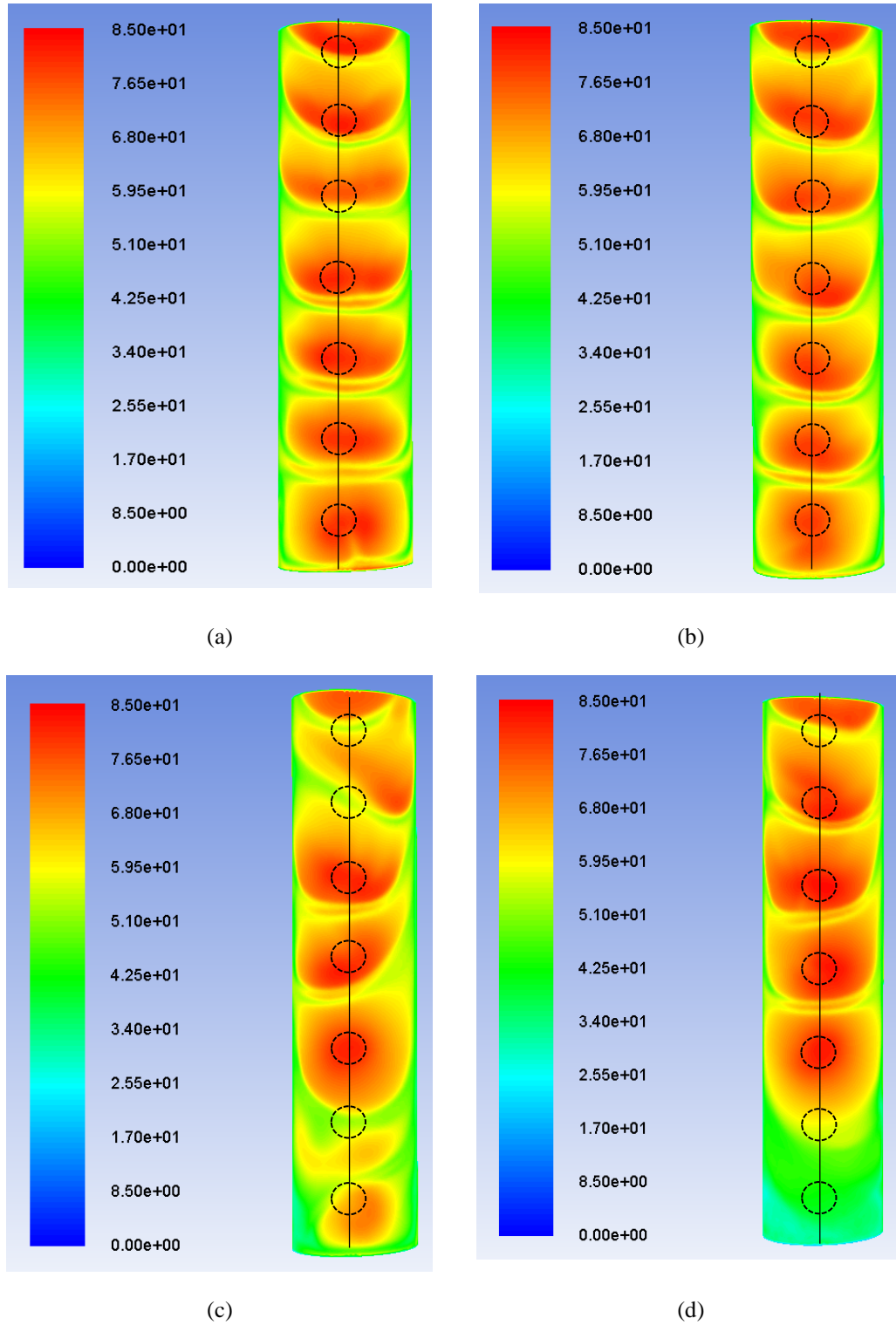


Figure 57: Nusselt number contours on the curved surface for Re_j of 7,500 with different rotation, (a) stationary, (b) 250 rpm, (c) 500 rpm and (d) 750 rpm

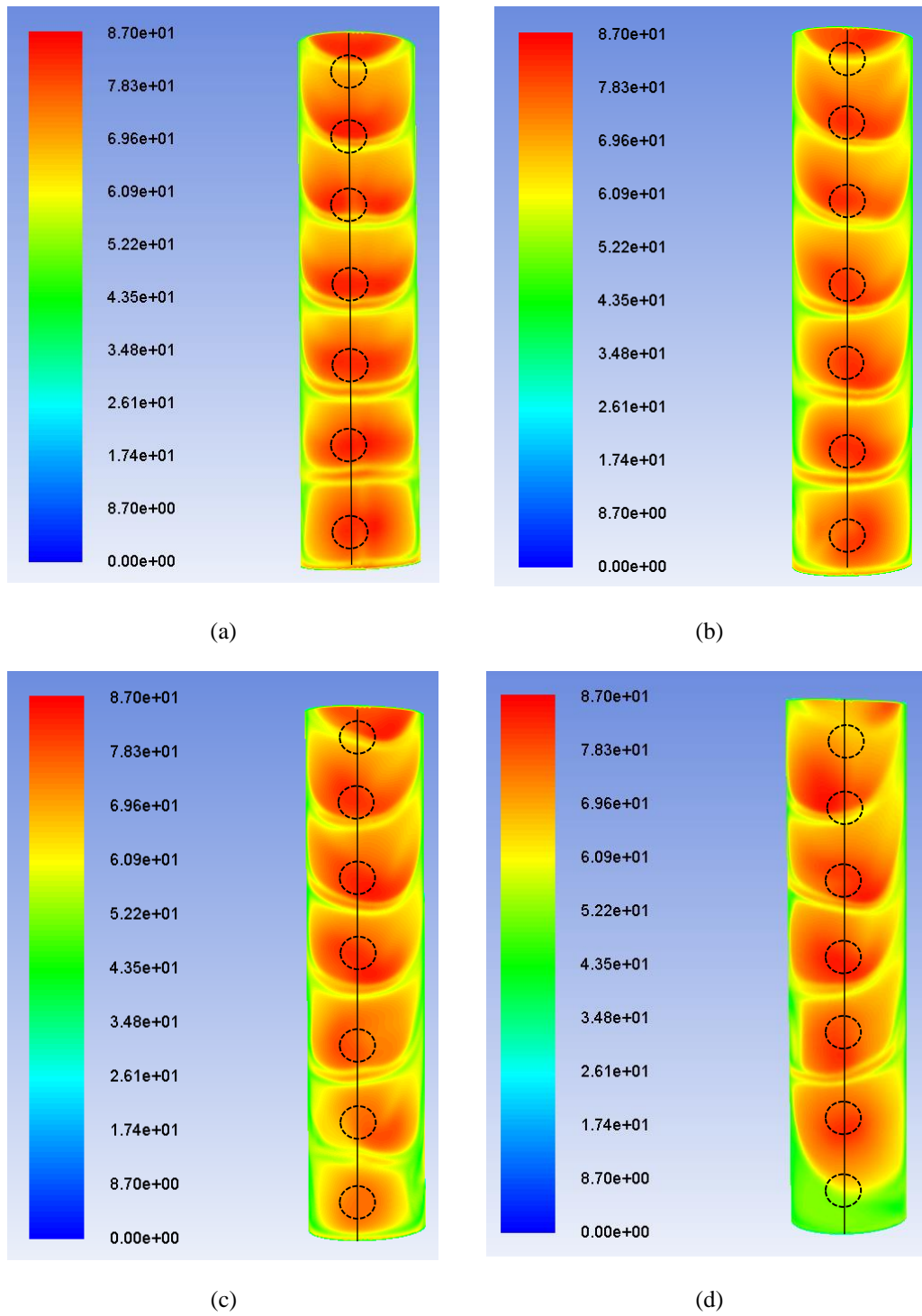


Figure 58: Nusselt number contours on the curved surface for Re_j of 10,000 with different rotation, (a) stationary, (b) 250 rpm, (c) 500 rpm and (d) 750 rpm

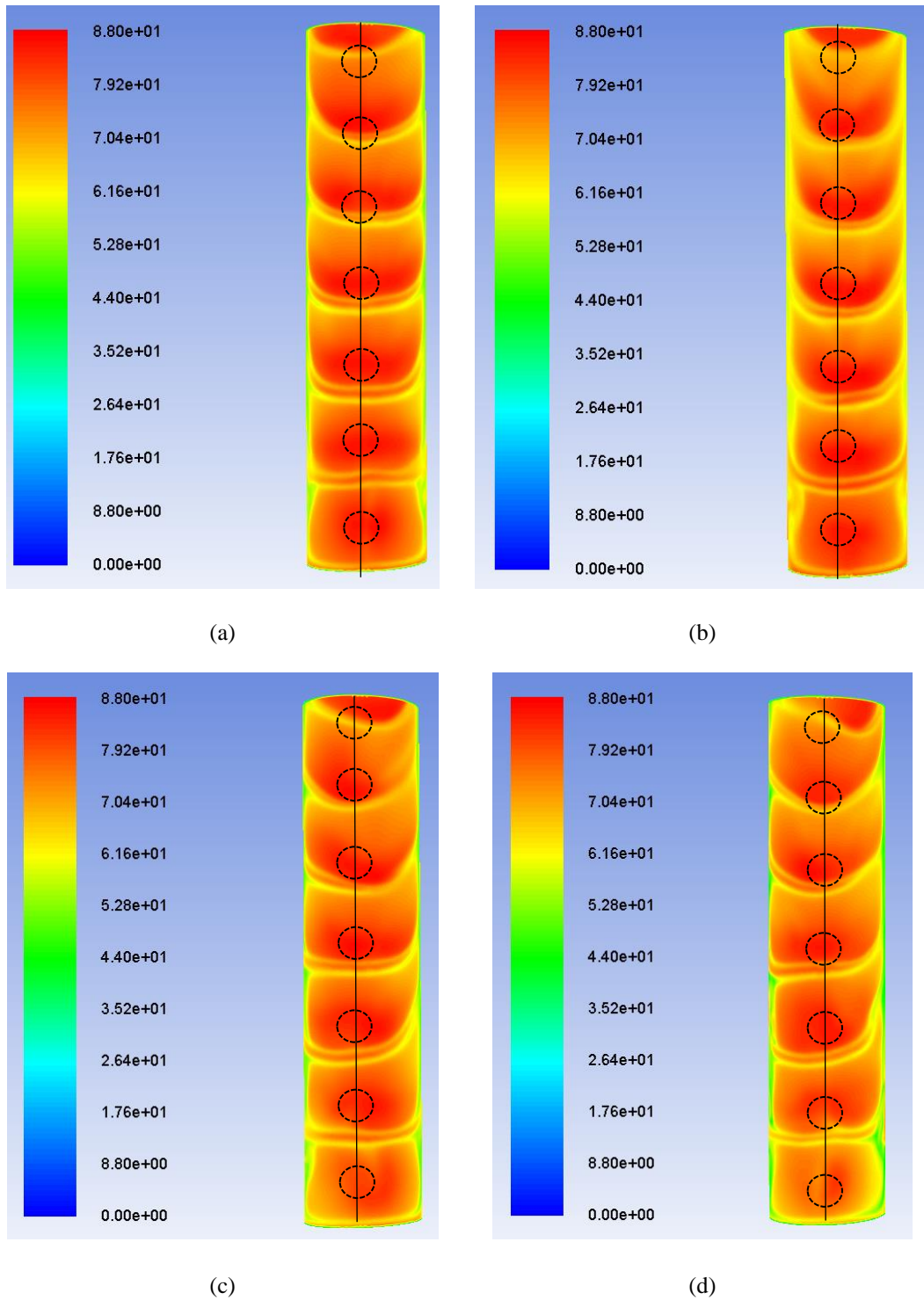
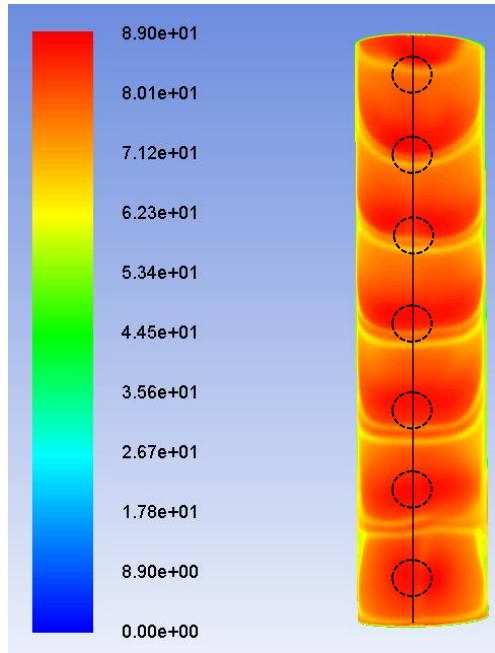
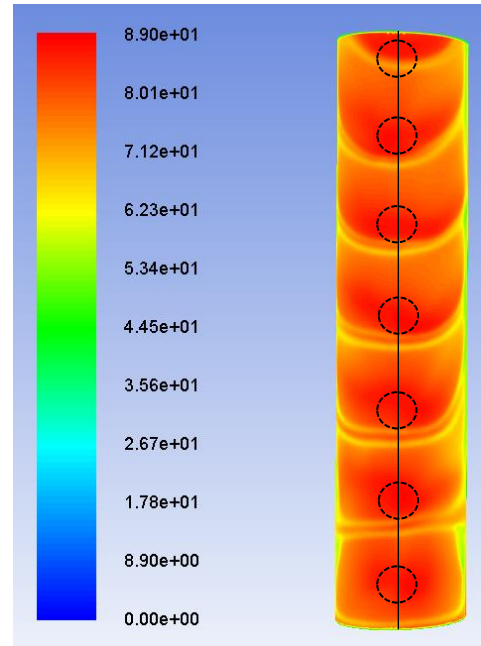


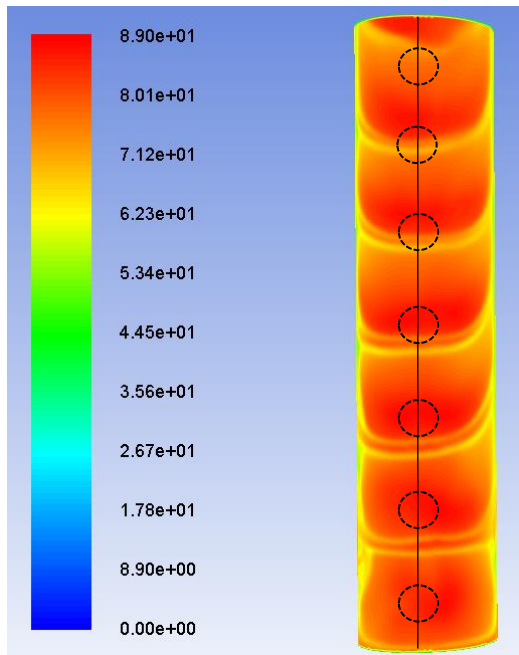
Figure 59: Nusselt number contours on the curved surface for Re_j of 15,000 with different rotation, (a) stationary, (b) 250 rpm, (c) 500 rpm and (d) 750 rpm



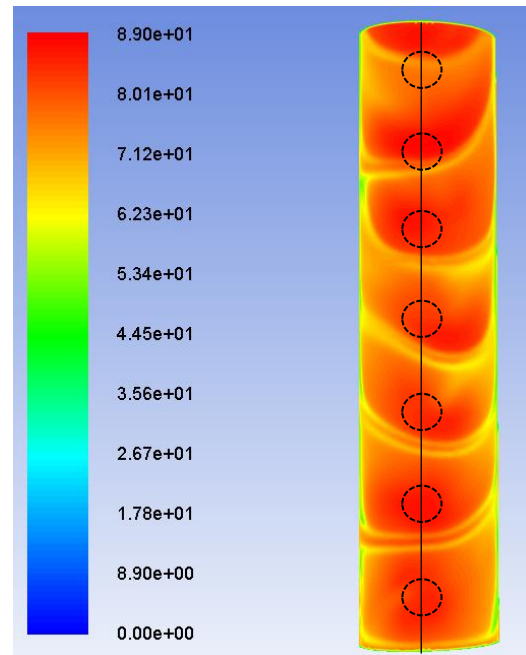
(a)



(b)



(c)



(d)

Figure 60: Nusselt number contours on the curved surface for Re_j of 20,000 with different rotation, (a) stationary, (b) 250 rpm, (c) 500 rpm and (d) 750 rpm

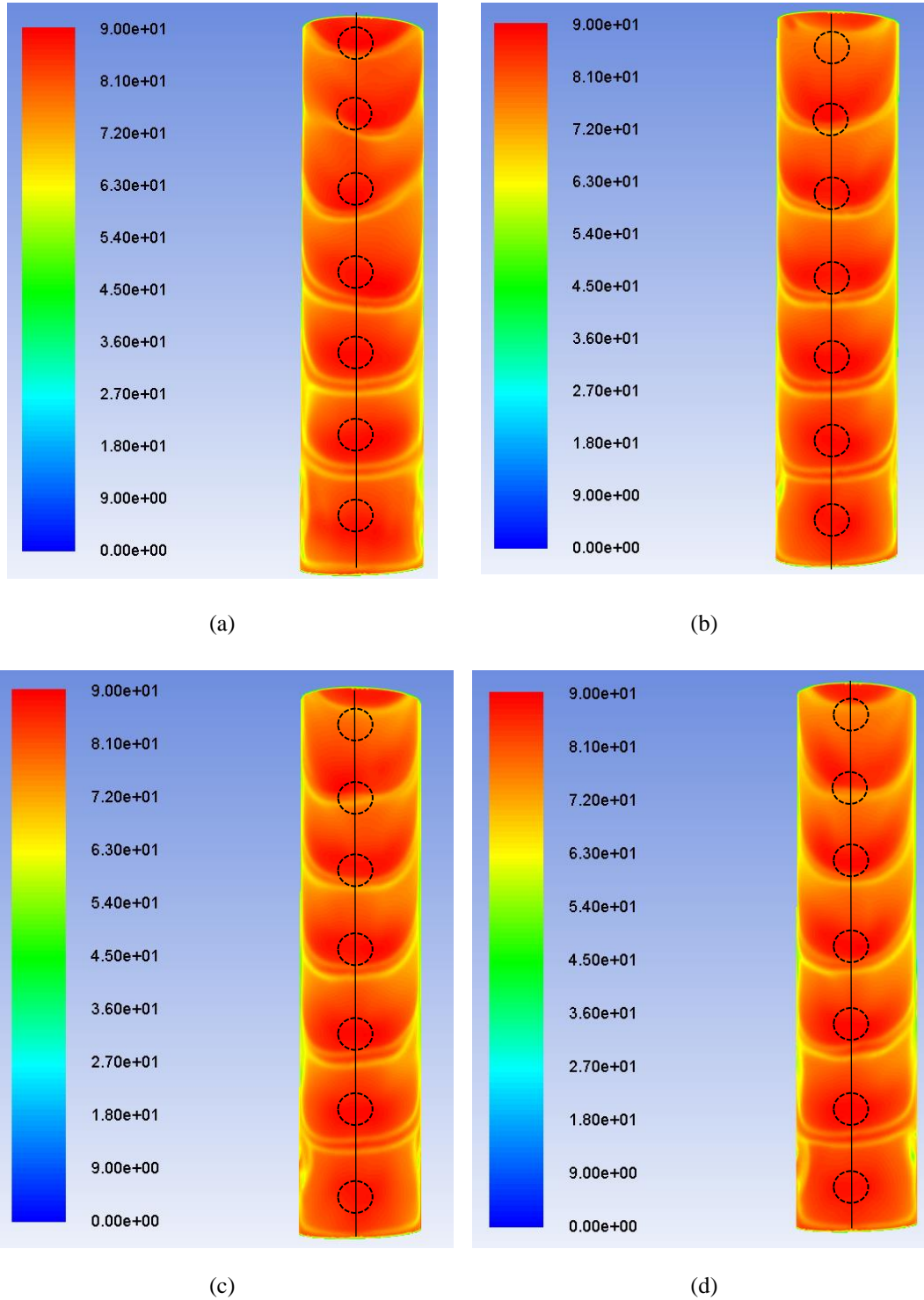


Figure 61: Nusselt number contours on the curved surface for Re_j of 25,000 with different rotation, (a) stationary, (b) 250 rpm, (c) 500 rpm and (d) 750 rpm

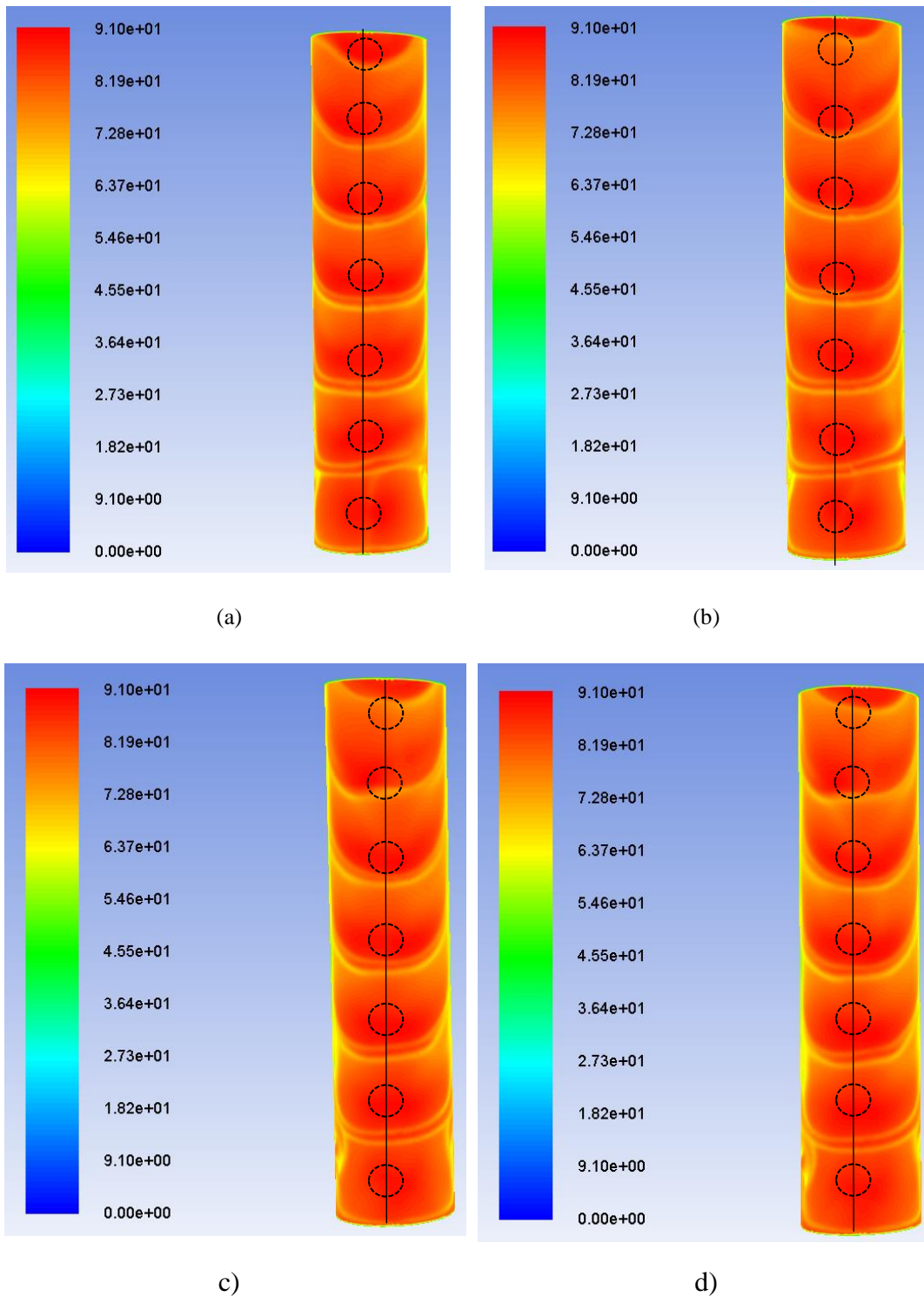
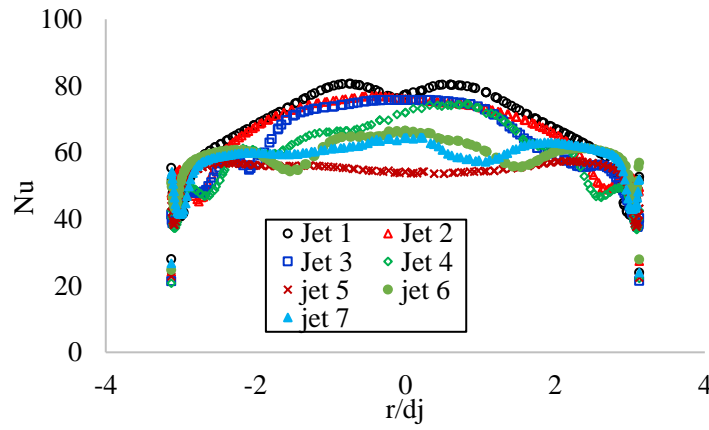


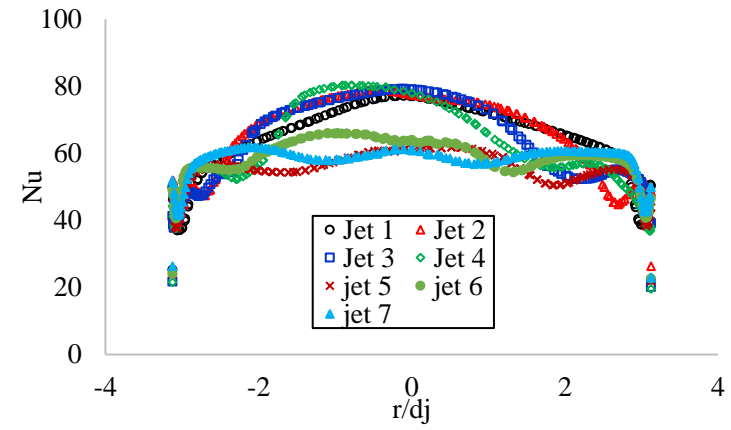
Figure 62: Nusselt number contours on the curved surface for Re_j of 30,000 with different rotation, (a) stationary, (b) 250 rpm, (c) 500 rpm and (d) 750 rpm

5.2.4 Nusselt Number Distribution on the Curved Line Facing Each Jet

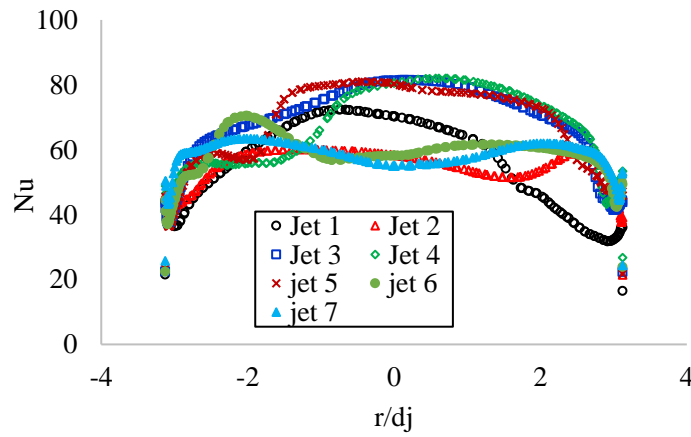
The localized Nusselt number on the semi-circular curve line facing each jet is plotted around the curved line in Figure 63 to Figure 68 for all jet Reynolds numbers from 7,500-3,0000. For Figure 63, at $Re_j = 7,500$, jet one had a wide Nusselt number between maximum and minimum values due to the substantial impingement and crossflow absence. Figure 63 revealed a big difference between each jet performance, clearly depicting crossflow on low jet Reynolds numbers. At higher jet Reynolds numbers, such as Figure 68, the Nusselt number distribution from each jet shows less discrepancy, displaying overall Nusselt number uniformity. The impact of a ratio on local Nusselt number at a low Re_j ($Re_j = 7,500$, Figure 63) emerges. When comparing Figure 63a (0 rpm) and Figure 63d (750 rpm), the first jet's cooling dropped dramatically due to the mass fraction decrease. The mass fraction drop with high rpm resulting from centrifugal force moving the fluid radially, reducing the fluid amount delivered to jet one. The centrifugal force impacted the secondary channel carrying the cooling fluid, as presented in this figure. The secondary channel is shown in Figure 10. Generally, rotation destroys the uniformity of impingement jets at low Reynolds numbers due to the changing mass fraction and the jet deflection. The rotation effect diminishes at high Reynolds numbers and is almost absent in Figure 68. At high Reynolds numbers, the Nusselt number distribution along the curved line remained uniform. Conversely, at low Reynolds numbers, the Nusselt number remains less uniform. A high Reynolds number means higher inertia dominated compared to the given angular speed.



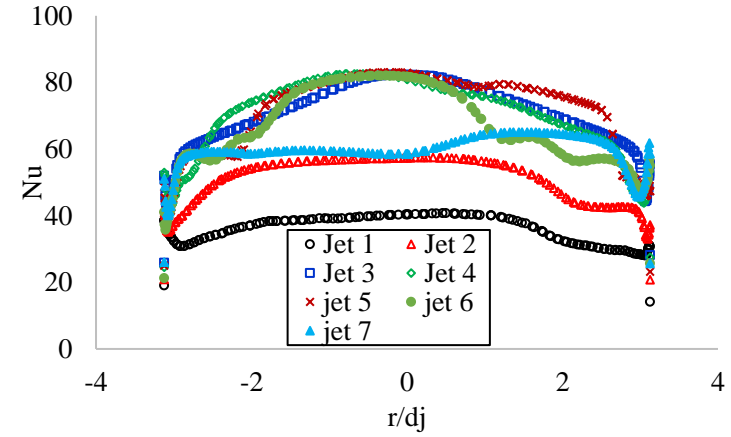
(a)



(b)

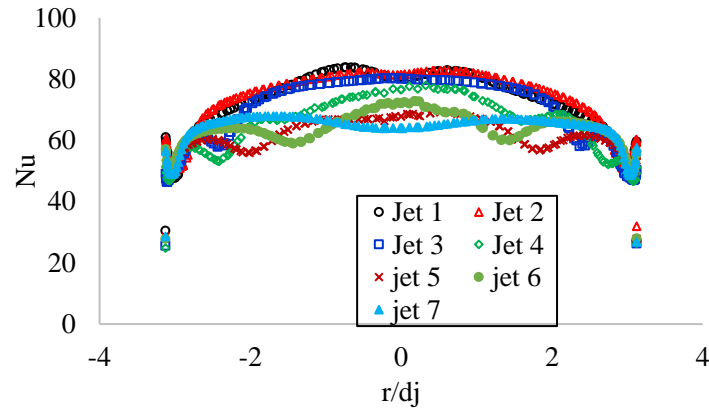


(c)

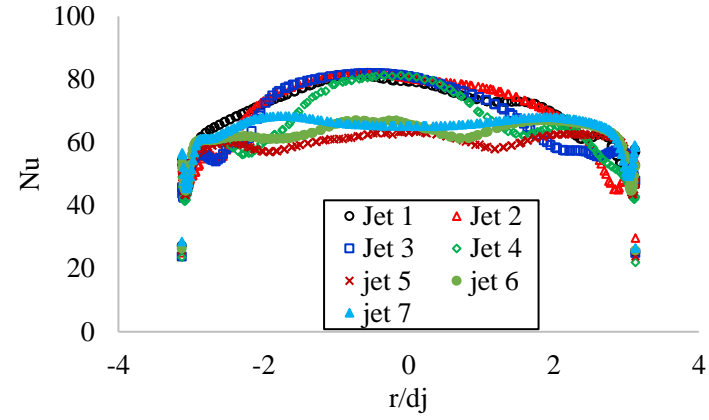


(d)

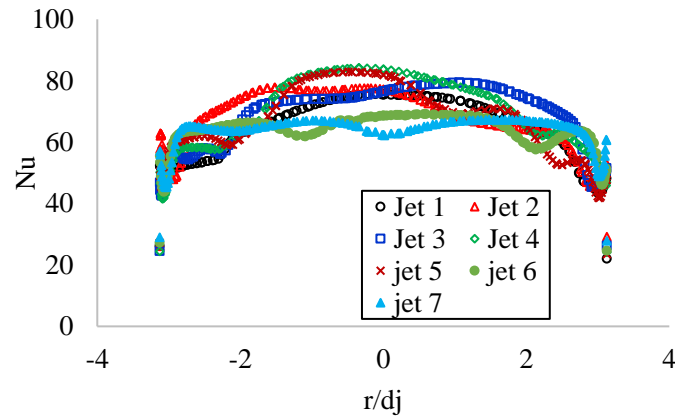
Figure 63: Local Nusselt number on the curved line facing each jet for $Re_j = 7,500$, (a) stationary, (b) 250 rpm, (c) 500 rpm, (d) 750 rpm



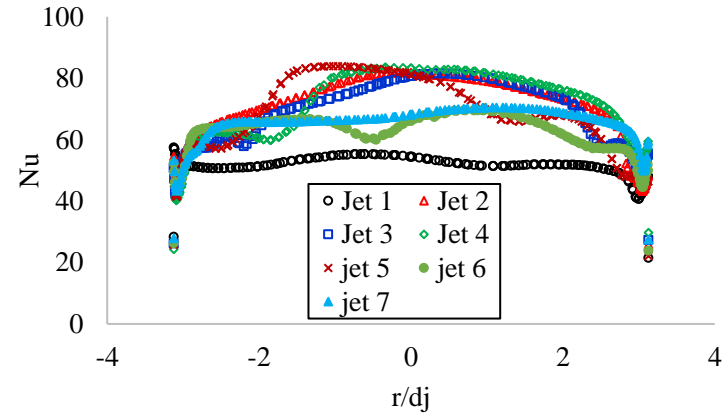
(a)



(b)

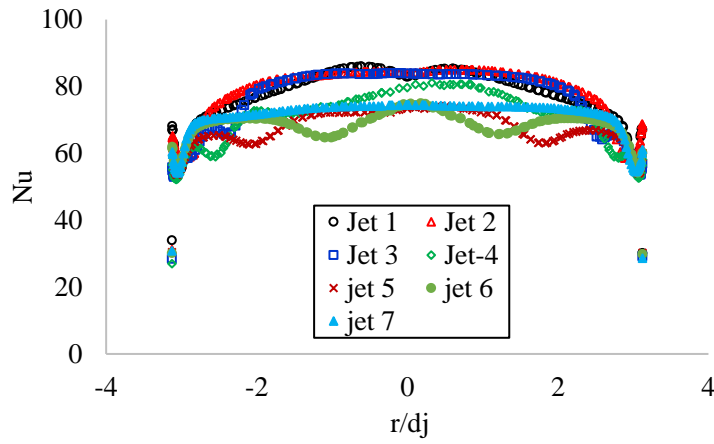


(c)

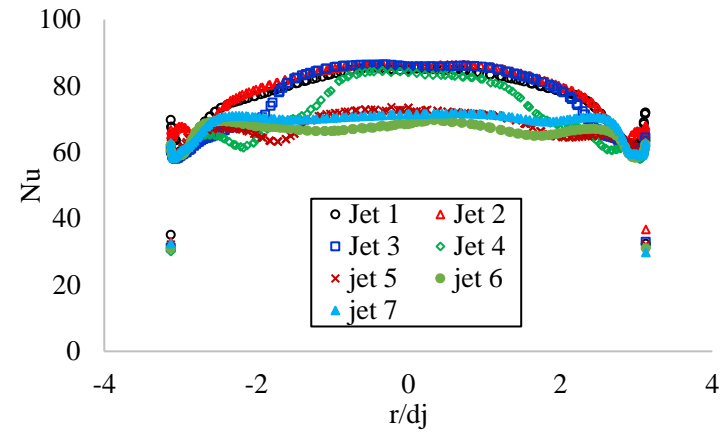


(d)

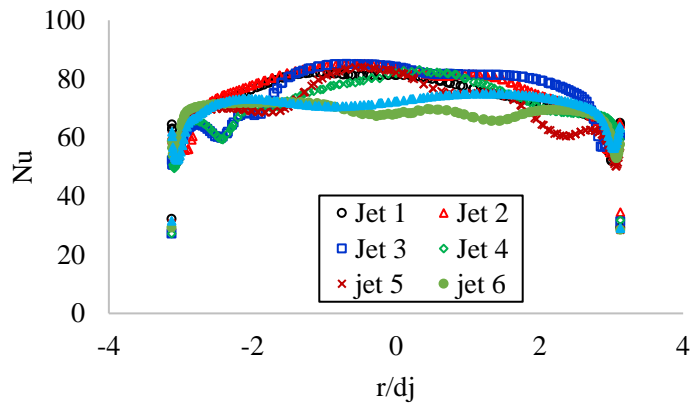
Figure 64: Local Nusselt number on the curved line facing each jet for $Re_j = 10,000$, (a) stationary, (b) 250 rpm, (c) 500 rpm, (d) 750 rpm



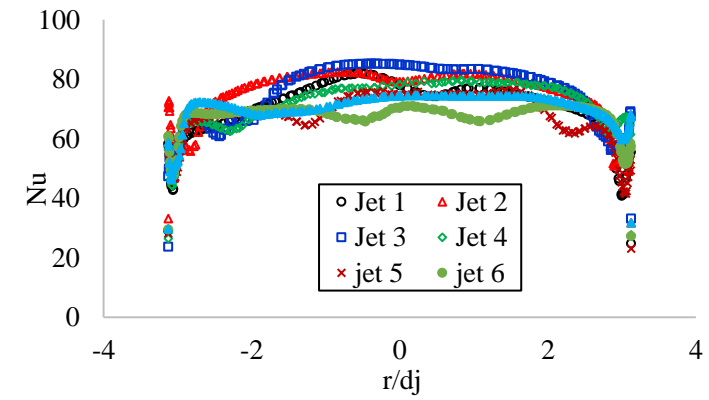
(a)



(b)

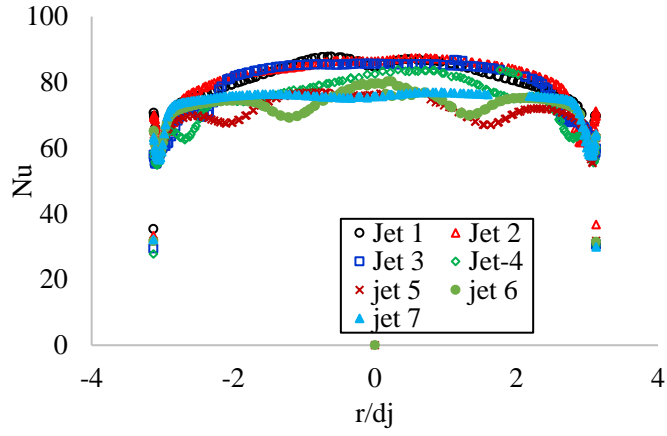


(c)

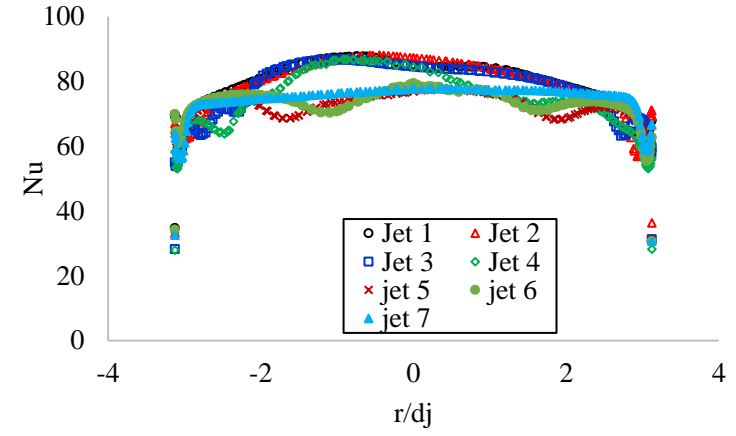


(d)

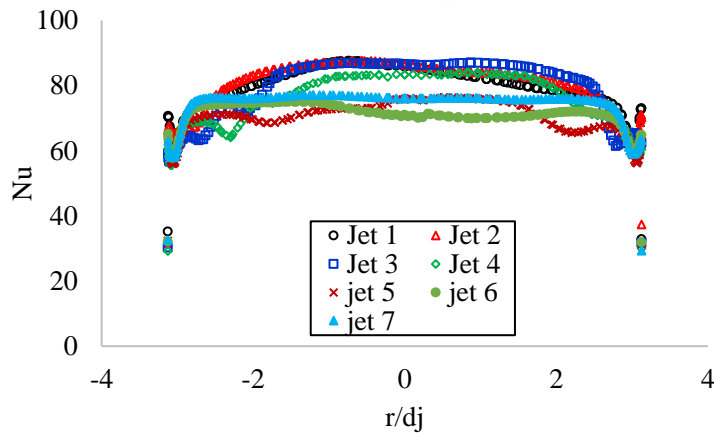
Figure 65: Local Nusselt number on the curved line facing each jet for $Re_j = 15,000$, (a) stationary, (b) 250 rpm, (c) 500 rpm, (d) 750 rpm



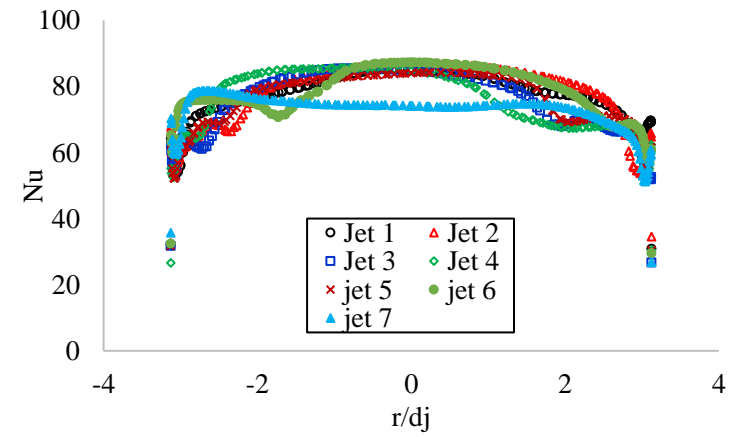
(a)



(b)

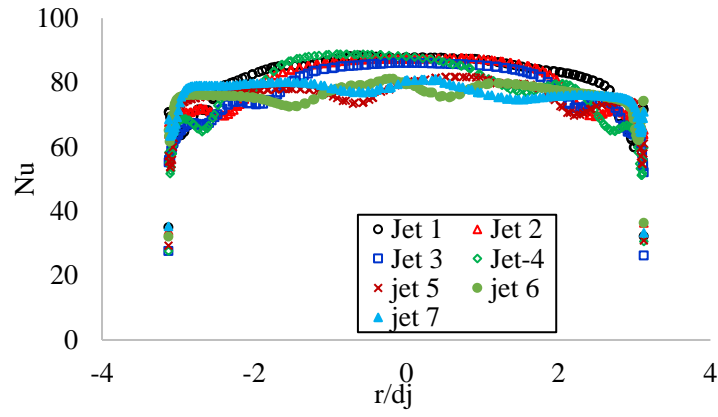


(c)

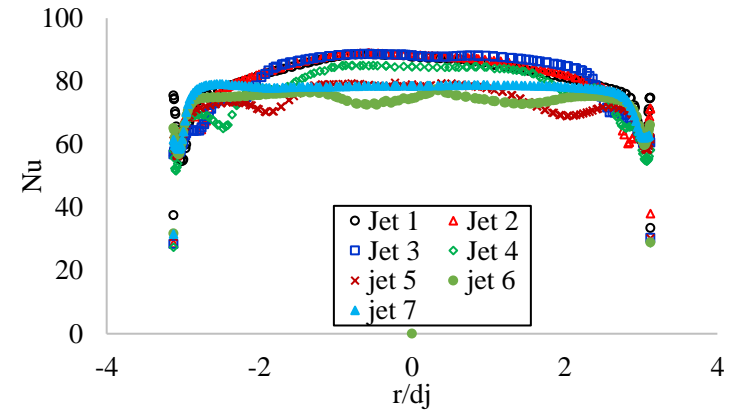


(d)

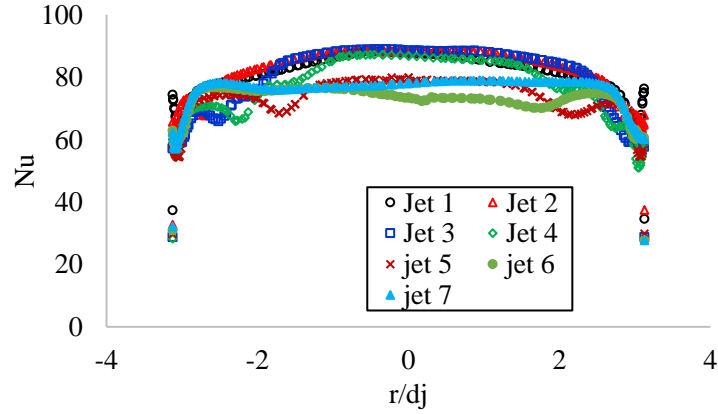
Figure 66: Local Nusselt number on the curved line facing each jet for $Re_j = 20,000$, (a) stationary, (b) 250 rpm, (c) 500 rpm, (d) 750 rpm



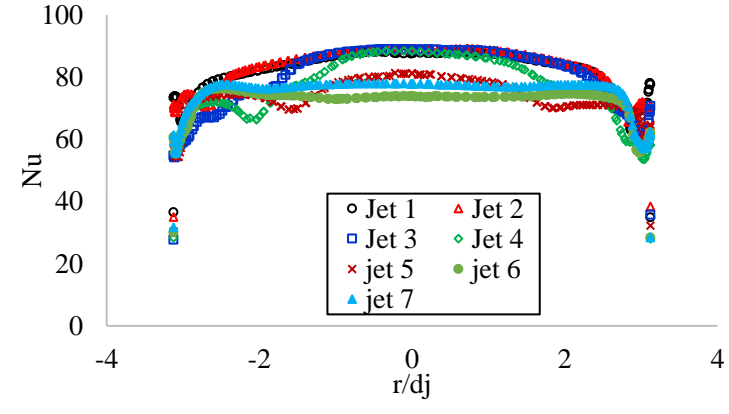
(a)



(b)

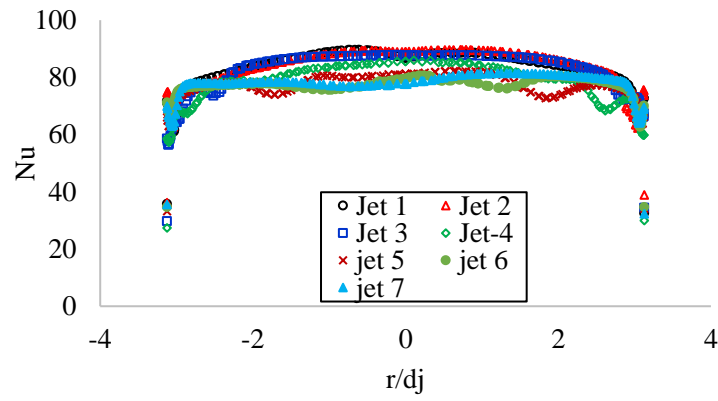


(c)

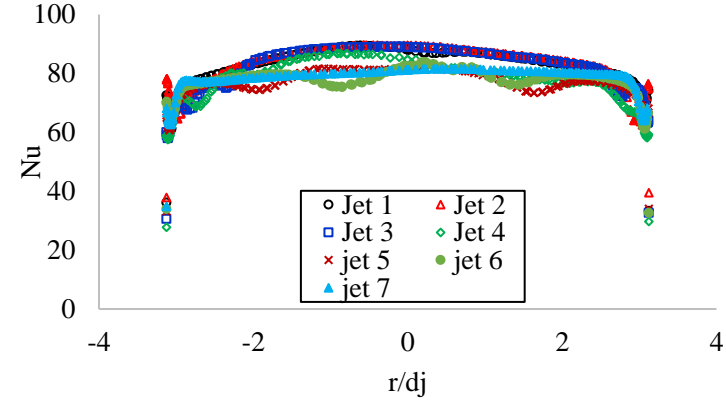


(d)

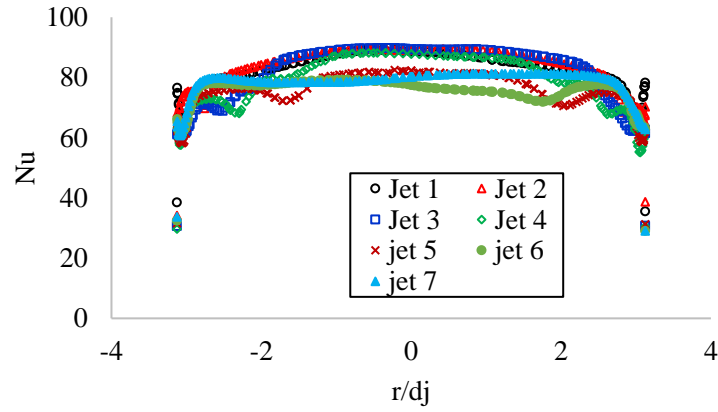
Figure 67: Local Nusselt number on the curved line facing each jet for $Re_j = 25,000$, (a) stationary, (b) 250 rpm, (c) 500 rpm, (d) 750 rpm



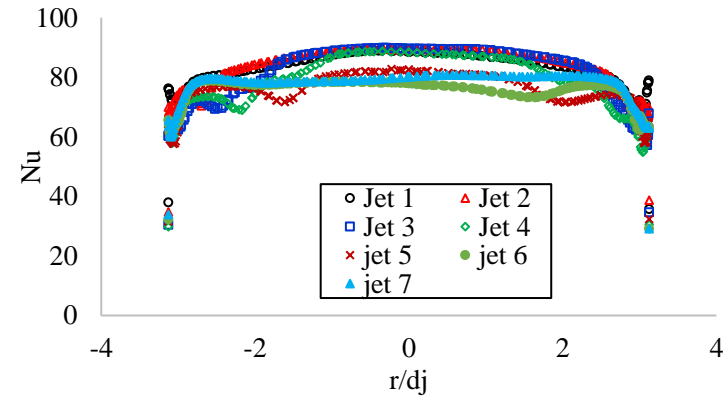
(a)



(b)



(c)



(d)

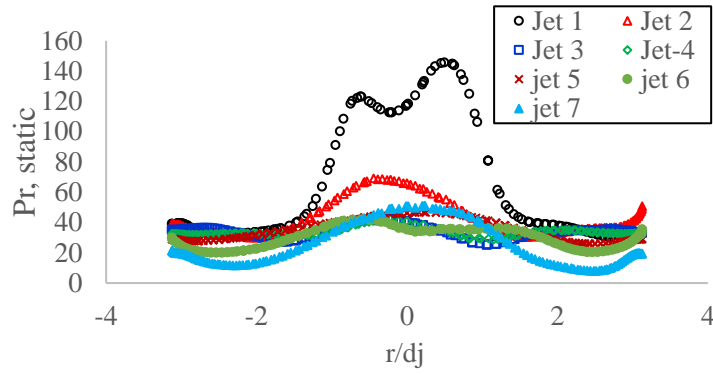
Figure 68: Local Nusselt number on the curved line facing each jet for $Re_j = 30,000$, (a) stationary, (b) 250 rpm, (c) 500 rpm, (d) 750 rpm

5.2.5 Static Pressure Distribution on the Curved Line Facing Each Jet

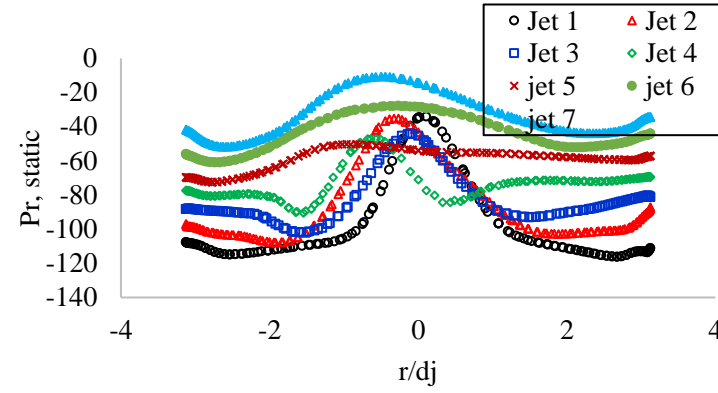
The static pressure on the curved lines facing each jet is plotted in Figure 69 to Figure 74 for jet Reynolds numbers 7,500 to 30,000. At low Reynolds number ($Re_j = 7,500$) as shown in Figure 69, rotation significantly affects the local static pressure distribution formed by each jet. As demonstrated in the figures, rotation reduced static pressure, destroying jet impingement. The pressure distribution along the curved line remained uniform for high rpm and at low Reynolds numbers unveiling the absence of impingement on the curved surface.

Moreover, it reduced overall static pressure for the low jets at high rpm, where jets one and two experienced minimum static pressure. In the Nusselt number distribution contour for jet Reynold number 7,500 and high rpm, the local Nusselt number is absent for the first jet and very poor for the second jet. The streamlines section for jets one and two, for the same conditions ($Re_j = 7500$ and higher rpm) revealed poor impingement due to the centrifugal force and low mass fraction through jets one and two. As shown in Figure 69a, when focusing on one jet (for example, jet one), maximum static pressure occurred around the center where the jet impinged on the curved wall, while far from the impingement zone pressure had reduced. The crossflow on jet impingement is clearly shown in Figure 69 to Figure 74. Given the crossflow breaks and shifts impingement, it reduces the local pressure for upper jets. The static pressure drops as angular speed increases, portrayed when comparing Figure 69(a-d). The static pressure fell with increased angular speed as expected because angular speed increases the centrifugal force, pushing and forcing the flow toward the exit. Crossflow and rotational speed cause the flow to shift away from the perpendicular area facing the jet, diminishing its impact on the curved surface.

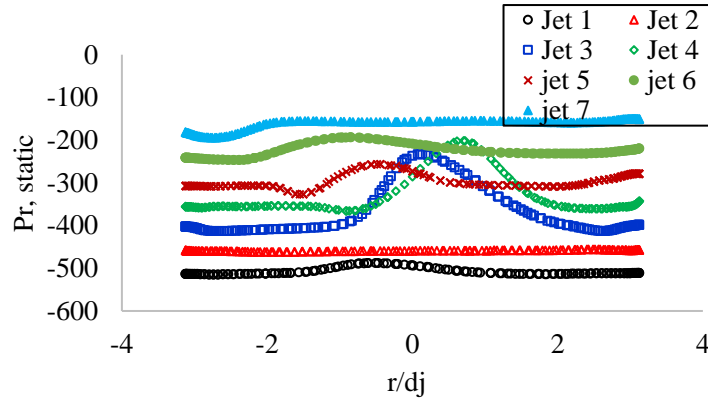
Similar trends are shown in other Reynolds numbers in Figure 70 to Figure 74. From Figure 69a to Figure 74a, for stationary conditions, the maximum static pressure occurred around the center. Chiefly, jets one and two had the highest static pressure at the Reynolds number stationary condition. The reason for having the highest static pressure for jet one involves crossflow absence, while the second jet is exposed to the minimum crossflow coming from the first jet only. At high Reynolds numbers, such as Figure 74, the rotation lead a minimum influence on static pressure for upper jets (jets six and seven), while for lower jets (jets one and two), it behaved similarl to stationary conditions. Also, by comparing Figure 69 to Figure 74, maximum static pressure increased as jet Reynolds number increased. The crossflow exists at stationary conditions for all Reynolds numbers. Crossflow did not impact jet one, which is located at the beginning of the axial flow. Thus, it has maximum static pressure at the stationary condition (Figure 69a-Figure 74a). Figure 69d illustrates the highest rotational effect on static pressure at $Re_j = 7,500$. Generally, high rpm reduces impingement on the target surface, lowering cooling. Figure 69 to Figure 74 portray centrifugal force dominated the flow structure at a high rpm, leading to low jet impingement cooling.



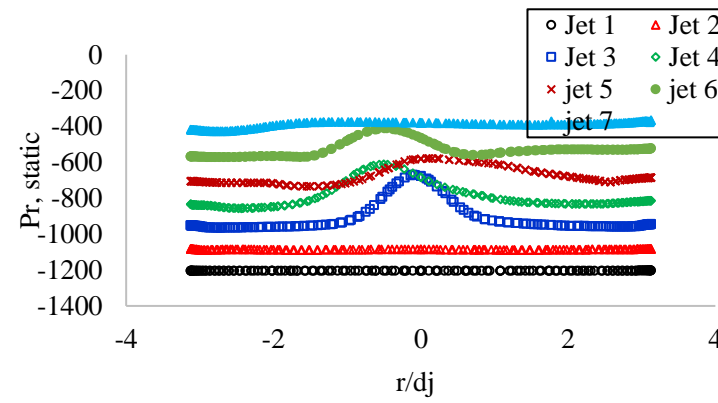
(a)



(b)

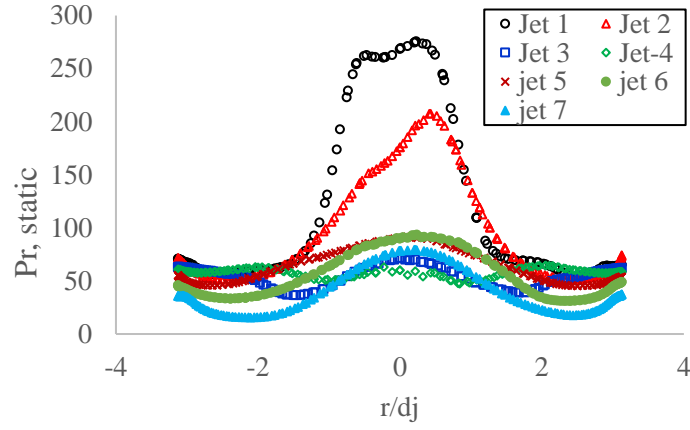


(c)

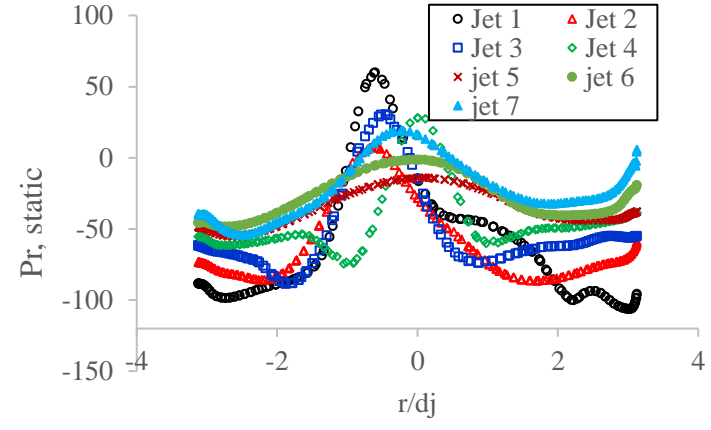


(d)

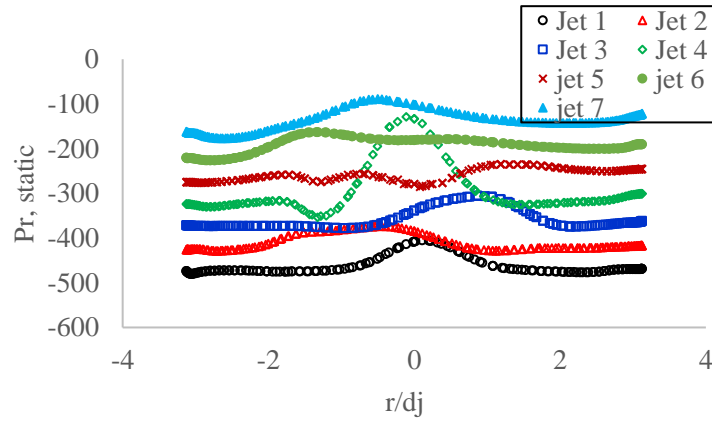
Figure 69: Local static pressure at the curved line facing each jet for jet Reynolds of 7,500, (a) stationary, (b) 250 rpm, (c) 500 rpm, (d) 750 rpm



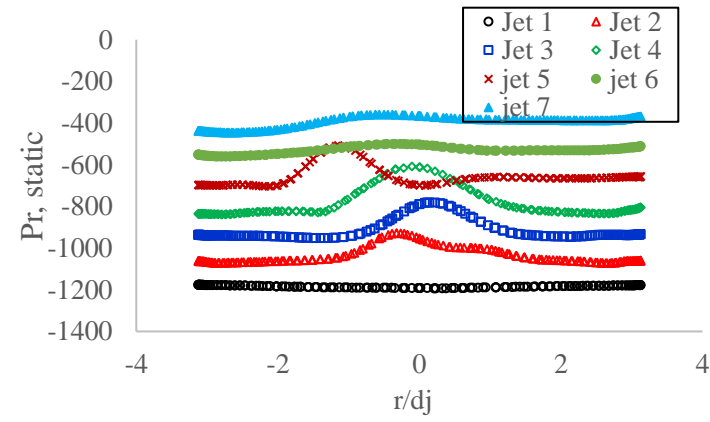
(a)



(b)



(c)



(d)

Figure 70: Local static pressure at the curved line facing each jet for jet Reynolds of 10,000, (a) stationary, (b) 250 rpm, (c) 500 rpm, (d) 750 rpm

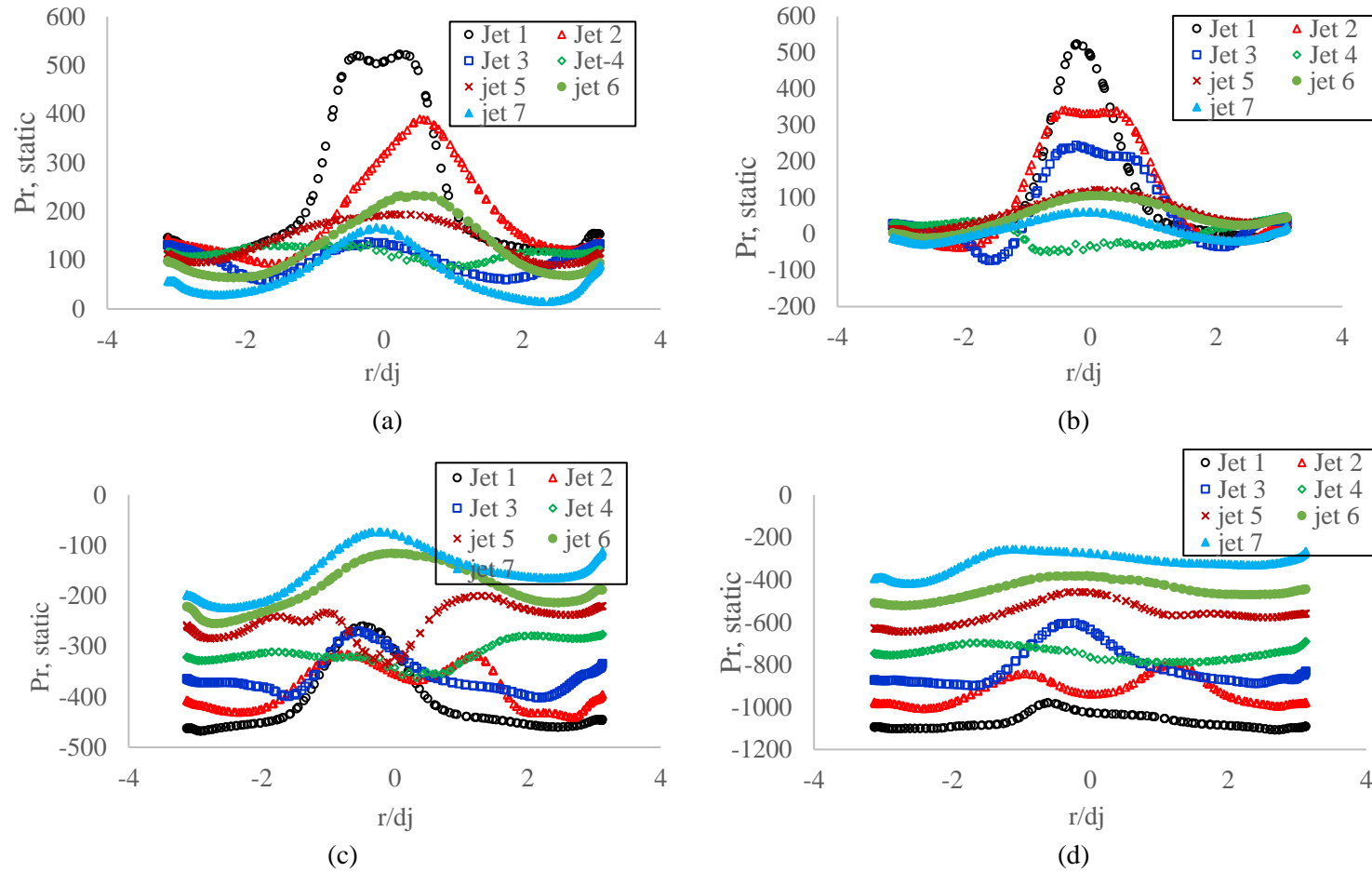


Figure 71: Local static pressure at the curved line facing each jet for jet Reynolds of 15,000, (a) stationary, (b) 250 rpm, (c) 500 rpm, (d) 750 rpm

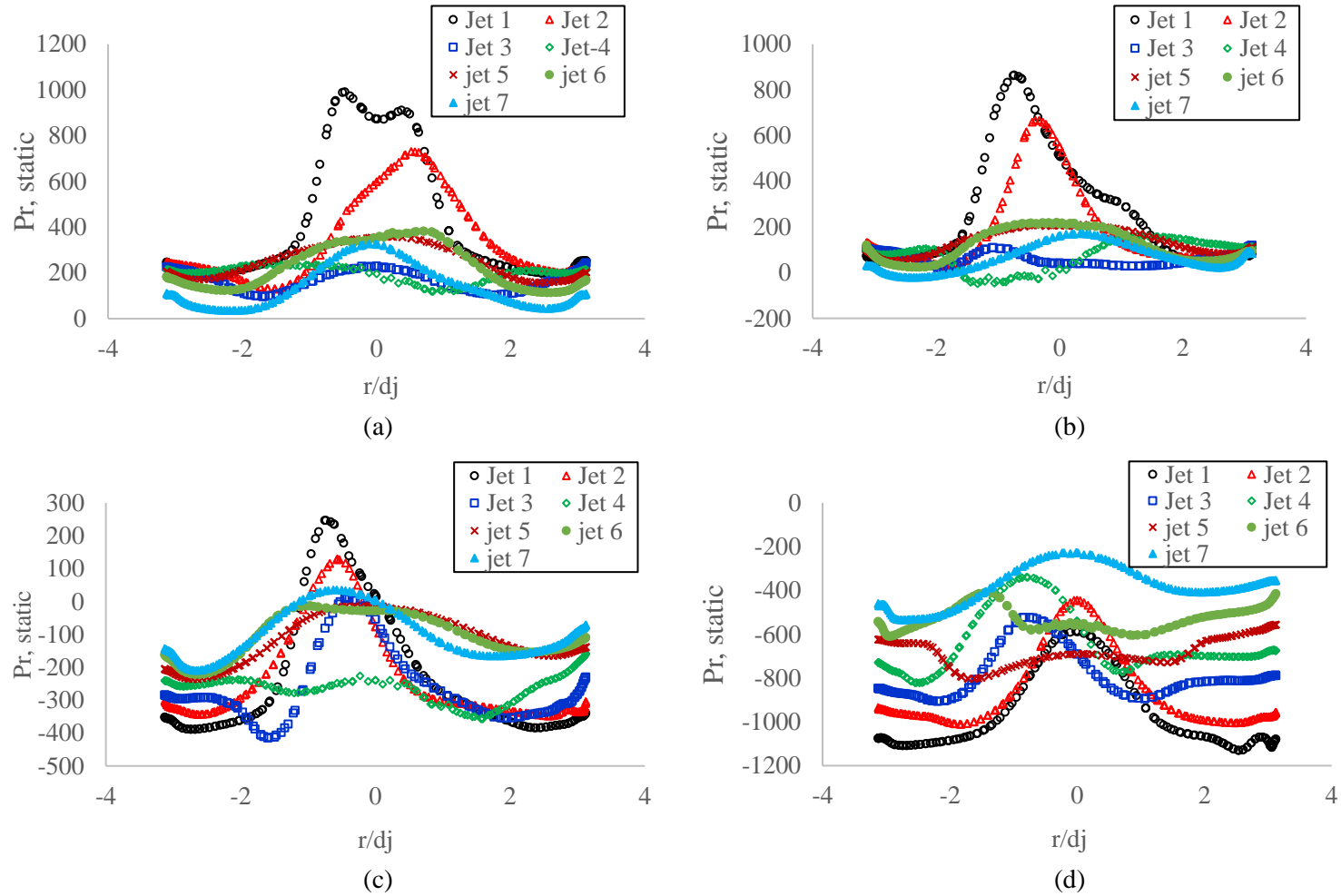
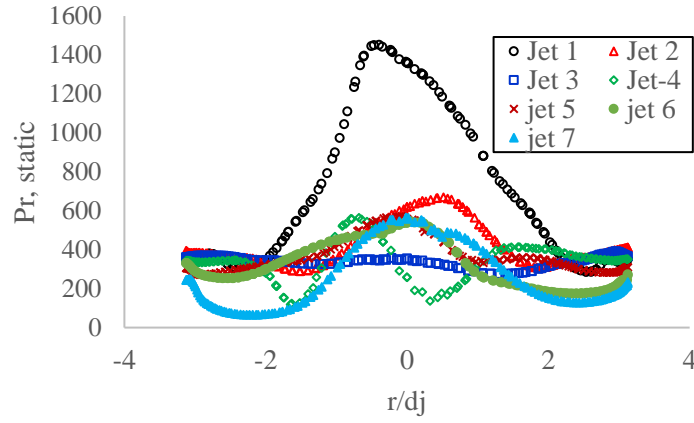
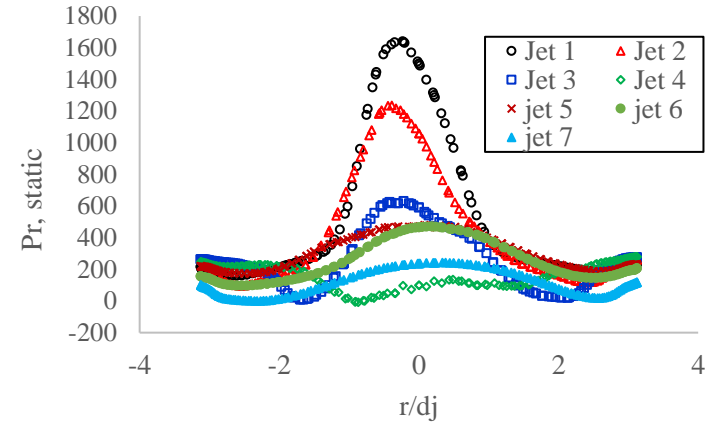


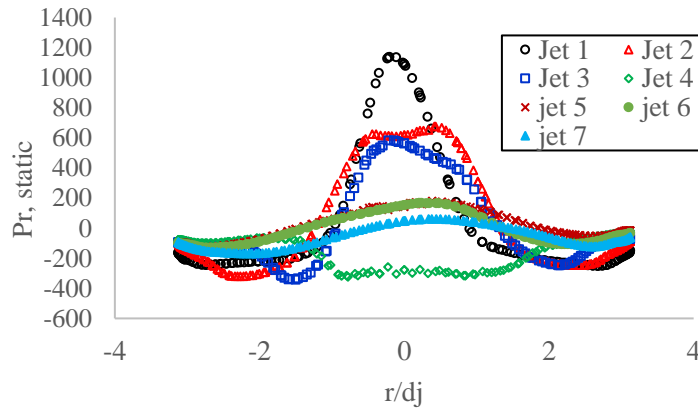
Figure 72: Local static pressure at the curved line facing each jet for jet Reynolds of 20,000, (a) stationary, (b) 250 rpm, (c) 500 rpm, (d) 750 rpm



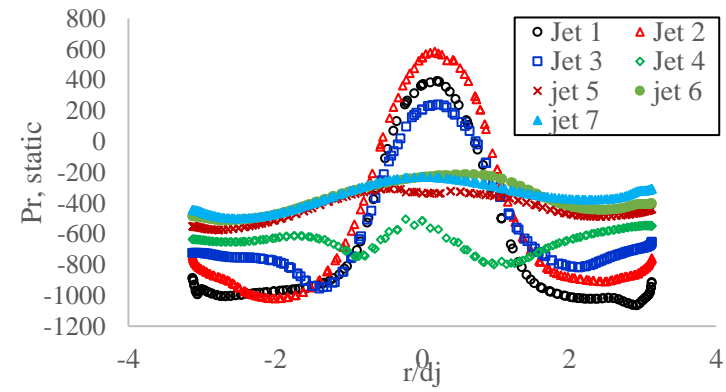
(a)



(b)



(c)



(d)

Figure 73: Local static pressure at the curved line facing each jet for jet Reynolds of 25,000, (a) stationary, (b) 250 rpm, (c) 500 rpm, (d) 750 rpm

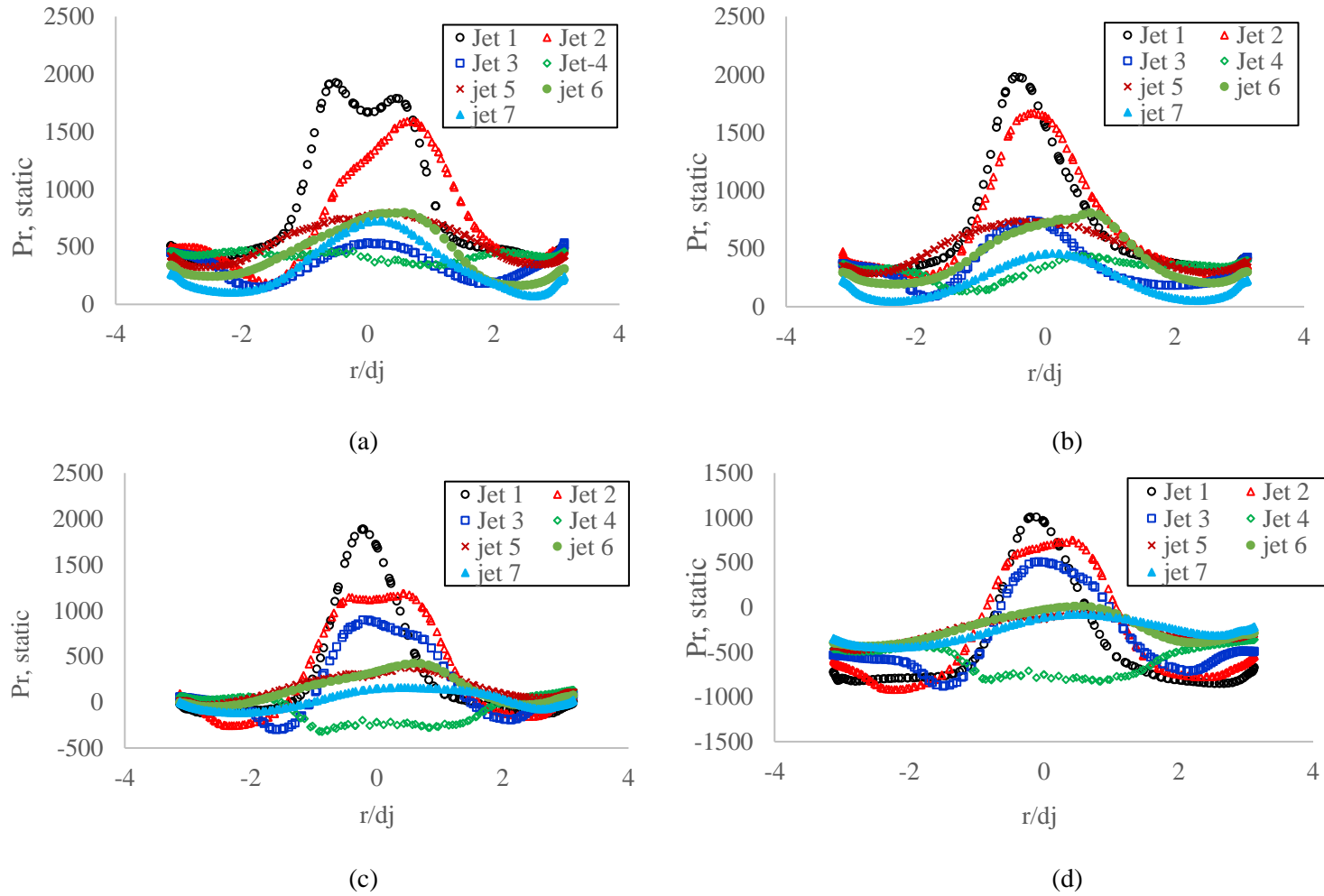


Figure 74: Local static pressure at the curved line facing each jet for jet Reynolds of 30,000, (a) stationary, (b) 250 rpm, (c) 500 rpm, (d) 750 rpm

5.2.6 Static Pressure Variation on the Center Line

Figure 75 plots the static pressure distribution along the curved surface leading edge for Reynolds numbers and rpm. Observing how static pressure changes from Figure 75(a) to Figure 75(f) indicates increasing jet Reynolds number significantly affects the local static pressure. After examining Figure 75, as rotating velocity increases, the static pressure near jets one and two decreases. This static pressure drop is expected because centrifugal force pulls the fluid and forces it toward the upper jets (jets six and seven). Hence, this centrifugal force created a low pressure near jets one and two. At low Reynolds numbers, the impingement remained insignificant, and the pressure distribution along the leading edge remained more uniform than high Reynolds numbers. The local static pressure has its minimum value at the smallest examined Reynolds number and the lowest examined rpm. Figure 75(a) presents at jet Reynolds number of 7,500 and high rotating velocity (500 and 750 rpm), the impact of jets one and two on local static pressure is hardly noticeable due to the low mass fraction passing through these jets compared to other jets. Figure 75(a) and (b) illustrated at jet Reynolds numbers ($Re_j = 7,500$ and 10,000) and high rotating velocity (500 and 750 rpm), show that jets six and seven weakly affected local static pressure due to crossflow created by the centrifugal force. As will be discussed in Figure 78, jets six and seven encountered the highest mass fraction. Nevertheless, they are weakly affected at a low Reynolds number. Crossflow created by jets three, four, and five affected the upper jets (six and seven), and the crossflow significantly decreased static pressure.

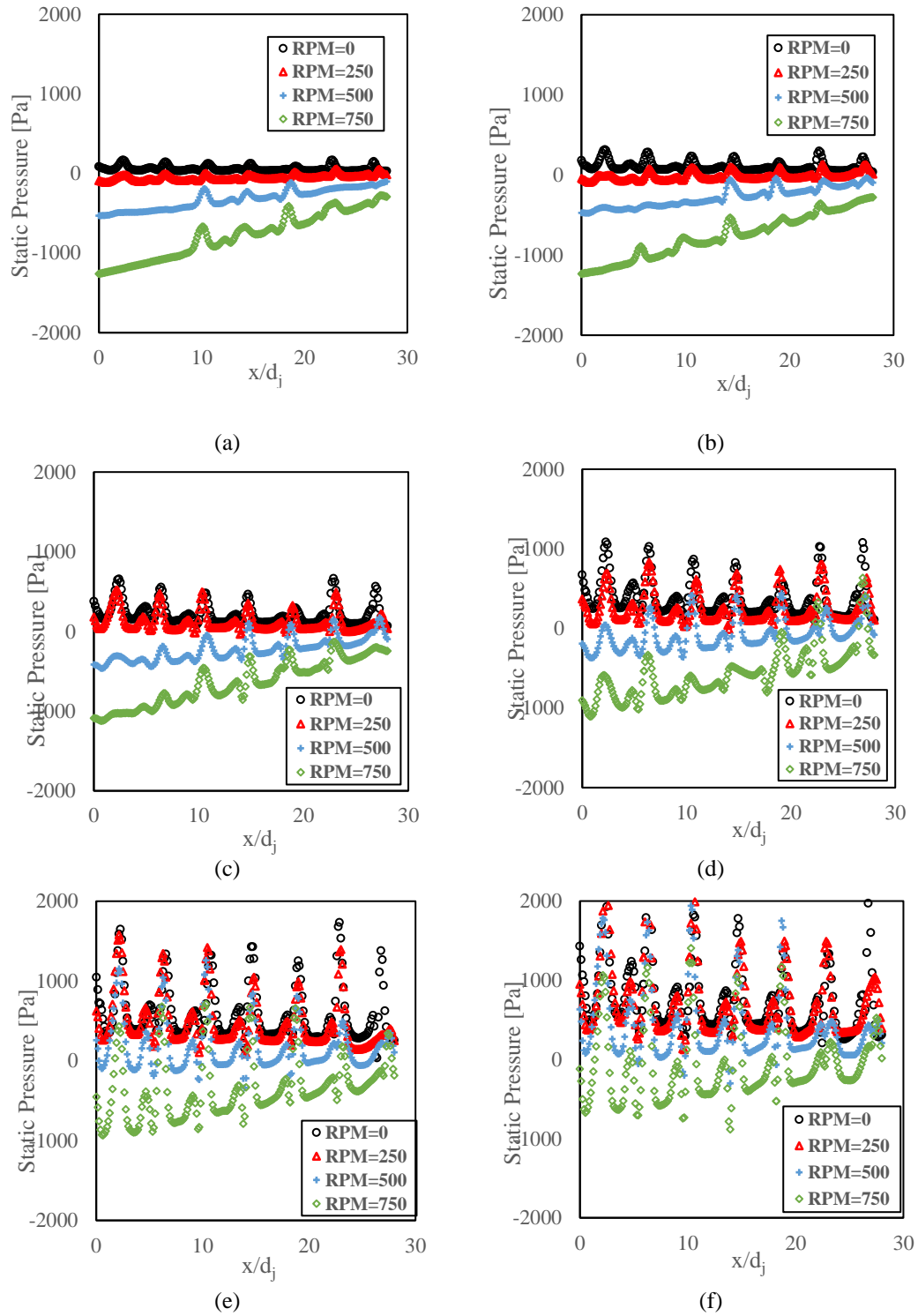


Figure 75: Local static pressure on line A-A (center line) for jet Reynolds number of (a) 7,500, (b) 10,000, (c) 15,000, (d) 20,000, (e) 25,000 and (f) 30,000

5.2.7 Nusselt Number Distribution on the Line

Figure 76 displays the local Nusselt number distribution on the curved surface's centerline for different Reynolds numbers and rpm. For low jet Reynolds numbers, the Nusselt number distribution does not remain uniform, and the local Nusselt number for each jet is much higher than the average Nusselt number compared to higher Reynolds numbers. As the Reynolds number increases, the Nusselt number increases, and the difference between maximum and minimum values of Nusselt number decreases as well as. The minimum local Nusselt number occurred for jets one and two at low Reynolds number and high rpm. Figure 76 depicts rpm does not significantly affect the Nusselt number for high jet Reynolds numbers, as shown in Figure 76 (c), (d), (e), and (f). As shown in Figure 76 (f), the angular velocity impacts the local Nusselt number insignificantly at high Reynolds numbers, indicating jet inertia force is more significant than the centrifugal force.

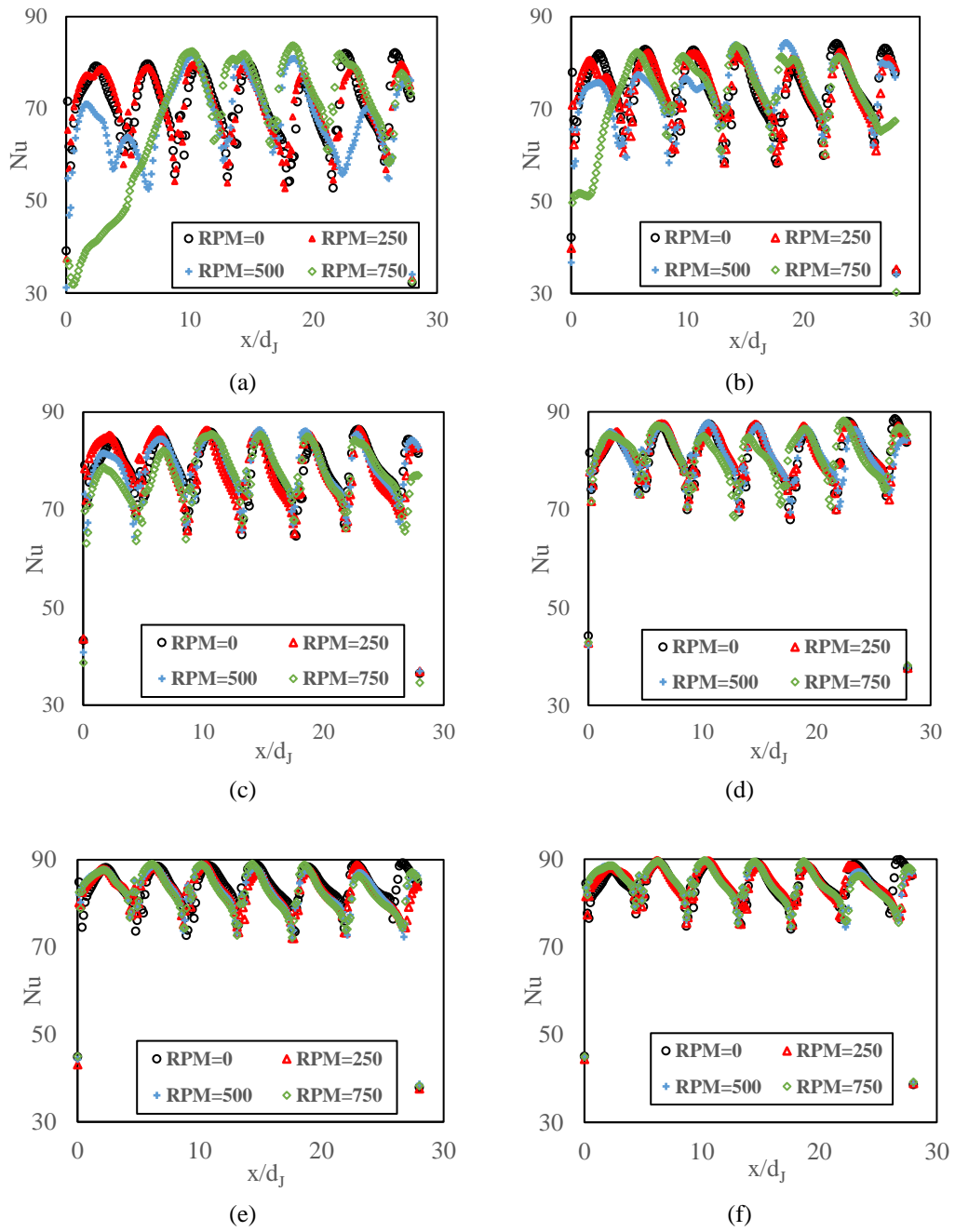


Figure 76: Nusselt number on line A-A (center line) for jet Reynolds number of (a) 7,500, (b) 10,000, (c) 15,000, (d) 20,000, (e) 25,000 and (f) 30,000

5.2.8 Averaged Local Nusselt Number Facing Each Jet

In Figure 77, the average local Nusselt number on the curved surface facing each jet is plotted. Principally at low jet Reynolds numbers, the rotation velocity significantly affects the local Nusselt number. Generally, the local Nusselt number for jets one through four is higher than jets five through seven. At low jet Reynolds numbers, Figure 77(a) and (b), the centrifugal force dominates, pushing the jet flow radially and deteriorating its Nusselt number. The rotation significantly affected the flow field at low Reynolds numbers, pushing the flow radially, reducing the mass flow in jets one and two, and weakening the impingement. Figure 77(f) reveals rotation effect remained negligible at high jet Reynolds number.

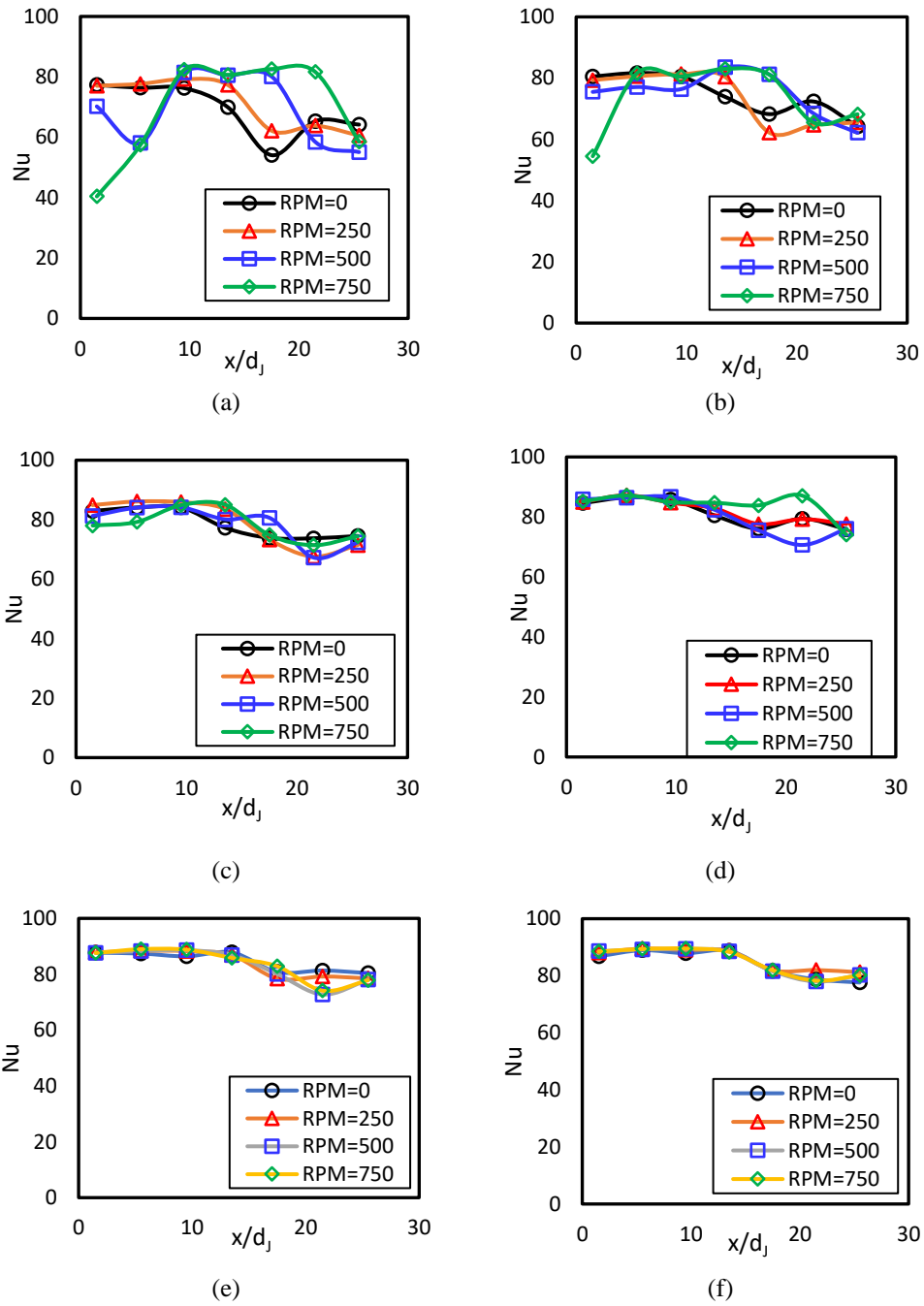


Figure 77: Average Nusselt number on the curved line facing each jet for jet Reynolds number of (a) 7,500, (b) 10,000, (c) 15,000, (d) 20,000, (e) 25,000 and (f) 30,000

5.2.9 Mass Fraction for Each Individual Jet

Figure 78 shows the mass fraction leaving from each jet at various jet Reynolds numbers and rotations. Figure 78 portrays the maximum jet mass fraction (flow rate) in jet seven confronted the least flow resistance. Conversely, the minimum mass fraction in jet one faced the maximum flow resistance. The maximum resistance remained directly proportional to the distance the fluid needed to travel from the jet inlet to the outlet: minimum for jet seven and maximum for jet one. Mass fraction strongly depended on rotation speed, primarily at low jet Reynolds numbers (7,500 and 10,000). However, this dependence faded at high jet Reynolds numbers, signifying for a low jet Reynolds number (less than 10,000), the centrifugal rotational force equated to flow inertia force. As reflected in Figure 78(a) and (b), a high rotation speed reduced mass fraction in first and second jets while compensating for this loss in a mass fraction in jet numbers four through seven. This environment reduced the jet impingement for jets one and two, lowering the local Nusselt number for the first two jets, principally at a high rotation speed.

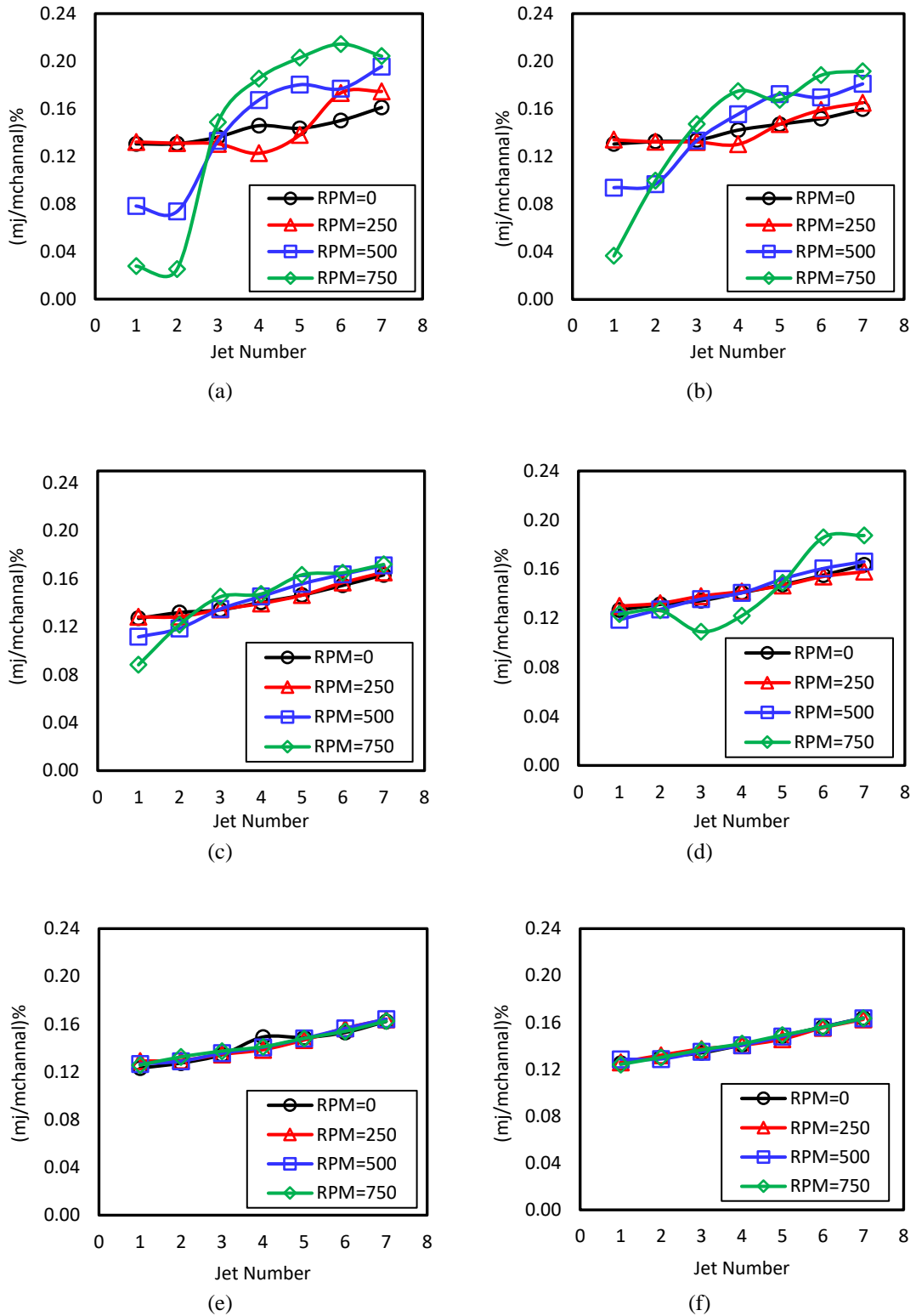


Figure 78: Average mass fraction passing each jet for different jet Reynolds numbers of (a) 7,500, (b) 10,000, (c) 15,000, (d) 20,000, (e) 25,000 and (f) 30,000

5.2.10 Pressure Coefficient for Each Individual Jet

Figure 79 presents jet pressure coefficient (C_p) at various jet Reynolds numbers and rpm. The pressure coefficient represents a dimensionless parameter indicating the pressure change across each jet. The pressure coefficient decreased from jet one to seven at the stationary condition almost in all cases. Having less friction for upper jets (six and seven) resulted from short fluid travel distance leaving the channel with the minimum friction losses. Rotating speed significantly affected the pressure coefficient and, generally, decreased C_p for all jets at Reynolds numbers greater than or equal to 15,000. The pressure coefficient dropped due to rotational speed driven by increased centrifugal force, aiding the flow toward the outlet. For Reynolds numbers 7,500 and 10,000, this effect reversed for jets one and two, where centrifugal force dominated and reduced the mass flow leaving these jets. Hence higher pressure is needed to push the flow through these jets. The pressure coefficient decreased around eight times for low jet Reynolds numbers ($Re_j = 7500$) with the rotation of 750, while at $Re_j = 30,000$ the C_p decreased less than three times at various rotational speeds.

Pressure coefficient is calculated based on the following formula:

$$C_p = \frac{p_j - p_\infty}{\frac{1}{2} \cdot \rho_\infty V_j^2}$$

Where;

p_j – jet inlet pressure

p_∞ – atmospheric pressure

ρ – fluid density

V_j – averaged jet velocity

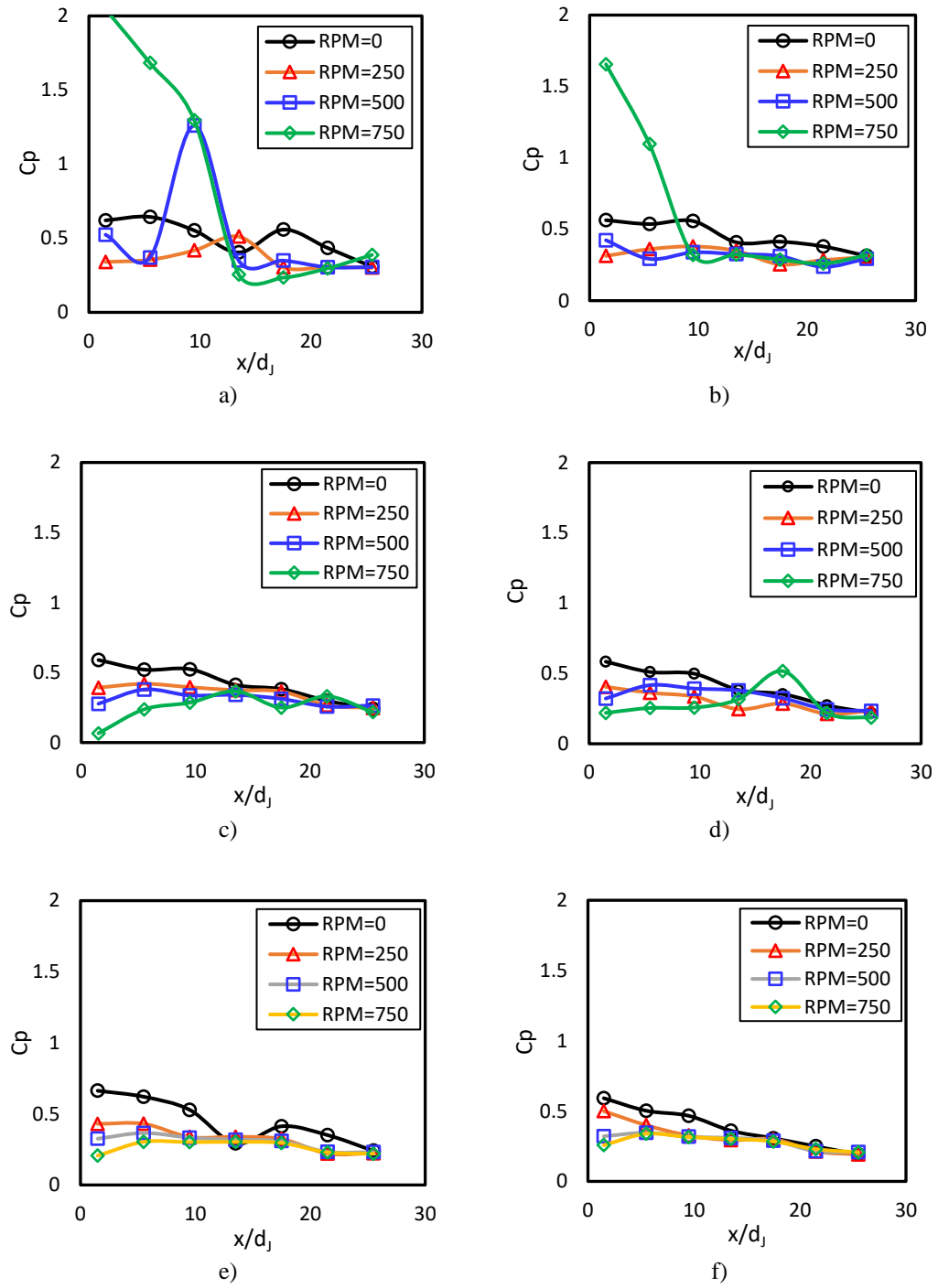


Figure 79: Pressure coefficient facing each jet for different jet Reynolds numbers of (a) 7,500, (b) 10,000, (c) 15,000, (d) 20,000, (e) 25,000 and (f) 30,000

5.2.11 Correlation

The study covers a range of jet Reynolds numbers of 7500 to 30,000 under rotational speeds of 0, 250, 500, and 750 rpm. Figure 80 summarizes the overall study findings:

- Overall Nusselt number increases as the Reynolds numbers increases.
- Rotation affects the heat transfer coefficient at low jet Reynold numbers but this effect is diminished at high jet Reynolds numbers. The observed flow and produced pressure fields support this conclusion.
- Generally, jet impingement embodies an efficient method for cooling the gas turbine blade's leading edge. The cooling performance at low jet Reynolds number is strongly influenced by the individual jet location, crossflow, and rotation speed.
- Leading-edge rotation substantially effects on the flow behavior at low jet Reynolds numbers but minimizes at high Reynolds numbers.
- Finally, Reynolds and rotation numbers impacting the Nusselt number combine into a correlation assessing the rotating leading edge's cooling performance.

$$Nu_{Ro} = 14.54 \cdot Re_j^{0.164} \cdot (1 - Ro_j)^{2.682} \quad (19)$$

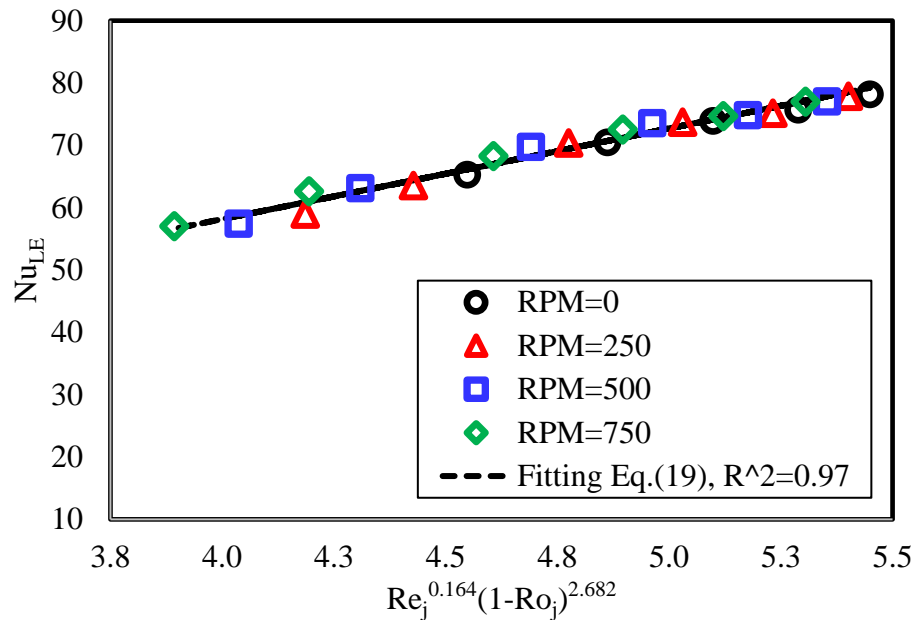


Figure 80: Correlation fit with computation results

Chapter 6 Conclusion and future work

The aim of this work is to study the flow field and the heat transfer performance for the leading edge of a rotating gas turbine blade. An experimental setup has been constructed using advanced measuring instrumentations. The experimental setup is designed and built to operate with jet Reynolds number of 7,500 and maximum rotation speed of 200 rpm. The experimental setup has been used to validate a numerical simulation. Later, the numerical simulation is used to understand the flow field and to diagnose the interaction between jet flow and cross flow. In this analysis, the leading-edge wall is exposed to a constant heat flux, while being cooled via seven impinging jets. Once the numerical study is validated, a series of numerical experimentations have been conducted for a range of jet Reynolds numbers varying from 7,500 to 30,000 under different rotations speed ranging from 0 to 750rpm. The numerical analysis has been used to improve the initial design by improving the system inlet area. These results have been used to establish a mathematical relation between overall Nusselt number, jet rotation number and jet Reynolds number. This mathematical relation is of a great use when design jet impingement thermal system.

6.1 Conclusions

The following points outline the overall validation findings:

- Based on the used instrumentations uncertainties, an adequate agreement between experimental data (calibrated TLC and thermocouples results) and CFD results.

- The SST k- ω turbulence model with y^+ of order one is an appropriate model to simulate internal channel jet impingement under crossflow and rotating system.
- Both experimental measurements and numerical results, namely the temperature distribution along the centerline for the leading-edge target surface, show a very good agreement for jets number 3, 4 and 5.
- The results reveal the importance of the size of the entrance for the cooling air and its impact on the flow, which could eliminate the jet impingements from jets near the entrance premises.
- A CFD analysis may overestimate or underestimate an experimental result especially when the CFD model does not capture minor features of the problem such as wall thickness and outlet inner step lip.

The following points outline the overall parametric model findings:

- Overall Nusselt number increases as the Reynolds number increases ($Nu_{Ro} \propto Re_j^{0.164}$).
- Overall Nusselt number decreases as the rotation number increases ($Nu_{Ro} \propto -Ro_j^{2.682}$).
- Rotation speed causes a drop in the overall heat transfer, mainly at low jet Reynolds number, while it has insignificant effect at high jet Reynolds numbers.
- In general, the jet impingement is an efficient method for cooling the leading edge of gas turbine blade. The cooling performance at low jet Reynolds numbers is strongly influenced by the individual jet location and the rotation speed.

- Leading-edge rotation substantially influences flow at low Reynolds numbers and barely has an effect at high Reynolds numbers.

6.2 Future work

- Improving heat removal using jet impingement has great potential to improve the thermal management in many applications. Hence, more research is needed to improve jet impingement such as impinging on a surface roughness or porous wall, changing jet location to produce vortex flow, impinging vortex jet, testing jet angles and using variable jet angles with different rotation speeds.
- Another extension of the present work is to study the impact of number of jet and jet diameter ratio to channel diameter. Also, possible useful work is developing zero model to predict mass fraction for variable jet diameters.

References

1. Oguma, H., et al., *Development of advanced materials and manufacturing technologies for high-efficiency gas turbines*. Mitsubishi Heavy Ind. Tech. Rev, 2015. 52(4): p. 5-14.
2. Çengel, Y.A. and M.A. Boles, *Thermodynamics : an engineering approach*. Seventh edition. ed. 2011, New York, NY: McGraw-Hill.
3. Sautner, M., S. Clouser, and J.C. Han, *Determination of surface heat transfer and film cooling effectiveness in unsteady wake flow conditions*. 1993, *agard conference proceedings agard cp*.
4. Han, J.C., S. Dutta, and S. Ekkad, *Gas Turbine Heat Transfer and Cooling Technology, Second Edition*. 2012: CRC Press. doi: 10.1201/b13616.
5. Han, J.-C. and M. Huh. *Recent studies in turbine blade internal cooling*. Begel House Inc. <https://doi.org/10.1155/S1023621X04000442>.
6. Lakshminarayana, B. and S. Yavuzkurt, *Fluid Dynamics and Heat Transfer of Turbomachinery*. Applied mechanics reviews., 1996. 49(12 1). doi:10.1002/9780470172629.
7. Lakshminarayana, B., *Fluid dynamics and heat transfer of turbomachinery*. 1995: John Wiley & Sons. doi:10.1002/9780470172629.
8. Taylor, J.R., *Heat Transfer Phenomena in Gas Turbines*. 1980(79665). <https://doi.org/10.1115/80-GT-172>.
9. Viskanta, R., *Heat transfer to impinging isothermal gas and flame jets*. Experimental Thermal and Fluid Science, 1993. 6(2): p. 111-134.
10. Liu, Z., Z. Feng, and L. Song, *Numerical Study on Flow and Heat Transfer Characteristics of Swirl Cooling on Leading Edge Model of Gas Turbine Blade*. 2011(54655): p. 1495-1504.
11. Bunker, R.S. and D.E. Metzger, *Local Heat Transfer in Internally Cooled Turbine Airfoil Leading Edge Regions: Part I—Impingement Cooling Without Film Coolant Extraction*. Journal of Turbomachinery, 1990. 112(3): p. 451-458.
12. Liu, Z. and Z. Feng, *Numerical simulation on the effect of jet nozzle position on impingement cooling of gas turbine blade leading edge*. International Journal of Heat and Mass Transfer, 2011. 54(23): p. 4949-4959.

13. Lin, G., et al., *Numerical investigation on heat transfer in an advanced new leading edge impingement cooling configuration*. Propulsion and Power Research, 2015. 4(4): p. 179-189.
14. Yang, L., et al., *Experimental and numerical investigation of unsteady impingement cooling within a blade leading edge passage*. International Journal of Heat and Mass Transfer, 2014. 71: p. 57-68.
15. Liu, L., et al., *Effect of tangential jet impingement on blade leading edge impingement heat transfer*. Applied Thermal Engineering, 2018. 130: p. 1380-1390.
16. Hamdan, M.O., E. Elnajjar, and Y. Haik, *Measurement and Modeling of Confined Jet Discharged Tangentially on a Concave Semicylindrical Hot Surface*. Journal of Heat Transfer, 2011. 133(12). <https://doi.org/10.1115/1.4004529>
17. Emad, E., H.M. Omar, and H. Yousef, *Experimental investigation of impinging jet flow on a heated curved surface*. 2012: 6th International Conference on Thermal Engineering.
18. Elnajjar, E., M.O. Hamdan, and Y. Haik, *Experimental investigation of internal channel cooling via jet impingement*. Fluid Dynamics and Materials Processing, 2013. 9(1): p. 77-89.
19. Al-Hemyari, M., M. Hamdan, and F. Orhan, *Numerical Analysis of Film Cooling Shield Formed by Confined Jet Discharging on a Flat Plate*. International Journal of Heat and Technology, 2019. 37: p. 327-333.
20. Al-Hemyari, M., M. Hamdan, and M. Orhan, *Optimization of a Confined Jet Geometry to Improve Film Cooling Performance Using Response Surface Methodology (RSM)*. Processes, 2020. <https://doi.org/10.3390/pr8020232>.
21. Elebiary, K. and M.E. Taslim, *Experimental/Numerical Crossover Jet Impingement in an Airfoil Leading-Edge Cooling Channel*. Journal of Turbomachinery, 2012. <https://doi.org/10.1115/1.4006420>.
22. Taslim, M.E., K. Bakhtari, and H. Liu, *Experimental and Numerical Investigation of Impingement on a Rib-Roughened Leading-Edge Wall*. Journal of Turbomachinery, 2003. 125(4): p. 31-41.
23. Taslim, M.E. and A. Khanicheh, *Experimental and Numerical Study of Impingement on an Airfoil Leading Edge With and Without Showerhead and Gill Film Holes*. Journal of Turbomachinery, 2006. 128(2): p. 310-320.
24. Rao, Y., *Jet Impingement Heat Transfer in Narrow Channels With Different Pin Fin Configurations on Target Surfaces*. Journal of Heat Transfer, 2018. 140(7): p. 72201. <https://doi.org/10.1115/1.4039015>

25. Wang, N., et al., *Turbine Blade Leading Edge Cooling With One Row of Normal or Tangential Impinging Jets*. Journal of Heat Transfer, 2018. 140(6): p. 62201. <https://doi.org/10.1115/1.4038691>.
26. Fechter, S., et al., *Experimental and numerical investigation of narrow impingement cooling channels*. International Journal of Heat and Mass Transfer, 2013. 67: p. 1208-1219.
27. Chi, Z., et al., *Experimental and numerical study of the anti-crossflows impingement cooling structure*. International Journal of Heat and Mass Transfer, 2013. 64: p. 567-580.
28. Zhou, T., et al., *Numerical analysis of turbulent round jet impingement heat transfer at high temperature difference*. Applied Thermal Engineering, 2016. 100: p. 55-61.
29. Baughn, J.W. and S. Shimizu, *Heat Transfer Measurements From a Surface With Uniform Heat Flux and an Impinging Jet*. Journal of Heat Transfer, 1989. 111(4): p. 1096-1098.
30. Penumadu, P.S. and A.G. Rao, *Numerical investigations of heat transfer and pressure drop characteristics in multiple jet impingement system*. Applied Thermal Engineering, 2017. 110: p. 1511-1524.
31. Wan, C., Y. Rao, and P. Chen, *Numerical predictions of jet impingement heat transfer on square pin-fin roughened plates*. Applied Thermal Engineering, 2015. 80: p. 301-309.
32. Liu, Z., et al., *Numerical simulation on impingement and film composite cooling of blade leading edge model for gas turbine*. Applied Thermal Engineering, 2014. 73(2): p. 1432-1443.
33. Maikell, J., et al., *Experimental Simulation of a Film Cooled Turbine Blade Leading Edge Including Thermal Barrier Coating Effects*. Journal of Turbomachinery, 2010. <https://doi.org/10.1115/1.4000537>.
34. Burberi, E., et al., *Effect of Rotation on a Gas Turbine Blade Internal Cooling System: Numerical Investigation*. Journal of Turbomachinery, 2017. <https://doi.org/10.1115/1.4034799>.
35. Paccati, S., et al., *Numerical Investigation on the Effect of Rotation and Holes Arrangement in Cold Bridge-Type Impingement Cooling Systems*. J. Turbomach, 2020. 142(4). <https://doi.org/10.1115/1.4046454>.
36. Safi, A., M.O. Hamdan, and E. Elnajjar, *Numerical investigation on the effect of rotation on impingement cooling of the gas turbine leading edge*. Alexandria Engineering Journal, 2020. 59(5): p. 3781-3797.

37. Safi Amin, H.M. Omar, and E. Emad, *Effect of Angular Velocity on Mass Fraction Distribution for Jets Impinging on Airfoil Leading-Edge Cavity*. 2020: 5th World Congress on Momentum, Heat and Mass Transfer (MHMT'20). doi: 10.11159/enfht20.147.
38. Chupp, R.E., H.E. Helms, and P.W. McFadden, *Evaluation of internal heat-transfer coefficients for impingement-cooled turbine airfoils*. Journal of Aircraft, 1969. 6(3): p. 203-208.
39. Goldstein, R.J. and A.I. Behbahani, *Impingement of a circular jet with and without cross flow*. International Journal of Heat and Mass Transfer, 1982. 25(9): p. 1377-1382.
40. Kercher, D.M. and W. Tabakoff, *Heat Transfer by a Square Array of Round Air Jets Impinging Perpendicular to a Flat Surface Including the Effect of Spent Air*. Journal of Engineering for Power, 1970. 92(1): p. 73-82.
41. Florschuetz, L.W., C.R. Truman, and D.E. Metzger, *Streamwise Flow and Heat Transfer Distributions for Jet Array Impingement with Crossflow*. Journal of Heat Transfer, 1981. 103(2): p. 337-342.
42. Fenot, M., E. Dorignac, and J.J. Vullierme, *An experimental study on hot round jets impinging a concave surface*. International Journal of Heat and Fluid Flow, 2008. 29(4): p. 945-956.
43. Lee, D.H., Y.S. Chung, and S.Y. Won, *Technical Note The effect of concave surface curvature on heat transfer from a fully developed round impinging jet*. International Journal of Heat and Mass Transfer, 1999. 42(13): p. 2489-2497.
44. Taslim, M.E., L. Setayeshgar, and S.D. Spring, *An Experimental Evaluation of Advanced Leading Edge Impingement Cooling Concepts*. Journal of Turbomachinery, 2001. <https://doi.org/10.1115/1.1331537>.
45. Martin, E.L., L.M. Wright, and D.C. Crites, *Impingement Heat Transfer Enhancement on a Cylindrical, Leading Edge Model With Varying Jet Temperatures*. Journal of Turbomachinery, 2013. <https://doi.org/10.1115/1.4007529>.
46. Metzger, D.E., et al., *Heat Transfer Characteristics for Inline and Staggered Arrays of Circular Jets with Crossflow of Spent Air*. Journal of Heat Transfer, 1979. 101(3): p. 526-531.
47. Florschuetz, L.W., R.A. Berry, and D.E. Metzger, *Periodic Streamwise Variations of Heat Transfer Coefficients for Inline and Staggered Arrays of Circular Jets with Crossflow of Spent Air*. Journal of Heat Transfer, 1980. 102(1): p. 132-137.

48. Akella, K.V. and J.-C. Han, *Impingement Cooling in Rotating Two-Pass Rectangular Channels with Ribbed Walls*. Journal of Thermophysics and Heat Transfer, 1999. 13(3): p. 364-371.
49. Hong, S.K., D.H. Lee, and H.H. Cho, *Effect of jet direction on heat/mass transfer of rotating impingement jet*. Applied Thermal Engineering, 2009. 29(14): p. 2914-2920.
50. Deng, H., et al., *Experiments on impingement heat transfer with film extraction flow on the leading edge of rotating blades*. International Journal of Heat and Mass Transfer, 2012. 55(21-22): p. 5425-5435.
51. Elston, C.A. and L.M. Wright, *Leading Edge Jet Impingement Under High Rotation Numbers*. Journal of Thermal Science and Engineering Applications, 2017. <https://doi.org/10.1115/1.4035892>.
52. Wright, L.M. and C.A. Elston, *Experimental Investigation of Heat Transfer in a Leading Edge, Two-Pass Serpentine Passage at High Rotation Numbers*. 2012(44779): p. 827-839.
53. Massini, D., et al., *Effect of Rotation on a Gas Turbine Blade Internal Cooling System: Experimental Investigation*. Journal of Engineering for Gas Turbines and Power, 2017. <https://doi.org/10.1115/GT2016-57594>.
54. Wilcox, D.C., *Formulation of the k-omega Turbulence Model Revisited*. AIAA Journal, 2008. 46(11): p. 2823-2847.
55. Menter, F.R., *Review of the shear-stress transport turbulence model experience from an industrial perspective*. International Journal of Computational Fluid Dynamics, 2009. 23(4): p. 305-316.
56. Safi, A., E. Elnajjar, and M. Hamdan. *Isothermal compressed air system for internal channel cooling*. in *2019 Advances in Science and Engineering Technology International Conferences (ASET)*. 2019. doi: 10.1109/ICASET.2019.8714523.
57. Singh, P. and S.V. Ekkad, *Detailed Heat Transfer Measurements of Jet Impingement on Dimpled Target Surface Under Rotation*. Journal of Thermal Science and Engineering Applications, 2018. <https://doi.org/10.1115/1.4039054>.
58. Lamont, J.A., S.V. Ekkad, and M.A. Alvin, *Effects of Rotation on Heat Transfer for a Single Row Jet Impingement Array With Crossflow*. Journal of Heat Transfer, 2012. <https://doi.org/10.1115/1.4006167>.

List of Publications

1. Safi, A., M.O. Hamdan, and E. Elnajjar, Numerical investigation on the effect of rotation on impingement cooling of the gas turbine leading edge. Alexandria Engineering Journal, 2020. 59(5): p. 3781-3797.
2. Safi Amin, H.M. Omar, and E. Emad, Effect of Angular Velocity on Mass Fraction Distribution for Jets Impinging on Airfoil Leading-Edge Cavity. 2020: 5th World Congress on Momentum, Heat, and Mass Transfer (MHMT'20). doi: 10.11159/enfht20.147.
3. Safi, A., E. Elnajjar, and M. Hamdan, Isothermal compressed air system for internal channel cooling. Advances in Science and Engineering Technology International Conferences (ASET), 2019. doi: 10.1109/ICASET.2019.8714523.